Monte Carlo simulations of phonon transport in nanostructures based on ab-initio methods

Junbum Park

THESE DE DOCTORAT

NNT : 2024UPAST068

université PARIS-SACLAY

Monte Carlo simulations of phonon transport in nanostructures based on ab-initio methods

Simulation Monte Carlo du transport des phonons dans les nanostructures au moyen des méthodes ab-initio

Thèse de doctorat de l'université Paris-Saclay

École doctorale n°575 : Electrical, Optical, Bio-physics and Engineering (EOBE)
Spécialité de doctorat : Electronique, Photonique et Micro-Nanotechnologies
Graduate School : Sciences de l'ingénierie et des systèmes
Référent : Faculté des sciences d'Orsay

Thèse préparée dans l'unité de recherche **Centre de Nanosciences et de Nanotechnologies** (Université Paris-Saclay, CNRS), sous la direction de **Jérôme SAINT-MARTIN**, Professeur à l'ENS Paris-Saclay, et le co-encadrement de **Marco PALA**, Professeur à l'Université d'Udine

Thèse soutenue à Paris-Saclay, le 31 mai 2024, par

Junbum PARK

Composition du Jury

Membres du jury avec voix délibérative

Damien QUERLIOZ Directeur de recherche, CNRS, Université Paris-Saclay	Président
Marc BESCOND Directeur de recherche, CNRS, Aix-Marseille Université	Rapporteur & Examinateur
Konstantinos TERMENTZIDIS Directeur de recherche, CNRS, INSA Lyon	Rapporteur & Examinateur
Jelena SJAKSTE Chargée de recherche, CNRS, Institut Polytechnique de Paris	Examinatrice

Titre : Simulation Monte Carlo du transport des phonons dans les nanostructures au moyen des méthodes ab-initio

Mots clés : Transport des phonons, Théorie de la fonctionnelle de la densité, Méthode de Monte Carlo, Nanostructures, Conductivité thermique, Conductance thermique d'interface

Résumé : Alors que la tendance à la miniaturisation des appareils électroniques se poursuit, la compréhension du transport de chaleur à l'échelle nanométrique devient de plus en plus cruciale pour développer des systèmes fiables et économes en énergie. La loi de Fourier conventionnelle ne parvient pas à capturer la dynamique complexe du transport de chaleur basé sur les phonons dans de tels dispositifs miniaturisés. Avec la recherche de dispositifs plus compacts et plus performants, l'exploration de matériaux alternatifs au-delà du silicium est tout aussi essentielle, en se concentrant sur leurs propriétés thermiques. Dans cette thèse, nous étudions le transport des phonons au sein de nanostructures en utilisant des méthodes stochastiques de Monte Carlo (MC). La précision des simulations est améliorée grâce à l'utilisation d'une description complète des matériaux de bande dérivée de calculs ab-initio basés sur la théorie fonctionnelle de la densité (DFT) sans recourir à des paramètres empiriques. Cette approche méthodologique permet des calculs précis de diffusion de phonons sur une large plage de températures de 0,1 à 1 000 K, intégrant des mécanismes de diffusion normale, Umklapp et isotopique pour tenir compte des interactions anharmoniques. Nous nous concentrons sur l'examen de matériaux alternatifs, tels que l'arséniure de gallium (GaAs) et de matériaux bidimensionnels (2D) comme le graphène, le nitrure de bore hexagonal (h-BN) et les dichalcogénures de métaux de transition (TMDC), chacun sélectionné pour ses propriétés thermiques uniques.

Cette thèse présente un contexte théorique complet sur la DFT, soulignant l'importance des effets anharmoniques dans le transport des phonons, et discute des algorithmes de Monte Carlo pour résoudre l'équation de transport de Boltzmann. Les résultats présentés dans cette thèse incluent une analyse approfondie des propriétés thermiques des nanostructures de GaAs et de leur réponse à différentes conditions aux limites, dimensions du dispositif et températures. De plus, nous explorons les propriétés thermiques des matériaux 2D et de leurs hétérostructures latérales, en évaluant leur conductance thermique d'interface (ITC) et la variation des contributions modales des phonons à proximité de l'interface. Utilisant le concept de température directionnelle, l'étude fournit des calculs ITC précis, élucidant ainsi la dynamique thermique complexe au sein de ces hétérostructures. Enfin, nous étudions la réponse thermique transitoire dans des hétérostructures latérales 2D h-BN/graphène de 100 nm de long. Grâce à la cartographie positionnelle et à la caractérisation de la réponse temporelle, nous fournissons une compréhension détaillée du comportement thermique transitoire au sein de ces nanostructures. Ces travaux offrent non seulement des contributions substantielles au domaine du transport thermique dans les nanostructures, mais ouvrent également de nouvelles voies pour la conception et l'application de matériaux avancés en électronique.

université PARIS-SACLAY | DOCTORAL SCHOOL Electrical, Optical, Bio: Physics and Engineering (EOBE)

Title : Monte Carlo simulations of phonon transport in nanostructures based on ab-initio methods

Keywords : Phonon transport, Density functional theory, Monte Carlo method, Nanostructures, Thermal conductivity, Interface thermal conductance

Abstract : As the trend towards miniaturization of electronic devices continues, understanding heat transport at the nanoscale becomes increasingly crucial for developing energy-efficient and reliable systems. Conventional Fourier's law fails to capture the complex dynamics of phonon-based heat transport in such miniaturized devices. With the drive for more compact and high-performance devices, exploring alternative materials beyond silicon is equally essential, focusing on their thermal properties. In this thesis, we study the phonon transport within nanostructures employing stochastic Monte Carlo (MC) methods. The accuracy of the simulations is enhanced by utilizing full-band material description derived from ab-initio calculations based on density functional theory (DFT) without reliance on empirical parameters. This methodological approach allows for precise phonon scattering calculations across a broad temperature range of 0.1 to 1000 K, incorporating normal, Umklapp, and isotope scattering mechanisms to account for anharmonic interactions. We focus on examining alternative materials, such as gallium arsenide (GaAs) and two-dimensional (2D) materials like graphene, hexagonal boron nitride (h-BN), and transition metal dichalcogenides (TMDCs), each selected for their unique thermal properties.

This thesis presents a comprehensive theoretical background on DFT, emphasizing the importance of anharmonic effects in phonon transport, and discusses the Monte Carlo algorithms for solving the Boltzmann transport equation. The results presented in this thesis include a thorough analysis of the thermal properties of GaAs nanostructures and their response to varying boundary conditions, device dimensions, and temperatures. Furthermore, we explore the thermal properties of 2D materials and their lateral heterostructures, assessing their interface thermal conductance (ITC) and the variation of phonon modal contributions near the interface. Employing the concept of directional temperature, the study provides precise ITC calculations, thereby elucidating the intricate thermal dynamics within these heterostructures. Finally, we investigate the transient thermal response in 100 nm long 2D h-BN/graphene lateral heterostructures. Through positional mapping and temporal response characterization, we provide a detailed understanding of the transient thermal behavior within these nanostructures. This work not only offers substantial contributions to the field of thermal transport in nanostructures but also opens new pathways for the design and application of advanced materials in electronics.

ACKNOWLEDGMENTS

First and foremost, I extend my deepest gratitude to my supervisors, Jérôme Saint-Martin and Marco Pala, for their invaluable guidance and dedicated support throughout my Ph.D. Their efforts greatly facilitated my research progress and personal growth as a scientist. I am deeply grateful for their patience, understanding, and insightful leadership that steered me toward becoming a researcher.

I would also like to express my appreciation to all members of the COMICS team at C2N, including Philippe Dollfus, Davide Romanin, Anish Joseph, Rémi Helleboid, Owen Loison, Mohammad Ghanem, Alessandro Pilotto, and Adel M'Foukh. Working and discussing with them was not only a pleasure but also an integral part of my professional development. Thank you for the memorable moments shared during our daily interactions in the office.

Thanks go to Damien Querlioz, Jelena Sjakste, and Jean-Paul Adam for their support in administrative, technical, and personal matters. Their invaluable advice each year ensured a smooth doctoral journey.

I am also thankful to Lorenzo Paulatto and Raja Sen for enriching discussions on ab-initio calculations, which broadened my knowledge significantly. These discussions were both enjoyable and immensely beneficial.

My gratitude extends to Jungho Kim and Yvan Bonnassieux, my former supervisors for the KHU-X dual master's program. Their support allowed me to complete my master's program in both South Korea and France. A special thanks to Sungyeop Jung and Yongjeong Lee, who mentored me during my master's course. Their guidance and exemplary conduct in research have been deeply inspiring.

I would also like to acknowledge my Korean colleagues, Jiho Yoon, Heeryung Lee, Minjin Kim, Junha Park, Hyeonseok Sim, Haeyeon Jun, Seonggil Kang, Seongbin Lim, Youngro Lee, Gwanju Eun, Jisoo Oh, and Myeongseop Kim for their camaraderie and support. Special thanks to Yeonsoo Cho, Jihye Baik, Jinhyeok Im, and Yunho Ahn, who were pillars of strength during my challenging times abroad, providing both support and encouragement.

Lastly, my deepest love and appreciation go to my family: my father, Kyoungkug Park; my mother, Younghee Jung; and my brother, Juntae Park. Their unwavering belief in me and constant encouragement have been a source of tremendous energy throughout my journey.

All glory to God, who watched over and guided me throughout my studies abroad.

CONTENTS

LIST OF FIGURES

List of Tables

List of Acronyms and Abbreviations

DFT	Density functional theory
DFPT	Density functional perturbation theory
MC	Monte Carlo
BTE	Boltzmann transport equation
MD	Molecular dynamics
NEGF	Non-equilibrium Green's function
MFP	Mean free path
RTA	Relaxation time approximation
DMM	Diffuse mismatch model
AMM	Acoustic mismatch model
ITC	Interface thermal conductance
CPNF	Cross-plane nanofilm
IPNF	In-plane nanofilm
NW	Nanowire

1 Introduction

1.1 Heat Management

1.1.1 Challenges in miniaturized devices

The trend of miniaturization in electronics is one of the most significant movements within the technology sector over the past several decades [1,2]. This trend is rooted in the semiconductor industry, producing increasingly smaller transistors, which are the fundamental building blocks of electronic devices. Moore's Law, proposed by Gordon Moore in 1965, has been a guiding principle for this trend by predicting the doubling of transistors in integrated circuits approximately every two years [3]. With advancements in materials science and manufacturing techniques, Samsung Electronics and TSMC are currently producing electronic devices with billions of transistors using the 3 nm process technology as of 2024 [4,5]. Despite reaching the limits of Moore's Law, progress is continuing, promising increased integration density.

As these devices shrink to the nanoscale, the importance of efficient heat management becomes critical. The primary challenge in these miniaturized devices is the significantly increased power density, which arises from packing more transistors into a smaller area, as illustrated in Figure 1.1 [6]. This escalation in power density leads to elevated temperatures that can adversely affect device integrity and performance, necessitating solutions to guarantee device longevity and prevent overheating [7].

In a crystalline solid, heat conduction is attributed mainly to two carriers: electrons and quantized modes of lattice, referred to as phonons [8]. Especially in semiconductor materials, heat is primarily conducted through the lattice by the propagation of these phonons [9]. Since phonons influence the properties of semiconductor devices, it becomes essential to understand thermal transport mediated by phonons for the development of optimized electronic devices.

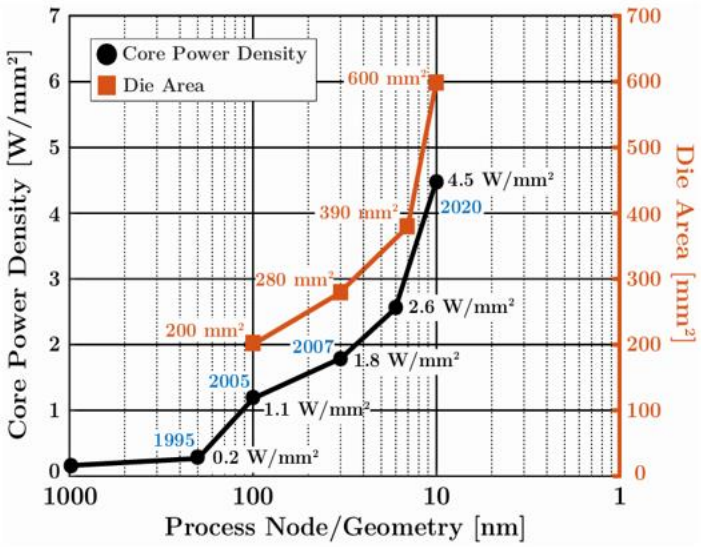

Figure 1.1 The trend of increasing power density in miniaturized processors, underscoring the need for effective thermal management solutions to address the elevated temperatures resulting from higher power densities [6].

Therefore, rigorous and quantitative evaluation of the thermal properties is required to understand how phonons behave within materials or devices. These properties include thermal conductivity, heat capacity, and thermal boundary resistance at interfaces, which are crucial for precisely analyzing the thermal properties in miniaturized electronic devices. For instance, materials with high thermal conductivity serve as efficient heat channels to dissipate heat from hot spots as passive heat spreading [10]. Conversely, materials with low thermal conductivity can be promising candidates as thermoelectric (TE) materials to harvest waste heat by converting it directly into electricity [11].

To design thermal properties for specific applications across various fields, the implementation of diverse technologies is underway through the utilization of point defects, nanostructures, and lattice anharmonicity [12,13]. In alignment with these trends, new theoretical models are indispensable, and numerical simulations can provide valuable insights for nanoscale heat transport [14].

1.2 BEYOND SILICON-BASED TECHNOLOGY

At the core of the electronics industry, silicon has stood as the predominant material due to its semiconducting properties combined with its abundance and compatibility with a wide array of fabrication processes [15]. This prominence is further reinforced by silicon's capacity to form high-quality insulating oxide layers and its versatility in being doped with impurities to fabricate both n-type and p-type materials [16,17]. Consequently, silicon-based technology has enabled the development of a wide range of electronic devices, such as transistors, integrated circuits, solar cells, and even the realm of quantum computing [18–21].

However, as the industry moves towards more compact and high-performance devices, the limitations of silicon become increasingly pronounced [22,23]. These challenges are multifaceted, encompassing issues of speed, packaging complexities, and heat dissipation. The quest for further miniaturization hits physical constraints with unwanted quantum effects, leading to increased power consumption and thermal inefficiencies. In response to these challenges, the semiconductor industry has been compelled beyond traditional scaling paradigms with innovations like FinFET (Fin Field-Effect Transistor) and the GAA (Gate-All-Around) transistor [24,25].

While the new architectures provide improvements in performance and energy efficiency, they fall short of addressing the intrinsic physical properties of silicon, such as its indirect bandgap and moderate carrier mobility [26]. Moreover, its thermal conductivity limits its ability to dissipate heat effectively in high-power and high-frequency applications [22]. This thermal bottleneck can lead to overheating, reduced reliability, and shortened device lifespans.

In recent years, extensive research has spurred a shift toward exploring materials beyond silicon [27–30]. For the future of the industry and research, it will become much more important to conduct accurate assessments of the thermal properties of these materials and their nanodevices. Therefore, this section will explore alternative materials with a particular focus on their thermal characteristics.

1.2.1 Gallium arsenide and its nanostructures

Gallium Arsenide (GaAs) is a III-V semiconductor material composed of atoms from the third and fifth columns of the periodic table as a prominent alternative to silicon. GaAs is celebrated for its superior electronic features, including higher electron mobility and a direct bandgap [12]. Unlike silicon's indirect bandgap, GaAs's direct bandgap enables efficient light absorption and emission for higher performance in optoelectronics, such as lasers, LEDs, and solar cells [31,32]. Additionally, GaAs has a wider bandgap than silicon, which allows it to operate efficiently at elevated temperatures up to 400 °C [33].

In 1964, Holland pioneered the measurement of the lattice thermal conductivity of GaAs and theoretically validated it using the Callaway model at low temperatures [34]. This foundational work has paved the way for numerous investigations of GaAs's thermal properties. Bulk GaAs exhibits a thermal conductivity of approximately 50 W/mK, which is lower than that of silicon [35]. This property makes GaAs a better candidate for thermoelectric materials, combined with its high electron mobility [36].

The thermal conductivity of GaAs can be influenced by the film thickness and the effect of isotopic mass disorder. For instance, the thermal conductivity of GaAs nanofilms exhibits a marked decrease with the reduction in film thickness [37,38]. Additionally, a research conducted by Inyushkin et al. on GaAs crystal highly enriched with the isotope ^{71}Ga showed a 5 % higher thermal conductivity at room temperature compared to natural GaAs crystals [39].

The potential of this material is notably enhanced when utilized in nanostructures such as nanowires and superlattices, as shown in Figure 1.2 [40,41]. The design of these nanostructures enables the manipulation of thermal properties, leading to innovative thermal management strategies. Specifically, reduced dimensionality and increased surface-to-volume ratio of nanowires alter phonon transport mechanisms, which may modify thermal conductivity. With advancements in nanowire growth technology, it has been observed that the thermal characteristics of GaAs nanowires can vary significantly based on their length and diameter [42–44].

GaAs also has the advantage of easily forming superlattice structures with other III-V compounds, altering properties for application in a wide range of fields [45]. Several studies have shown that the periodic structure of GaAs/AlAs superlattices has a notable impact on thermal conductivity [46,47]. Building upon the combined structures, Juntunen et al. studied GaAs-AlAs core-shell nanowires. They measured the thermal conductivity of arrays of GaAs nanowires coated with AlAs shells, revealing that the AlAs shells suppress thermal transport, reducing it by up to approximately 60 % [48].

The study of phonon dynamics within GaAs has been a subject of continuous investigation, reflecting its critical role in understanding thermal properties. In 1990, Strauch and Dorner made the first experimental measurements of phonon dispersion in GaAs along a high symmetry point, including Gamma (Γ), X, L, and W [49]. Research into the lifetime of specific mode phonons in GaAs began in the 1970s [50,51]. Recently, Hamzeh and Aniel developed the Monte Carlo method with the Grüneisen constant to determine lifetimes that align with experimental results [52]. Moreover, numerous recent studies based on first-principles calculations have provided comprehensive insights into the dynamics of phonons, including the contributions from individual phonon modes, the accumulative thermal conductivity in relation to phonon mean free path, and variations across different temperatures and pressures [53–56].

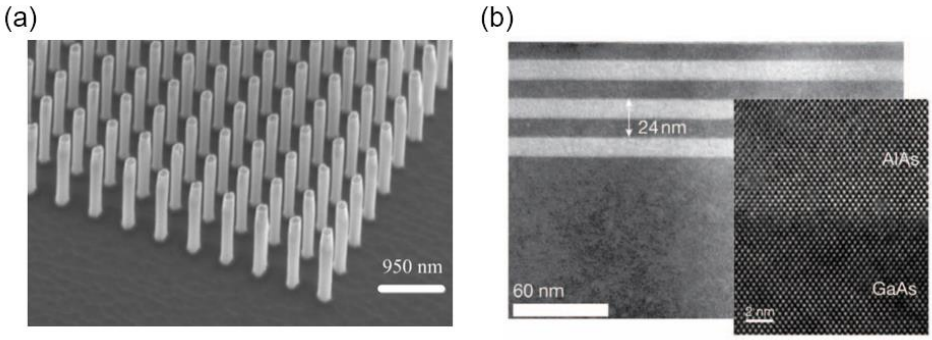

Figure 1.2 (a) The scanning electron microscope (SEM) images of GaAs nanowire array [40]. (b) Cross-sectional transmission electron microscope (TEM) images of GaAs/AlAs superlattices [41].

1.2.2 Exploring two-dimensional materials

As the quest for beyond-silicon technology drives research, materials with dimensions lower than bulk materials, specifically two-dimensional (2D) materials, have begun to capture significant attention [27,28]. Since Geim and Novoselov announced the first experimental isolation of graphene in 2004 [57], many other 2D materials have been studied, raising fundamental questions about low-dimensional systems and their potential applications [58]. In recent decades, a variety of 2D materials have been identified, encompassing single-element materials like graphene, black phosphorus, and silicene, as well as compound materials, including transition metal dichalcogenides (TMDCs) and hexagonal boron nitride (h-BN), as illustrated in Figure 1.3 [28].

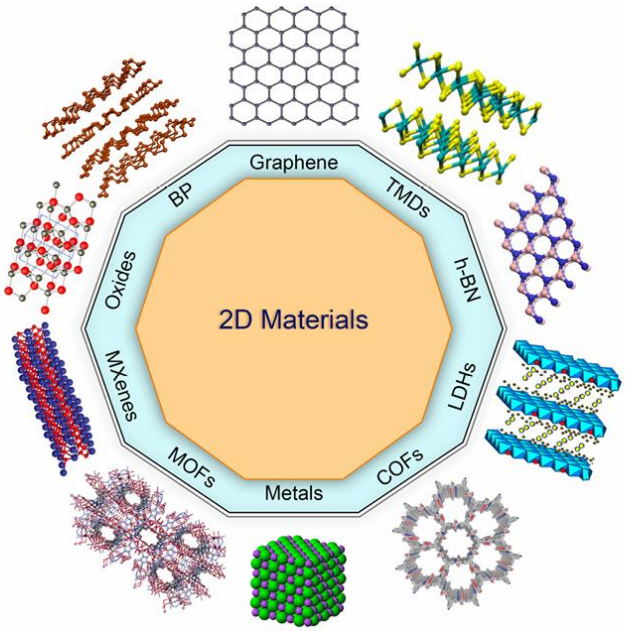

Figure 1.3 Classification of various two-dimensional (2D) materials showcasing a range of structures including graphene, hexagonal boron nitride (h-BN), transition metal dichalcogenides (TMDCs), black phosphorus (BP), etc. [28].

These 2D materials stand out due to extraordinary electrical, chemical, and mechanical properties. Moreover, the exploration of thermal properties in 2D materials has emerged as a critical focus within the field, driven by the distinctive thermal phenomena at the nanoscale [59]. Understanding these thermal characteristics is essential for advancing electronic systems, marking a significant step forward in applying 2D materials in next-generation technologies. In this section, we review the thermal characteristics of key 2D materials, including graphene, monolayer h-BN, and TMDCs. Additionally, heterostructures composed of distinct 2D materials are discussed because they could offer new physical properties, which are not present in the individual monolayer forms.

1.2.2.1 Graphene

Graphene is a monolayer of carbon atoms arranged in a hexagonal honeycomb lattice with excellent physical properties, including ultra-high electrical conductivity and carrier mobility [60]. In terms of thermal properties, graphene also has extraordinary thermal conductivity, which can reach up to several thousand W/mK. The first experimental measurement of the thermal conductivity of graphene was conducted by Balandin et al. in 2008, reporting room temperature values in the range of 4840 to 5300 W/mK, far exceeding that of typical bulk materials [61].

However, subsequent research indicated that thermal conductivity in graphene could vary significantly due to various factors such as sample quality, size, and measurement environment. For example, Wei et al. demonstrated a thermal conductivity value of approximately 2500±1100 W/mK at 350 K for graphene grown by chemical vapor deposition. [62]. These findings were further supported by various studies, including those by Chen et al. and Lee et al. in 2011, showing thermal conductivity values ranging from 1800 to 3100 W/mK [63,64]. Additionally, a relatively lower value of 840 W/mK was reported by Li et al. in 2017, highlighting the wide range of observed thermal conductivity values in graphene [65].

To understand the high thermal conductivity of graphene, it is crucial to explore the phonon dynamics. Given that graphene features a long phonon mean free path, extending to micrometer scales at room temperature, it facilitates phonon ballistic transport. This aspect was highlighted by Xu et al. in 2014, who provided experimental evidence for quasi-ballistic phonon transport in graphene [66]. After that, several theoretical studies have discovered that graphene exhibits clear hydrodynamic phonon transport across a broad temperature range through collective phonon excitations by strong normal scattering processes [67–69].

Regarding the contribution of each phonon mode to thermal conductivity, earlier research by Nika et al. suggested that the longitudinal acoustic (LA) and transverse acoustic (TA) phonon modes predominantly carry heat in graphene, while the contribution of the out-of-plane acoustic (ZA) phonon mode is negligible [70]. However, this perspective was later challenged by studies from Lindsay et al., who predicted that the thermal conductivity in graphene is dominated by contributions from the ZA phonon modes [71]. This significant role of ZA phonons was further confirmed when graphene was placed on a silicon oxide substrate, which notably suppressed the ZA mode, thereby reducing thermal conductivity [72,73].

The research on graphene and the exploration of its applications still continue. Its exceptional heat conduction capabilities make it an ideal candidate for thermal interface materials [74]. While its high thermal conductivity renders it less suitable for thermoelectric applications, Dollfus et al. highlighted that the poor thermoelectric performance of graphene could be improved through nanostructuring and bandgap engineering [75].

1.2.2.2 Hexagonal boron nitride

Hexagonal Boron Nitride (h-BN) is a material composed of alternating boron and nitrogen atoms arranged in a honeycomb lattice instead of carbon atoms in graphene [76]. Due to its crystal structure being similar to graphene, it is often referred to as 'white graphene'. The

atomically thin material form can be exfoliated from bulk h-BN crystals and is gaining importance due to its high chemical and mechanical stability, revealing a wide range of applications [77,78]. It also features a wide electronic bandgap, positioning it as an ideal dielectric material for electronic devices [79].

The thermal properties of h-BN are another aspect of great interest. Bulk h-BN exhibits thermal conductivity values of around 400 W/mK at room temperature [80,81]. In 2009, Alem et al. presented a method to prepare monolayer h-BN using mechanical exfoliation, thereby paving the way for the possibility of measuring the properties of h-BN in its monolayer form [82]. As early as 2011, a theoretical study by Lindsay et al. predicted the in-plane thermal conductivity of single-layer h-BN to be higher than 600 W/mK, surpassing that of bulk h-BN [83]. Notably, they found that the contribution of the ZA phonon mode is still significant, although smaller than that of graphene.

However, experimental measurements of few-layer h-BN have shown varying thermal conductivities, lower than theoretical predictions. For instance, Jo et al. measured the in-plane thermal conductivity of multi-layer h-BN, obtaining value of 250 W/mK for five layers [84], and Zhou et al. reported values ranging from 227 to 280 W/mK for nine layers [85]. The observed discrepancies between measured data and theoretical predictions were attributed to phonon scattering caused by polymer residues on the surface of h-BN samples.

Advancements in sample preparation methods employed by Wang et al. significantly reduced polymer residues on h-BN films. This approach allowed for the measurement of suspended bilayer h-BN thermal conductivity greater than the bulk material, achieving values between 460 and 625 W/mK at room temperature [86]. Further studies by Cai et al. explored the thermal conductivity of monolayer to trilayer h-BN near room temperature, with monolayer h-BN reaching thermal conductivity values of 751±340 W/mK [87]. The ongoing research and exploration into h-BN's thermal properties continue to reveal its potential for a wide range of applications, making it a material of significant interest in nanotechnology [88].

1.2.2.3 Transition metal dichalcogenides

Transition metal dichalcogenides (TMDCs) represent crystalline nanomaterials, characterized by their MX_2 composition, where M stands for a transition metal element (such as Mo, W, or Ti) and X denotes a chalcogen element (including S, Se, or Te). A monolayer of TMDCs features a sandwich-like structure with the transition metal layer between two chalcogen layers [89]. Bulk crystals of TMDCs are formed of monolayers held together by van der Waals forces. Although the first production of monolayer MoS_2 was achieved in 1986 [90], the interest in targeting monolayer and few-layer TMDCs gained significant momentum following the isolation of graphene in 2004 [91–93].

These materials have been actively studied due to their unique electronic, optical, and mechanical properties, which vary widely from metallic to semiconducting depending on their composition and structure, making them promising for nanoelectronics, optoelectronics, and energy conversion devices [94]. Unlike the previously mentioned two materials, TMDCs also exhibit distinct thermal properties attributed to the unique crystal structure of TMDCs and the difference in atomic masses between the transition metal and chalcogen atoms within these compounds.

Molybdenum disulfide (MoS_2) is one of the most extensively studied materials in this domain, notable for its bandgap transformation from an indirect gap in bulk form to a direct gap in a monolayer configuration [95]. Regarding its thermal characteristics, Sahoo et al. conducted the experimental measurement for the in-plane thermal conductivity of an 11-layer MoS_2 sample, which was found to be around 52 W/mK at room temperature [96]. Later, in 2015, Zhang et al. measured the thermal conductivity of single and double-layer MoS_2, finding that the single layer exhibited a thermal conductivity of 84±17 W/mK, while the bilayer displayed a value of 77±25 W/mK [97].

In theoretical predictions, a study by Li et al. in 2013 determined that the thermal conductivity of a typical 1 µm-sized monolayer MoS_2 at room temperature is 83 W/mK [98]. The research also highlighted that thermal conductivity could increase by 30 % in 10 µm-sized samples,

reaching around 108 W/mK. Additionally, Gu et al. in 2016 predicted that the room temperature in-plane thermal conductivity of a single layer of MoS_2 could achieve 138 W/mK [99]. Analogously, Hong et al., in the same year, found the thermal conductivity of MoS_2 to be 110.43 W/mK, using large-scale classical nonequilibrium molecular dynamics (NEMD) simulations [100].

Tungsten diselenide (WSe_2) has demonstrated utility for its electronic and optical properties, such as field-effect transistors and complementary inverters [101]. It interestingly exhibits a shift from an indirect to a direct bandgap as it transitions from bulk to monolayer form, similar to that observed in MoS_2 [102]. Notably, 2D WSe_2 has been identified as a promising candidate for thermoelectric applications, boasting a high Seebeck coefficient beyond that of commercial thermoelectric material Bi_2Te_3 [103].

Despite the considerable attention paid to its electrical and optical properties, experimental research on the thermal transport properties of 2D WSe_2 has been relatively scarce. In 2015, Kumar theoretically predicted the thermal conductivity of monolayer WSe_2 to be around 43 W/mK [104]. Building on this, recent experimental work by Easy et al. provided measurements of the thermal conductivities for single-layer, bilayer, and trilayer WSe_2 [105]. They discovered a trend in the layer-dependent lateral thermal conductivities, with the room-temperature thermal conductivities for single, bi-, and trilayer WSe_2 measured at 37±12, 24±12, and 20±6 W/mK, respectively.

As other examples, the thermal conductivities of various TMDCs have been measured, revealing significant diversity across materials. For tungsten disulfide (WS_2), thermal conductivity values were found to be 32 and 53 W/m·K for monolayer and bilayer configurations at 300K, respectively [106]. Monolayer molybdenum diselenide ($MoSe_2$) exhibited a thermal conductivity of 59±18 W/m·K [97], and tantalum diselenide ($TaSe_2$) with a thickness of 45 nm showed a notably low thermal conductivity of 9 W/mK [107]. The results of diverse TMDCs are comprehensively documented in the literature, highlighting the wide range of thermal conductivities [27,28,59].

Despite ongoing research, further investigation is required in various

aspects, including delineating the precise distinctions between the characteristics of bulk versus monolayer forms, the discrepancies between theoretical predictions and experimental findings, and expanding the scope of research to encompass out-of-plane thermal conductivity [108,109].

1.2.2.4 Two-dimensional heterostructures

Heterostructures composed of distinct 2D materials have garnered considerable interest due to their novel properties beyond the individual component and tunability to provide additional degrees of freedom for device engineering [27]. This emergence of new properties holds promise for developing high-performance, ultra-thin electronic devices, such as tunnel field-effect transistors [110]. The integration of 2D heterostructures also offers significant potential for enhancing thermoelectric performance and thermal management applications. This potential arises from an increased Seebeck coefficient and reduced thermal conductivity [111]. Moreover, the interfaces within heterostructures introduce deviations in thermal transport mechanisms compared to those observed in single 2D materials, opening the potential for innovation in various fields [112].

The synthesis of 2D heterostructures, achieved through various methods, including mechanical exfoliation and stacking, chemical vapor deposition (CVD), and molecular beam epitaxy (MBE), presents several challenges not typically encountered when working with single 2D materials [113,114]. One of the primary challenges is ensuring clean, defect-free interfaces between different 2D materials by controlling chemical reactions, contamination, or growth imperfections. Additionally, not all 2D materials can be easily combined due to differences in lattice constants (lattice mismatch) and thermal expansion coefficients, leading to potential incompatibility issues [115]. Finding compatible synthesis conditions is also difficult, given the variations in optimal growth temperatures and pressures among different materials. Furthermore, achieving desired stacking orders and orientations requires accurate control [116].

Despite these challenges, recent advancements in fabrication techniques have led to significant progresses in the synthesis of high-quality 2D heterostructures with atomically sharp interfaces and precisely controlled stacking arrangements [117,118]. Typically, 2D heterostructures are categorized into two classes: in-plane heterostructures and van der Waals (vdW) heterostructures [27]. In-plane heterostructures, also known as lateral heterostructures, are characterized by the seamless integration of two or more different 2D materials within a single plane, featuring sharp one-dimensional (1D) interface. Conversely, vdW heterostructures are comprised of distinct 2D materials stacked vertically, held together by the non-bonded vdW forces acting between adjacent layers.

In-plane heterostructures are at the forefront of research in materials science, marked by their well-matched electronic band structures and strong interfacial effect [27]. The minimal lattice mismatch between graphene and hexagonal boron nitride (h-BN) makes their in-plane heterostructures promising candidates [119]. Figure 1.4 (a) displays the experimental work by Liu et al. in 2013, which successfully demonstrated the growth of a perfect in-plane atomic scale continuity between graphene and h-BN, achieved through lithography patterning [120]. Despite the successful experimental synthesis of graphene/h-BN in-plane heterostructures, measuring their thermal properties, particularly the precise measurement of interface thermal conductance (ITC), remains a significant challenge [27]. Consequently, theoretical simulations have emerged as an essential tool for investigating the thermal properties of in-plane heterostructures. By focusing on phonon dynamics, these simulations offer invaluable insights into the mechanisms of interfacial thermal transport within these complex material systems.

For instance, Ong et al. reported that ITC in graphene/h-BN in-plane heterostructures is approximately 3.52 GW/m^{2}K at room temperature utilizing the atomistic Green's function (AGF) method [121]. Their findings also highlighted that the phonon transmission probability at the interface is notably high for longitudinal (LA) and flexural (ZA) acoustic phonons. In a similar study, Hong et al. explored the impact

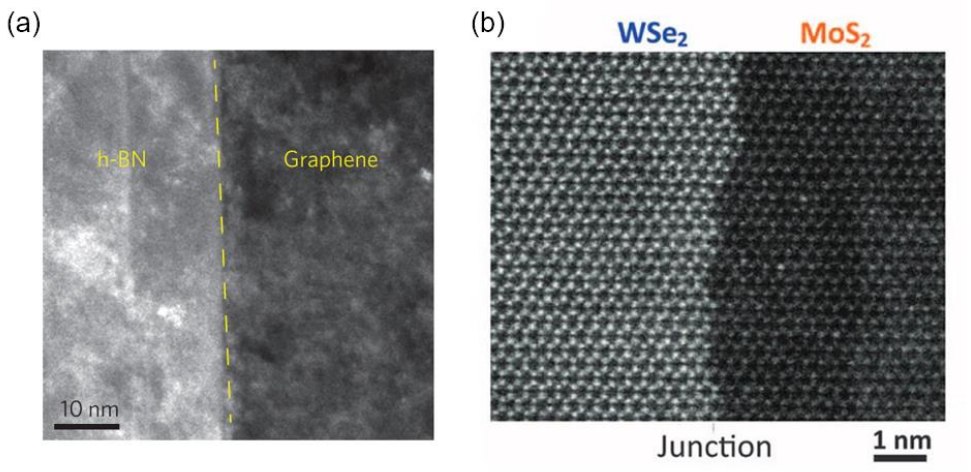

Figure 1.4 (a) Aberration-corrected annular dark-field (ADF) scanning transmission electron microscopy (STEM) image of a h-BN/graphene interface, where variations in material thickness are indicated by changes in image intensity [120]*, and (b) High-resolution ADF-STEM image of a laterally synthesized MoS_2/WSe_2 heterostructure showing a well-defined junction between the two materials* [125].

of sample length and ambient temperature on the ITC in graphene/h-BN in-plane heterostructures using the non-equilibrium molecular dynamics (NEMD) method [122]. They observed that the ITC fluctuates between 1.9 to 4.5 GW/m^{2}K for sample lengths ranging from 20 to 100 nm, with an increase in temperature significantly enhancing the ITC. Furthermore, Feng et al. conducted research on the temperature and thermal non-equilibrium of different phonon modes at graphene/h-BN planar interfaces [123]. Their findings indicated that the temperature jump for the ZA phonon mode accounts for only 10~20 % of the overall temperature jump across the interface. This minimal deviation is attributed to the significant overlap between the acoustic branches of graphene and h-BN. Conversely, the temperature jump for the flexural optical (ZO) phonon mode was as high as 220 % of the overall temperature jump.

Beyond graphene/h-BN in-plane heterostructures, the interfacial thermal transport properties of other 2D heterojunctions were also investigated. In 2017, it was found that the ITC of graphene/MoS_2 in-

plane heterostructures surpasses that of covalently bonded graphene/metal interfaces, with each Mo-C bond serving as a potential channel for heat transfer [124]. Li et al. successfully synthesized a lateral MoS_2/WSe_2 heterostructure through epitaxial growth, achieving sharply defined interfaces between the two materials, as shown in Figure 1.4 (b) [125]. Theoretically, Qin et al. in 2019 discovered that the ITC of MoS_2/WSe_2 in-plane heterostructures is approximately 10 % of that observed in graphene/h-BN heterojunctions, attributing this difference to strong phonon scatterings at the interface [126].

The thermal properties of vdW heterostructures have gained great interest due to their unique layered composition, which allows for the creation of vertical heterostructures with nearly defect-free interfaces. The advancement of innovative experimental methods has enabled the synthesis of vdW heterostructures through self-assembly technology, achieving remarkable precision [127]. This progress facilitates the assembly of complex devices that can be finely tuned by adjusting the stacking sequence, the relative rotation between adjacent layers, and the interlayer spacing [128,129].

In the study of bilayer graphene/h-BN heterostructures, Chen et al. measured the ITC, finding a value of 7.4 MW/m^2K at room temperature [130]. Similarly, Pak and Hwang determined the ITC at a graphene/h-BN interface to be 4.5 MW/m^2K, further noting that the thermal conductivity of graphene experiences minimal change when h-BN is introduced as a substrate [131]. Reinforcing these findings, Zhang et al. conducted NEMD simulations to assess the thermal conductivity of h-BN-supported graphene. Their research demonstrated that the system's thermal conductivity is only reduced by 23% compared to the suspended case, indicating that the force environment of graphene is scarcely affected by the h-BN substrate [132]. Moreover, the presence of periodic Moiré patterns on the graphene layer introduces a variable that can influence phonon transport within these heterostructures. When examining typical stacking configurations such as AA, AB, and AB′, Jung et al. determined that the AB stacking configuration offers superior properties compared to the AA stacking in graphene/h-BN vdW heterostructures through an analysis of phonon dispersion [133].

As other examples, Ma et al. predicted that the room-temperature thermal conductivity of a $MoS_2/MoSe_2$ bilayer heterostructure would be 25.4 W/mK, positioning it between the thermal conductivities of individual $MoSe_2$ and MoS_2 layers [134]. Employing the Raman optothermal technique, Liu et al. found that the ITC of a MoS_2/h-BN vdW heterostructure is about a third of that observed in graphene/h-BN heterostructures [135]. This difference is attributed to the lighter mass of carbon atoms in graphene, which allows for a broader frequency range for phonon transmission between the graphene and h-BN layers.

As the exploration of 2D heterostructures advances, numerous research challenges remain to be addressed. Theoretical calculations are still hindered by several limitations, including the computational cost and the complexity of accurately modeling vdW forces in density functional theory (DFT) calculations. On the experimental front, the journey towards accurately measuring the thermal properties of 2D heterostructures is far from complete. While several theoretical analyses have shed light on the potential of hybrid 2D materials, a deeper and more comprehensive understanding necessitates a broader spectrum of experimental data. Furthermore, the phenomena of anomalous non-Fourier transport require additional experimental verification.

1.3 MODELING HEAT TRANSFER AT THE NANOSCALE

1.3.1 Limitations of the classical description

The rapid development of nanodevices has underscored the need for a deeper understanding of their thermal properties. Heat energy transfer is at the heart of this exploration, necessitating a theoretical tool that not only elucidates the physics underlying these processes, but also facilitates predictive calculations. In the study of heat conduction, Fourier's law says that the heat flux across a material is proportional to the negative temperature gradient [136]. The material's ability to conduct heat, denoted by thermal conductivity, plays a pivotal role in this relationship. At macroscopic scales, Fourier's law has successfully captured thermal effects in large samples where the material properties are isotropic under steady-state conditions [137]. Its assumptions of linearity between heat flux and temperature gradient and its applicability to a wide set of geometries and boundary conditions have made it a fundamental tool in classical heat transfer analyses.

Over the past decades, the classical descriptions of heat transport, based on Fourier's law, have faced significant challenges due to phenomena theoretically and experimentally observed at the nanoscale [138]. Fourier's law, which traditionally models heat transport as a diffusive process, is valid only when phonons have mean free paths significantly shorter than the dimensions of the devices. However, when the mean free paths (MFP) of phonons become comparable to or exceed the sizes of these devices, the nature of heat transport shifts to ballistic [139]. This shift occurs because phonon MFP typically ranges from a few nanometers to tens of micrometers.

In complex nanostructures, especially those with internal interfaces, the thermal behavior is further complicated by different phonon scattering mechanisms [140,141]. The MFP of phonons is restricted by the physical boundaries, leading to non-uniform heat distribution and anisotropic thermal conductivity, which cannot be accurately described by traditional approaches. Another significant aspect of this complexity is the phenomenon of thermal boundary resistance at the interface. This resistance results from phonon interactions near

interfaces, such as reflection and transmission, which disrupts the thermal equilibrium and introduces non-equilibrium conditions. Its limitations also become evident in scenarios characterized by rapid spatial variations in temperature gradients and ultrafast time scales, such as those encountered in transient conditions [142]. This refers to situations where the system temperature changes over time due to external temperature bias or internal heat variations.

The limitations of the classical Fourier's law have propelled the development of more sophisticated models designed to accurately reflect the complexities of heat transfer. Among the notable extensions are the Cattaneo–Vernotte model and the Jeffreys-type model to better describe non-Fourier heat conduction behaviors [143,144]. While analytical methods have the potential to deliver exact solutions, the reality is that finding these solutions can often be time-consuming work or even impossible in some cases. In contrast, numerical simulation methods emerge as a practical alternative, capable of yielding reliable results efficiently. Unlike their analytical counterparts, numerical simulations have proven immensely valuable for tackling complex, multidimensional geometries and a wide array of boundary conditions [145]. The advent of advanced computational algorithms, coupled with powerful computing resources, has continued to improve the ability to perform accurate calculations. The next section will explore an overview of these simulation methods, shedding light on their pivotal role in contemporary thermal analysis.

1.3.2 Overview of simulation methods

To date, various simulation methods have been developed to study the thermal transport properties of multi-dimensional materials and diverse nanostructures, including density functional theory (DFT), the Boltzmann transport equation (BTE), the non-equilibrium Green's function formalism (NEGF), molecular dynamics (MD), Monte Carlo algorithm (MC), and finite element method (FEM) simulation [14,146,147]. These methods range from atomistic to continuum scales, as shown in Figure 1.5, each with its distinct foundational principles, advantages, and disadvantages. From a microscopic perspective, thermal transport is dominated by the behavior of phonons, quantized vibrations of atoms in the lattice. Therefore, phonons play a crucial role as thermal energy carriers, and their interactions, scattering

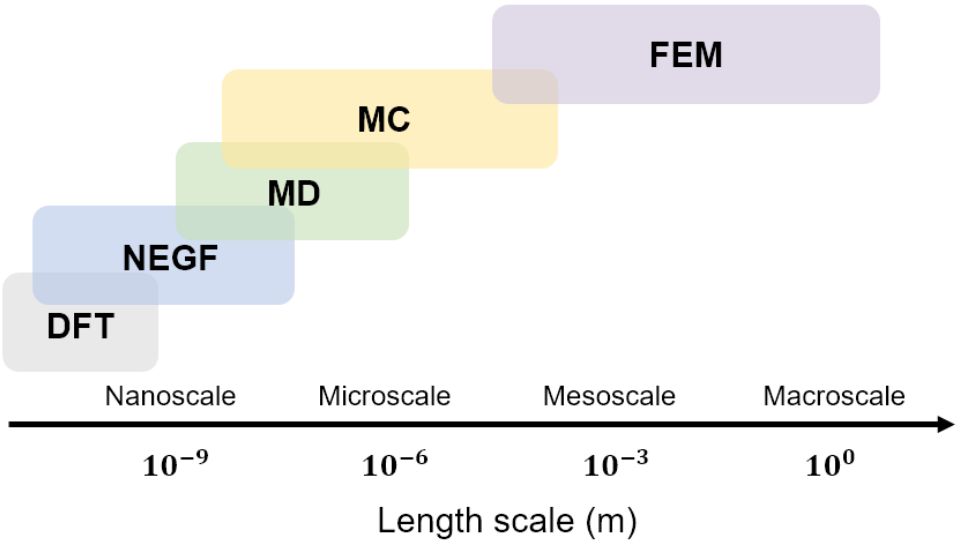

Figure 1.5 Schematic representation of the typical applicability ranges for various simulation methods across length scales. Density functional theory (DFT) and non-equilibrium Green's function formalism (NEGF) are most commonly utilized at the nanoscale, while molecular dynamics (MD) and Monte Carlo (MC) simulations span from the nano to microscales. The finite element method (FEM) is generally employed from meso to macroscales. These regions are approximate, indicating the flexibility and adaptability of each technique to different scales of analysis.

mechanisms, and propagation through materials are key factors determining thermal properties. The methods mentioned provide frameworks for analyzing these phenomena.

First principles calculation, also known as ab-initio method, is a quantum mechanical approach that requires no empirical parameters. The most common approach is density functional theory (DFT), which investigates the electronic structures of materials, particularly solids and molecules, by calculating the ground state in many-body systems [148]. Beyond the electronic structure calculations by DFT, analyzing the quantized vibrations of atoms within the lattice is important for understanding thermal properties based on density functional perturbation theory (DFPT). The foundation for DFPT was developed in 1987 by Baroni et al. [149]. They introduced a formalism that combines Green's functions with the principles of DFT to efficiently calculate the linear responses of solids to external perturbations for phonon dynamics. DFPT allows for the calculation of both harmonic (second-order) and anharmonic (third-order and higher) interatomic force constants, which are instrumental in deriving phonon dispersion relations and scattering rates [150]. Applicable across a broad spectrum of materials, including those yet to be fully understood or experimentally characterized, DFT and DFPT have significantly broadened the scope of computational research in material science, facilitating in-depth analysis of thermal properties. This technique's versatility is evidenced by its implementation across many software packages, such as Quantum ESPRESSO, ABINIT, and VASP [151–153].

Utilizing phonon properties and scattering rates derived from DFT calculations, the linearized Boltzmann transport equation (BTE) can be numerically solved to determine thermal conductivity. This approach incorporates various scattering mechanisms, including phonon-phonon, phonon-impurity, and phonon-boundary interactions. The research conducted by Lindsay et al. applied this approach to calculate the lattice thermal conductivity of various bulk materials, like Si, Ge, and GaAs, as well as technologically significant materials, such as SiC and AlN, demonstrating excellent agreement with experimental data [53]. Several studies have also reported that it can be applied beyond bulk materials to small nanostructures such as nanowires and superlattices [154–156]. Furthermore, it has been extended to studying

a wide range of 2D materials, including graphene, phosphorene, and TMDCs, offering insights into the fundamental mechanisms of heat transfer in these materials [68,83,157]. However, DFT simulations demand extensive computing resources, limiting their practical application to relatively small systems comprising only up to several hundred atoms. As a result, the application of DFT-based simulations to larger structures often requires simplifications or alternative methods to make the problem tractable.

The non-equilibrium Green's function formalism (NEGF) emerges as a comprehensive quantum mechanical framework rooted in many-body physics, elucidating quantum transport phenomena. NEGF transcends traditional methods by offering a coherent perspective on the quantum transport of systems via Green's functions. Among the most notable are the works of Keldysh in 1965, who played a significant role in the formal development of NEGF [158]. This formalism has been extensively applied to electron transport in nanoscale devices, enabling the detailed analysis of current-voltage characteristics, tunneling phenomena, and the effects of electron-electron and electron-phonon interactions [159–161]. After that, the approach has been also extended to study phonon transport dealing with both quantum and classical distribution for phonons. NEGF accurately calculates phonon transmission and heat conductance, incorporating the Landauer formula for ballistic systems [162]. It has proven its versatility and effectiveness across a broad spectrum of nanostructures [163,164], particularly suitable for heterostructures with interfaces [165,166]. One of the strengths of the NEGF formalism lies in its general applicability to any Hamiltonian. Furthermore, NEGF simplifies the inclusion of external interactions within the system through the concept of self-energy [167].

While NEGF offers precise insights into quantum transport phenomena, it presents a significant computational challenge. The primary drawback of NEGF lies in its intensive demand for computational resources, which restricts the size of the systems to only a few hundred or thousands of atoms [168]. As the complexity of the size of the system expands, the computational requirements escalate rapidly, hindering the study of larger-scale systems. Including anharmonic effects, such as phonon-phonon scattering, becomes also

computationally burdensome. Although recent advancements by Luisier have seen some implementations of anharmonic scattering within NEGF [169–171], such efforts require sophisticated self-consistent solutions that further compound the computational intensity of the approach. Moreover, capturing time-dependent or transient phenomena poses additional challenges, requiring dealing with time-dependent Green's functions compared to steady-state conditions.

Molecular dynamics (MD) is a powerful simulation technique in physics, chemistry, and materials science designed for structural, dynamic, and thermal properties. This method is especially useful in analyzing complex systems, including doping, defects, strain, and substrate influences. It employs Newton's equations of motion to predict the trajectories of atoms and molecules over time [172]. MD relies on determining interatomic potentials rather than quantum mechanical descriptions, making it a versatile tool for exploring phonon transport across both bulk materials and nanostructures. In the classical MD framework, the use of empirical interatomic potentials constrains its accuracy, especially at specific temperature ranges [173]. In response to this limitation, recent efforts have been directed toward developing reliable potential functions based on first-principles calculations [174]. Although these advanced potentials incorporate more accurate physical information, it is important to note that MD, being fundamentally classical, may not fully capture quantum mechanical effects critical at temperatures below the Debye temperature. This underscores the ongoing need to refine MD methodologies to understand complex thermal transport phenomena better, particularly those involving anharmonic effects.

Two types of MD simulations are typically employed to determine the thermal properties. The first, equilibrium molecular dynamics (EMD), investigates heat transfer in systems at equilibrium. Within EMD, the Green- Kubo relations play a crucial role, enabling the extraction of thermal properties such as thermal conductivity from the system's equilibrium fluctuations through statistical mechanics frameworks. For instance, Volz and Chen successfully calculated the thermal conductivity of silicon crystals within systems containing several thousands of atoms using the EMD method [175]. Zhong et al.

conducted the calculation of the thermal conductivity in nanostructures like nanofilms and nanowires, revealing a significant dependence on their characteristic size [176]. This methodology has also elucidated the detailed spectral dependence of phonon transport properties in bulk silicon [177] and proved invaluable in studying low-dimensional materials [178]. However, EMD's requirement for prolonged simulation times to achieve statistical convergence may limit its effectiveness in analyzing complex structures, particularly those with impurities, interfaces, or non-equilibrium states.

Compared to the EMD, non-equilibrium molecular dynamics (NEMD) offers a direct method for measuring thermal responses under non-equilibrium conditions, such as those induced by temperature gradients or external forces. A notable simplification of this method for thermal conductivity calculation under a temperature gradient was introduced by Müller-Plathe in 1997 [179]. Since then, NEMD simulations have been widely applied to investigate a variety of materials and nanostructures [180–182]. Notably, Xu et al. highlighted this technique's capability to elucidate the length-dependent thermal conductivity of suspended single-layer graphene, thereby demonstrating its crucial role in advancing our fundamental understanding of thermal transport in 2D materials [66]. Additionally, NEMD has proven exceptionally useful in examining interface-modulated phonon dynamics across different heterostructures [183,184]. However, this approach demands a sophisticated setup to yield reliable and interpretable outcomes, with its application generally limited to systems of up to tens of thousands of atoms.

In summary, MD simulations, encompassing both equilibrium and non-equilibrium methodologies, enhance our atomic-scale understanding of complex systems larger than those manageable with DFT and NEGF approaches. Recent advances in computational capabilities and algorithms, notably through the incorporation of machine learning techniques for improving atomic potential calculations, are significantly expanding the applicability and precision of MD in investigating complex material behaviors and transport phenomena [185].

The Boltzmann transport equation (BTE) is a foundational element in

the study of transport phenomena, providing a detailed account of the movement and interaction of particles such as electrons, phonons, and photons. Historically, it was initially formulated by Boltzmann in 1872 as a fundamental equation to describe the dynamics of gas molecules [186]. This groundbreaking work paved the way for further developments, notably by Peierls in 1929, who adapted the BTE to specifically address phonon transport in crystalline solids [187]. The primary principle of the BTE is its ability to describe the time evolution of the probability distribution function, incorporating scattering processes that impede carrier transport. This distribution function quantifies the number density of particles within phase space, portraying carriers as point-like entities. This treatment enables the BTE to effectively model transport phenomena through the statistical behavior of numerous particles rather than the specifics of individual particle states [14].

Solving the BTE to deal with the non-equilibrium phonon distribution is notably challenging due to its integral-differential nature and the collision term, demanding sophisticated analytical approaches for its solution. A frequently adopted strategy is the relaxation time approximation (RTA), which simplifies the collision term to depend on a singular parameter, namely the relaxation time [188]. At non-equilibrium introduced by a small temperature gradient, the phonon distribution function diverges from the equilibrium distribution dictated by Bose-Einstein statistics. Under RTA, this deviation can be linearly approximated, effectively capturing the initial deviation from equilibrium. The RTA framework enables the integration of multiple scattering events, including phonon-phonon, phonon-impurity, and phonon-boundary interactions, utilizing Matthiessen's rule, which assumes that these scattering mechanisms are considered independent.

Following the pioneering works by Holland [189], which evaluated the efficacy of the RTA for Si and Ge, this framework has been extensively applied to investigate the thermal conductivity across a broad spectrum of materials [55,190,191]. The RTA has gained popularity for its ability to effectively capture phonon dynamics, thereby providing a valuable tool for interpreting thermal transport results. However, McGaughey and Kaviany have pointed out that assuming simple

isotropic phonon dispersions in this framework, could lead to inaccurate outcomes [192]. Mingo demonstrated the utility of this method with complete phonon dispersions, achieving good agreement with experimental results for Si nanowires without the need for any externally imposed frequency cutoffs [193].

In addressing the complexities of phonon transport, it is observed that RTA techniques sometimes yield thermal conductivities lower than experimental values [194]. This discrepancy arises because such methods fail to differentiate between momentum-conserving normal processes and momentum-nonconserving Umklapp processes. Typically, in bulk materials like Si and Ge, the Umklapp process dominates, yet at low temperatures, the normal process becomes more significant, leading to enhanced wave-like transport in what is known as the hydrodynamic regime. This phenomenon is also experimentally and theoretically observed in 2D materials at room temperature, with graphene demonstrating clear hydrodynamic phonon transport across a broad temperature range due to collective phonon excitations driven by strong normal scattering processes [195,196].

To handle the complexity of the scattering term, which stems from the non-Fourier nature of phonon transport, one common analytical solution is a dual relaxation model proposed by Callaway [197]. This model simplifies the scattering term by assuming that the normal process and the resistive process, including Umklapp ones, independently restore the phonon distribution function to a displaced Planck distribution and a Planck distribution, respectively. The model's ability to separately consider normal and resistive phonon scattering allows it to describe heat transport from the hydrodynamic to the diffusive regime [198,199]. For instance, Cepellotti et al. successfully demonstrated its effectiveness for accurate description of thermal transport in 2D materials at a wide spectrum of temperatures [69].

Beyond the RTA frameworks, iterative solutions to the BTE represent another approach that handles complex scattering mechanisms [200]. This method meticulously refines the distribution function through successive iterations until a self-consistent solution is attained, providing an accurate understanding without relying on the

oversimplifications tied to RTA. The first efforts for an exact solution to the linearized BTE were introduced by the seminal work of Omini and Sparavigna [201]. Later, Fugallo et al. advanced this algorithm by joining the variational principle, assuring the mathematical stability [202]. Such iterative techniques have proven superior to the RTA, particularly for materials with high thermal conductivity or at low temperatures where the normal scattering process is dominant [69]. While iterative methods offer enhanced accuracy, they are computationally more demanding than RTA [203]. Furthermore, convergence is increasingly challenging in systems with complex structures or where various scattering processes are strongly coupled.

Indeed, the methods mentioned above for solving the BTE have limitations in capturing the full complexity of transport phenomena, except for simple systems. Therefore, numerical solutions become essential, including detailed scattering mechanisms, complex boundary conditions, and realistic device geometries. The most widely used numerical methods include a discrete ordinates method, a finite volume method, and Monte Carlo simulations [204–206]. Among the numerical solutions for the BTE, Monte Carlo (MC) simulations stand out as a powerful technique for modeling the stochastic nature of phonon transport in materials [188]. This method excels in investigating thermal transport properties by statistically simulating the random trajectories of phonons. It adeptly manages complex interactions with other phonons, defects, boundaries, and interfaces across complicated geometries. The MC method bases these simulations on probability distributions derived from the physical scattering mechanisms described by the BTE.

Originally developed as a numerical solution for the Boltzmann equation in the realm of electron transport, the MC approach gained prominence through the comprehensive overview provided by Jacoboni and Reggiani in 1983, focusing on charge transport problems in semiconductors [207]. This work became a cornerstone reference for the method's application in various fields. In 1994, Peterson applied the MC method to simulate the phonon heat conduction process under the Debye approximation [208]. This was achieved using a linear array of cells to model a one-dimensional heat transfer problem, aiming to determine the steady-state heat transfer.

Early studies of bulk materials frequently relied on the assumption of simple isotropic phonon dispersions in MC simulations [206,209]. This approach has been expanded upon by subsequent studies that have adopted a full-band phonon dispersion throughout the entire 3D Brillouin Zone, revealing that the isotropic assumption could lead to substantial deviations [210,211]. Subsequently, the MC simulation technique saw significant enhancements, particularly through the advanced treatment of three-phonon scattering processes and boundary conditions [206,212]. A notable advancement in MC algorithm development was achieved through the work of Péraud and Hadjiconstantinou in 2011 [213]. Their methodology introduced an energy-based variance-reduced method, significantly reducing computational costs and naturally embedding exact energy conservation into the algorithm.

Regarding the treatment of boundary conditions, it has evolved significantly over time. One of the earliest considerations of how geometric confinement affects phonon transport was introduced by Casimir, which led to a thermal conductivity that is proportional to the total specific heat and the sample size [214]. His model provided a foundational perspective on the role of boundaries in thermal transport. Building on these concepts, Soffer developed a probability-based model for phonon reflections at surfaces, effectively distinguishing between specular (mirror-like) and diffuse (randomized direction) scattering of phonons upon encountering a boundary [215]. This model expressed that the likelihood of specular versus diffuse scattering is determined by the phonon's incident wave vector along with empirical parameters such as the surface roughness standard deviation and the correlation length. More recent approaches have involved designing external boundaries in real space with realistic profiles, such as a saw-tooth shape [216], which have yielded results that closely align with experimental observations [217].

MC simulations have also demonstrated their versatility by studying heat conduction both in steady and transient states. In principle, the MC method operates as a transient analysis technique, characterizing steady-state processes through the extensive simulation of extended transient dynamics. For example, Lacroix et al. employed this method to simulate transient heat conduction within silicon nanofilms in the

diffusion and ballistic regimes within silicon and germanium nanofilms [206]. Furthermore, the potential of MC simulations to investigate transient heat conduction can open up opportunities for comparison with experimental observations, such as those obtained from ultrashort pulse laser heating processes in time-domain thermoreflectance (TDTR) measurements [213].

The accuracy of MC simulations is deeply connected to the precision of input parameters, such as dispersion properties and phonon lifetimes. As previously mentioned in the context of DFT, integrating DFT calculations in MC simulations solving the BTE enhances the accuracy and predictive power of simulations. This eliminates the need for empirical adjustments, making the method particularly suitable for exploring thermal transport in materials with unknown or intricate properties, as highlighted by Chaput et al. and Yang and Minnich [218,219]. In summary, the strength of the MC method in elucidating nanoscale heat conduction has been convincingly proved across a spectrum of nanostructures, including porous nanofilms, nanowires, and nanoribbons, among others, showcasing its applicability to a diverse range of materials and geometries [220–222]. Therefore, the MC simulation is firmly established as a cornerstone method in the study of thermal properties coupled with its flexibility in application. However, one notable drawback of the MC simulation technique is its substantial demand for computational resources when applied at the macroscale to achieve accurate results due to statistical noise.

To handle continuum heat transfer on a large scale, the finite element method (FEM) is a powerful and widely used numerical technique by discretizing a continuum domain into smaller, manageable elements [223]. This discretization process transforms the differential equations that govern the system into a coherent set of algebraic equations. Through its element-based framework, FEM delivers detailed insights into localized phenomena, offering precise information on stresses, strains, and temperature gradients. Its capacity to address multiphysics problems is particularly notable, facilitating the simultaneous consideration of interactions between diverse physical phenomena, such as mechanical, thermal, and electromagnetic forces. Noteworthy applications include the work by Hamian et al., who demonstrated the utility of FEM in computing ballistic–diffusive phonon heat transfer and

integrating these findings with multiphysics analyses at the micro and nanoscale [224]. Furthermore, Gu and Wang presented a hybrid approach that combines an atomistic Green's function method with FEM to analyze ballistic phonon transport in devices of arbitrary geometries, illustrating how FEM can transform a continuous system into a lattice system when discretized [225]. Despite its strengths, its computational cost can become challenging when a highly refined mesh is needed to accurately model small-scale phenomena. Additionally, the precision of FEM results heavily relies on the quality of the mesh and the reasonable choice of element types because suboptimal meshing may lead to approximation errors.

In conclusion, each simulation method offers unique strengths and is suited to particular thermal transport problems. The choice of simulation method depends on the specific requirements of the study, including the scales of interest, the material properties, and the available computational resources. Advances in computational techniques and hardware continue to expand the capabilities and applications of these simulation methods in thermal transport.

1.3.3 Modeling for the solid-solid interface

Interfaces between materials significantly influence phonon dynamics, playing a pivotal role in determining the thermal properties. This impact is magnified in nanoscale systems, where the relative effect of interfaces on material properties can be more pronounced compared to those in the bulk [226,227]. Historically, in 1941, Kapitza conducted systematic investigations into the thermal interface behavior in liquid helium, thereby introducing the concept of interface thermal resistance, or Kapitza resistance [228]. This resistance arises from the mismatch in the vibrational properties of the materials on either side of the interface, leading to carrier scattering and resultant temperature drops across the interface.

Understanding thermal transport across interfaces, characterized by Kapitza resistance, is vital, especially with the advent of nanotechnologies. For instance, low thermal resistance interfaces are essential in high heat dissipation scenarios, whereas high thermal resistance interfaces are beneficial in applications requiring thermal isolation. Traditional Fourier's theory fails to adequately describe interfacial thermal transport, particularly in nanostructured devices [229]. Thus, innovative simulation methods are required to consider how phonon reflection and transmission at the interface prevent thermal equilibrium, featuring rapid spatial variations in temperature gradients for thorough exploration.

For studying interface thermal resistance, primarily focusing on solid-solid interface, advanced atomistic ab-initio methods, molecular dynamics (MD), and the non-equilibrium Green's function (NEGF) approach have been employed [230,231]. While these modeling techniques can provide detailed insights into interfacial thermal transport, their extensive computational requirements, limitations at varying temperatures, and issues related to length or time scales constrain their broad application [232].

Two foundational approaches for evaluating thermal resistance and conductance at solid-solid interfaces are the acoustic mismatch model (AMM) and the diffuse mismatch model (DMM) [233]. The AMM, initially developed by Little, assumes an ideal interface that maintains

wave coherence with specular scattering, reflecting a geometrically perfect interface where phonon transport is entirely elastic [234]. This model is instrumental in elucidating phonon transmission across smooth interfaces. On the other hand, Swartz and Pohl introduced the DMM, which assumes interfaces are entirely diffusive due to roughness or defects, causing diffuse scattering and a loss of wave coherence [235]. Each phonon traversing the interface experiences a diffusive scattering process, leading to a loss of memory of its incident properties. Recent developments include the full-band (FB) extensions of these models, enhancing analysis by integrating the complete phonon spectrum. For instance, Larroque et al. have expanded the AMM [232], while Reddy et al. have extended the DMM into its FB form [236]. Despite their differing assumptions, both models utilize a Landauer approach to consider the transmission of phonons. A key aspect in both AMM and DMM is the importance of phonon state overlap in determining thermal resistance, with an explicit neglect of inelastic scattering.

Zhang et al. investigated the phonon transmission across the Si/Ge interface, showing that the AMM yields results similar to those from the atomistic Green's function method at low temperatures [237]. Within the same structural context, Larroque et al. discovered that the results from the DMM more closely matched experimental data than those obtained from the AMM [232]. Although AMM and DMM, including their full-band extensions, may not always offer precise predictions of thermal interface resistance under all conditions, they serve a critical role in framing the expected behavior within reasonable bounds. In addition, these models can be seamlessly integrated into the MC framework, enabling different and flexible simulation capabilities that support a broad range of investigations into thermal phenomena in nanostructures with less computational complexity.

Lastly, in determining interface thermal conductance (ITC), it's essential to account for the appropriate temperature difference at the interface by considering strong non-equilibrium phonon states near it. To address this complexity, Maassen and Lundstrom proposed using forward and reverse heat fluxes along with their corresponding temperatures, referred to as hemispherical or directional temperatures [238]. Building on this concept, in 2022, Davier et al. redefined the

interface thermal conductance using directional temperatures instead of the conventional pseudo-temperature based on Bose-Einstein statistics [239]. This novel approach has proven to be a promising solution, matching the ITC results with the predictions from the analytical model in silicon-based heterostructures [240,241].

1.4 MOTIVATION OF THE THESIS

In advancing our understanding of phonon transport in nanostructures, this thesis is motivated by the complex interplay of thermal phenomena at the nanoscale, a realm where traditional heat transfer models encounter significant limitations. As devices shrink to the nanoscale, efficient heat management becomes paramount, with phonon dynamics playing a crucial role in determining the thermal properties of semiconductor materials.

According to the trend towards more compact and high-performance devices beyond conventional silicon-based technology, there has been a surge in research exploring alternative materials such as compound and two-dimensional (2D) materials, each offering distinct advantages over silicon. For instance, gallium arsenide (GaAs), featured with higher electron mobility and direct bandgap, holds promise for next-generation electronic devices due to its suitability for nanostructures such as nanowires and superlattices. Similarly, 2D materials like graphene and hexagonal boron nitride (h-BN), along with transition metal dichalcogenides (TMDCs), including molybdenum disulfide (MoS_2), and tungsten diselenide (WSe_2), have gained attention for their exceptional electrical, thermal, and mechanical properties. Despite the ongoing research exhibiting potential for broad applications across various fields, the study of thermal transport properties in these materials has been relatively underexplored.

Moreover, heterostructures composed of various 2D materials have emerged as particularly intriguing due to their novel properties beyond those of individual components and their flexibility for device engineering. Although experimental efforts have successfully fabricated both in-plane and van der Waals (vdW) heterostructures, accurately measuring their thermal properties remains challenging. Notably, experimental assessment of thermal properties in lateral heterostructures poses more difficulties than in van der Waals heterostructures. Therefore, advanced simulation techniques have become crucial for examining the thermal properties of in-plane heterostructures, offering detailed insights into phonon dynamics and interfacial thermal transport.

As discussed in Chapter 1, the classical Fourier's law exhibits clear limitations within the context of nanoscale devices where the mean free paths of phonons can become comparable to the sizes of these devices. This issue, coupled with complex nanostructures and internal interfaces, introduces further challenges due to various phonon scattering mechanisms. In response to these challenges, this thesis explores phonon transport in nanostructures using stochastic MC simulations based on ab-initio parameters. DFT provides a quantum mechanical calculation of material properties, such as full-band phonon dispersion, group velocity, and scattering rates in the first Brillouin zone. Incorporating DFT-derived parameters into MC simulations enhances the reliability of these stochastic models, enabling them to capture the complex interplay of phonon behavior. This numerical approach can integrate a wide range of scattering mechanisms, including phonon-phonon, phonon-impurity, and phonon-boundary scatterings through the relaxation time approximation. Moreover, the stochastic nature of MC simulations makes them particularly suited for investigating non-equilibrium thermal phenomena, such as transient thermal responses and temperature gradients across interfaces.

In Chapter 2, we review the theoretical foundations of ab-initio calculations, highlighting the essential role of DFT and its core principles. It further elucidates the application of DFPT for phonon calculations, a crucial step in predicting lattice dynamics. The chapter progresses to address anharmonic effects, pivotal for accurately determining thermal conductivity through the analysis of three-phonon scattering processes, utilizing the Quantum ESPRESSO suite for a comprehensive full-band description of materials from DFT to DFPT. Additionally, this chapter explores MC algorithms to solve the Boltzmann transport equation for phonons, detailing how phonon scattering mechanisms are addressed and how temperatures are defined within this framework. This includes a discussion on calculating thermal conductivity and interface thermal conductance. To complement these numerical methods, several analytical models are examined as benchmarks for comparing the outcomes of MC simulations.

Following the methodology outlined in the previous chapters, we begin to present the calculated results. Starting with Chapter 3, a comprehensive examination of the thermal properties of GaAs nanostructures is conducted. This chapter explores the variations in phonon transport mechanisms influenced by device dimensions, boundary conditions, and temperatures. Initially, we demonstrate the material properties of GaAs calculated by DFT and validate the accuracy by comparing the thermal conductivity of bulk GaAs against experimental data. Then, we design various GaAs nanostructures by establishing specific boundary conditions and examine their thermal behavior. This examination spans across cross-plane and in-plane nanofilms, as well as nanowires, illustrating how boundary conditions influence thermal conductivity in relation to both device dimension and temperature. A particular focus is placed on illustrating the transition from ballistic to diffusive transport regimes, offering critical insights into the modal contribution of each phonon mode. Through sophisticated design, we also introduce nanopores within nanowire structures to further investigate their impact on the thermal conductivity of GaAs nanowires.

Chapter 4 advances the investigation into the thermal transport properties of novel 2D materials and their lateral heterostructures, such as those formed by h-BN, graphene, MoS_2, and WSe_2 in monolayer configurations. Reflecting the approach of the previous chapter, this chapter introduces the material properties of each 2D substance, including phonon dispersions, velocities, and scattering rates. A thermal conductivity analysis, combined with experimental data, validates the accuracy of the DFT calculations. Focusing on the intricacies of lateral heterostructures, specifically h-BN/Graphene and MoS_2/WSe_2 combinations, the chapter delineates the impact of lateral interfaces on thermal transport, as modeled by the diffuse mismatch model (DMM). This chapter focuses on exploring interface thermal conductance (ITC) and the phonon modal contributions near the interface, employing the concept of directional temperature to yield precise ITC calculations and unravel the complex thermal dynamics within these heterostructures.

Finally, Chapter 5 investigates the transient thermal response in 2D h-BN/graphene lateral heterostructures with a length of 100 nm. This

study aims to interpret the heat transfer mechanisms within the transient regime to understand the initial behavior due to an external bias and its progression to a steady-state. First, the unique material properties of h-BN and graphene that are crucial for transient thermal analysis are described. The chapter discusses variations in heat flux density and temperature over time at specific positions and introduces a semi-analytical model for transient response based on directional temperatures. It also provides detailed relaxation, delay, and rise times calculations to characterize the temporal response and quantifies mode-dependent thermal behaviors. Through comparisons with homogeneous h-BN and graphene nanofilms without interfaces, this study illustrates how interfaces within the heterostructures significantly impact the transient thermal response.

2 METHODOLOGY

Chapter 2 comprehensively analyzes the computational and theoretical frameworks used for simulating phonon transport in nanostructures. Section 2.1 begins with an overview of ab-initio calculations, emphasizing the pivotal role of density functional theory (DFT) and its foundational principles, including the Hohenberg-Kohn theorem and Kohn-Sham equations (2.1.1). Section 2.2.2 progresses to detail density functional perturbation theory (DFPT) for phonon calculations in predicting lattice dynamics. Furthermore, we also detail non-linear phonon interactions that significantly influence thermal transport mechanisms (2.1.3).

Next, Section 2.2 explores the implementation of Monte Carlo simulations to solve the Boltzmann transport equation (BTE), focusing on phonon transport simulations. This includes discussions on the application of the relaxation time approximation (2.2.1) and phonon scattering mechanisms (2.2.2). Additionally, it addresses the challenges of defining temperatures within simulations (2.2.3). Building on this foundation, we introduce Monte Carlo algorithms (2.2.4) and methodologies for calculating thermal conductivity and interface thermal conductance (2.2.5). Concluding the chapter, several analytical models are discussed as benchmarks for comparing the outcomes of Monte Carlo simulations.

2.1 AB-INITIO CALCULATIONS FOR MATERIAL DESCRIPTION

2.1.1 Density functional theory

The accuracy of carrier transport simulations depends on a precise full-band description of materials. There are two different material modeling approaches: 'top-down' and 'bottom-up'. Firstly, the 'top-down' approach involves extracting empirical laws by fitting experimental measurements. While practical, this method often fails to provide fundamental insights into the underlying quantum mechanical interactions [242]. It also lacks the ability of predict the physical properties of materials whose empirical parameters are unknown. In contrast, the 'bottom-up' strategy seeks to predict material properties without relying on empirical parameters. Since the latter is rooted in quantum mechanics through the solution of a complicated Schrödinger equation, it is also referred to as 'ab-initio method' or 'from first principles'. However, except in the simplest case of a hydrogen atom, the direct solution of the many-body Schrödinger equation becomes exponentially complex as the size of the system increases.

Among various theoretical and computational techniques to address this challenge, density functional theory (DFT) is a very effective technique that transforms the many-body problem into a simplified form, focusing on electron density rather than the many-body wavefunction. Historically, the foundation of DFT dates back to a published paper by Hohenberg and Kohn in 1964 [243]. Hohenberg-Kohn theorem, which forms the basis of DFT, can be summarized on the following two premises. The first premise is that the electron density, which defines the ground state properties of any system of interacting particles, is uniquely determined by an external potential, such as the arrangement of nuclei. Although this premise is not intuitive, it can be proven by reduction to absurdity. They demonstrated that if two different external potentials were to yield the same ground-state electron density, it would lead to a contradiction. The second premise comes from a variational principle for the electron density. This implies that the ground state density minimizes the energy functional. In other words, the ground-state energy functional reaches its minimum only if the electron density corresponds to that

of the ground state. Therefore, this theorem explains that the ground state energy of a many-electron system can be determined solely from its electron density.

While the Hohenberg-Kohn theorem established the theoretical framework, it did not provide specific methods to calculate the electron density. The Kohn-Sham equation, introduced by Kohn and Sham in 1965, addresses this by providing the Schrödinger-like equation that generates the same electron density as any given system of interacting particles [244]. The Kohn-Sham equation for single particle can be described as follows:

$$\left[-\frac{\hbar^2}{2m}\nabla^2 + V_{ext}(r) + V_{Hartree}(r) + V_{xc}(r)\right]\phi_i(r) = \varepsilon_i\phi_i(r) \qquad (2.1)$$

where the first term is the kinetic energy operator, the external potential, V_{ext}, the Hartree potential, $V_{Hartree}$, and the exchange-correlation potential, V_{xc}. ϕ_i and ε_i are wavefunctions and eigenvalues of the i-th orbital at the point r, respectively.

From the solutions of the Kohn-Sham wavefunctions ϕ_i, the electron density n is computed by summing up the probabilities of finding electrons in each occupied state i at point r:

$$n(r) = \sum_i |\phi_i(r)|^2 \qquad (2.2)$$

Regarding the definition of each potential in equation 2.1, the external potential V_{ext} is the Coulomb potential experienced by electrons due to external charges, typically the positively charged nuclei. This term represents the primary 'external' influence on the electron cloud.

The Hartree potential $V_{Hartree}$ accounts for the electrostatic electron interaction with the mean-field approximation. This potential satisfies Poisson's equation since it is the 'average' potential experienced by each electron:

$$\nabla^2 V_{Hartree}(r) = -4\pi n(r) \qquad (2.3)$$

The formal solution of equation 2.3 is given by:

$$V_{Hartree}(r) = \int dr' \frac{n(r')}{|r - r'|} \tag{2.4}$$

From a mathematical point of view, it is expressed as an integral over the electron density, reflecting the cumulative effect of all electrons.

The exchange-correlation potential V_{xc} is the most complex term which takes into account the Pauli exclusion principle and correlation effects among electrons in a many-electron system:

$$V_{xc}(r) = \frac{\delta E_{xc}[n(r)]}{\delta n}\Big|_{n(r)} \tag{2.5}$$

where E_{xc} is the exchange-correlation energy which is a functional of the electron density $n(r)$.

In order to solve the Kohn-Sham equation, constructing accurate exchange and correlation functionals is required. However, the exact form of this potential remains unknown, necessitating various approximate functionals such as the local density approximation (LDA), the generalized gradient approximation (GGA), and hybrid functionals [148,245–247]. Among them, the most commonly used and simplest approximation are the LDA. This approximation simplifies the complexity of the exchange-correlation potential by assuming that the electron density varies smoothly with real space:

$$E_{xc}^{LDA}[n(r)] = \int_V \frac{E_{xc}^{HEG}[n(r)]}{V} dr \tag{2.6}$$

where 'HEG' denotes homogeneous electron gas. For homogeneous electron gas, it is possible to calculate the exact exchange-correlation energy using numerical techniques. Then, the energy of the entire system can be obtained by adding up the individual contributions from each volume element V based on homogeneous electron gas of densities.

In the framework of DFT, the ground state electron density is determined through a self-consistent field (SCF) iterative process, as shown in Figure 2.1. This process begins with the determination of the external potential by specifying the atomic positions of the material.

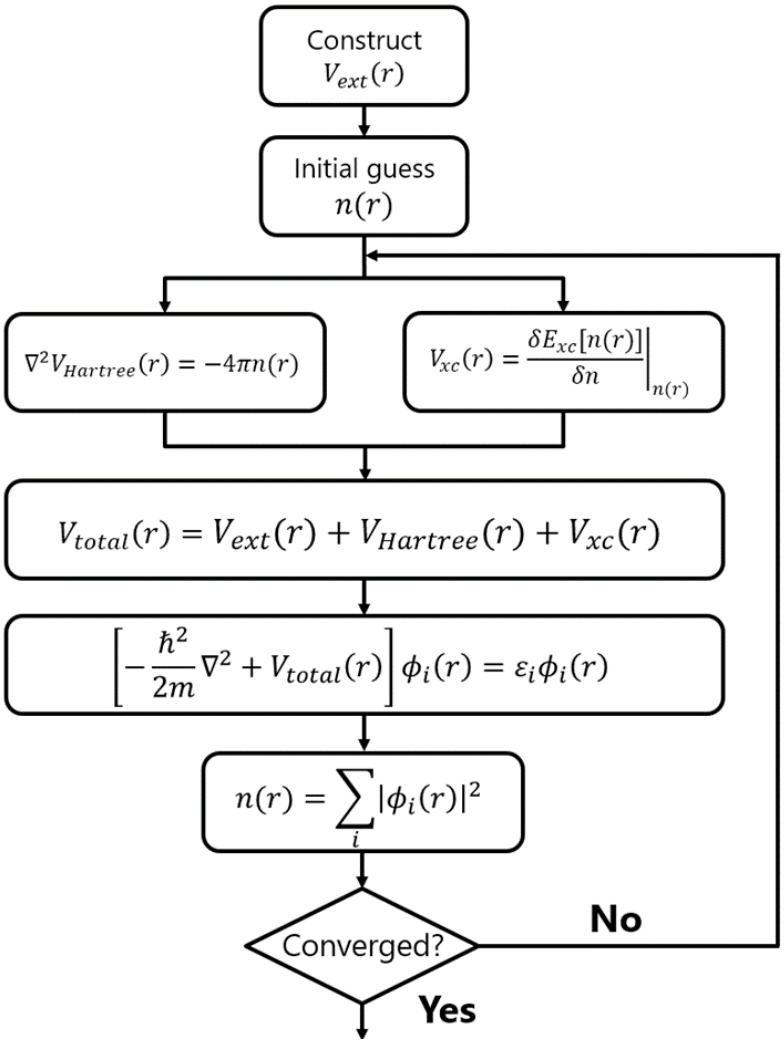

Figure 2.1 Schematic flowchart for finding self-consistent solutions of the Kohn–Sham equations (see equations 2.1~2.6).

An initial guess of the electron density is then made to construct the Hartree and exchange-correlation potentials, forming the total potential $V_{total} = V_{ext} + V_{Hartree} + V_{xc}$. With the total potential established, the numerical solution of the Kohn–Sham equation proceeds. Solving this equation yields new wavefunctions, which are then used to construct an improved estimate of the electron density. This iterative process continues until the new density matches the old density within a predefined convergence threshold. Once convergence

is reached, the total energy of the system can be accurately calculated using the obtained ground state electron density.

Although DFT fails in describing specific properties, such as the underestimation of electronic band gaps, and inaccuracies in describing magnetic properties and biological molecules, it can be a reasonable starting point for ab-initio quantum mechanical calculations with the combinations of post-DFT corrections [248–250]. Furthermore, the principles of DFT form the basis for advanced methodologies like density functional perturbation theory (DFPT), which will be discussed in the following section.

Today, DFT is implemented in many software packages. For this PhD thesis, Quantum ESPRESSO suite is employed, which is an open-source software distributed under the GNU General Public License [151]. Its open-source nature ensures that it's widely used in the scientific community and is regularly updated with new features and continuous improvement by many users and developers.

2.1.2 Density functional perturbation theory for phonon

While DFT aims to describe the electronic structure of a system in its ground state, density functional perturbation theory (DFPT) extends this concept to the linear response of the system to small perturbations by slightly displacing atoms from their equilibrium positions [251]. Since phonon is a quantized mode of vibration by considering dynamic deformations in a crystalline solid, DFPT thus provides a powerful tool for predicting lattice dynamics, which is essential for studying thermal properties such as angular frequency, group velocity, and their interaction. DFPT is computationally efficient compared to other methods for calculating response properties because it avoids the need for numerous total energy calculations across different configurations. This efficiency is achieved by linearizing the Kohn-Sham equations around the ground state, which enables the calculation of energy derivatives with respect to perturbations.

Let us assume that I-th atoms R_I are displaced slightly from their equilibrium positions R_I^0:

$$R_I = R_I^0 + u_I \tag{2.7}$$

where u_I denotes small displacements around their equilibrium positions.

Such small perturbations result in a variation of the total energy E_{total}. Consequently, the total energy can be expressed through a Taylor expansion as follows:

$$E_{total}(u) = E_{total}^0 + \sum_{I\alpha} \frac{\partial E}{\partial R_{I\alpha}} u_{I\alpha} + \frac{1}{2} \sum_{I\alpha} \sum_{J\beta} \frac{\partial^2 E}{\partial R_{I\alpha} \partial R_{J\beta}} u_{I\alpha} u_{J\beta} + \cdots \tag{2.8}$$

where E_{total}^0 represents the energy at equilibrium without atomic displacements, and the sum is taken over all atomic indices I, J along Cartesian directions α, β.

Under the harmonic approximation, the third (and higher) derivatives of the energy with respect to atomic displacements are ignored. This approximation assumes that the potential energy surface can be replaced by a second-order Taylor expansion with a quadratic function.

Nevertheless, the third derivative of the energy is associated with anharmonic effects in lattice vibrations, which is crucial for accurately describing properties such as thermal conductivity. These properties can present deviations from purely harmonic behavior. The implication of anharmonic effects will be discussed in detail in the following Section 2.1.3.

In equation 2.8, the first-order derivative of the energy with respect to this perturbation equals zero at the equilibrium geometry of the system. This is because the forces acting on all parts of the system cancel out, resulting in a state of mechanical equilibrium where the system is in its lowest energy state. The second-order derivative of total energy with respect to displacements u_α and u_β is referred to as the interatomic force constant (IFC). This quantity reveals the curvature of the potential energy surface near the equilibrium position, which is related to vibrational frequencies. The IFCs are responsible for defining the dynamical matrix:

$$D_{I\alpha,J\beta} = (M_I M_J)^{-\frac{1}{2}} \frac{\partial^2 E}{\partial R_{I\alpha} \partial R_{J\beta}} \tag{2.9}$$

where D is the dynamical matrix, and $M_{I,J}$ are the atomic mass of atoms involved. This mass-weighted dynamical matrix formulation enables the force constants to transform into frequencies. Since the dynamical matrix is derived from IFCs in real space, a Fourier transform is employed to move from the real space to the reciprocal space representation in the crystal's Brillouin zone. The Fourier-transformed dynamical matrix $\widetilde{D}$ for a wave vector q is given by:

$$\widetilde{D}_{\alpha,\beta}(q) = \sum_{I,J} D_{I\alpha,J\beta} \cdot e^{[iq\cdot(R_I - R_J)]} \tag{2.10}$$

Once the dynamical matrix is computed, it can be diagonalized to calculate the angular frequencies and modes, revealing the system's vibrational properties:

$$\sum_{\beta} \widetilde{D}_{\alpha,\beta}(q)\, e_\beta^{qm} = \omega_{qm}^2 e_\alpha^{qm} \tag{2.11}$$

where e^{qm} is the eigenvector corresponding to the phonon mode m, and ω_{qm}^2 is the square of the angular frequency as the eigenvalue of the matrix. As the dynamical matrix is Hermitian, its eigenvalues are real. This allows for the computation of the actual angular frequencies ω of the normal vibrational modes within the crystal by taking the square roots of these eigenvalues. Through this sequence of methods, the angular frequencies corresponding to each wave vector q can be calculated, thereby enabling the construction of the phonon dispersion relations.

In a manner analogous to the SCF procedure described for DFT in the previous section, DFPT employs a similar iterative process to achieve self-consistency in the presence of a small perturbation. The SCF-like loop in DFPT is dedicated to compute the first-order derivative of the charge density and wavefunction for the perturbed system by using the Sternheimer equation, which reads

$$[H - \varepsilon_i]\frac{\partial \phi_i(r)}{\partial R_\alpha} = -[\frac{\partial V(r)}{\partial R_\alpha} - \frac{\partial \varepsilon_i(r)}{\partial R_\alpha}]\phi_i(r) \qquad (2.12)$$

where H is the unperturbed Kohn-Sham Hamiltonian based on the ground state charge density, ε_i are the eigenvalues corresponding to the unperturbed wavefunctions $\phi_i(r)$.

The Sternheimer equation enables the direct calculation of first-order wavefunction, reducing computational costs. Once the Sternheimer equation is solved for the change in the wavefunction due to the perturbation, the first-order charge density can be updated as follows:

$$\frac{\partial n(r)}{\partial R_\alpha} = 2\sum_i [\phi_i^*(r)\frac{\partial \phi_i(r)}{\partial R_\alpha}] \qquad (2.13)$$

With the new first derivative charge density, it is used to update potentials to solve the Sternheimer equation again. This continues until the linear response wavefunctions converge.

After obtaining a converged linear response, the Hellmann-Feynman theorem is applied to compute the forces acting on the atoms from the perturbed electron density [252]. According to the theorem, the force on an atom can be computed directly from the derivative of the

total energy with respect to the atomic position. These forces allow for an efficient calculation of the interatomic force constants, which are then used to construct the dynamical matrix, ultimately leading to phonon dispersion relations.

2.1.3 Phonon anharmonicity

Moving beyond the harmonic approximation, understanding of anharmonic effects is critical in determining thermal conductivity and heat capacity where forces are no longer purely linear with respect to atomic displacements [253,254]. Anharmonicity, which is mainly dominated by the three-phonon scattering process, is captured through third-order derivatives of the energy to perturbations. The third derivatives of the energy with respect to atomic displacements, absent in equation 2.8, are introduced as follows in the Taylor expansion:

$$E_{total}(u) = E^0_{total} + \sum_{I\alpha} \frac{\partial E}{\partial R_{I\alpha}} u_{I\alpha} + \frac{1}{2} \sum_{I\alpha} \sum_{J\beta} \frac{\partial^2 E}{\partial R_{I\alpha} \partial R_{J\beta}} u_{I\alpha} u_{J\beta} + \frac{1}{3!} \sum_{I\alpha} \sum_{J\beta} \sum_{K\gamma} \frac{\partial^3 E}{\partial R_{I\alpha} \partial R_{J\beta} \partial R_{K\gamma}} u_{I\alpha} u_{J\beta} u_{K\gamma} + \cdots \quad (2.14)$$

where I, J, K are atomic indices along Cartesian directions α, β, γ. Note that the contribution of fourth-order and higher terms to anharmonic properties is negligible compared to second and third-order terms at room temperature [255].

Based on the third-order derivative of the energy, the anharmonic scattering coefficients $V^{(3)}$ can be defined, characterized by wave vectors q_1, q_2, and q_3 in reciprocal space [150,202]:

$$V^{(3)}_{q_1 m, q_2 m', q_3 m''} = \frac{1}{N_0} \frac{\partial^3 E}{\partial X_{q_1 m} \partial X_{q_2 m'} \partial X_{q_3 m''}} \quad (2.15)$$

where index m is phonon mode of wave vector q and N_0 is the number of unit cells in the crystal, which is used to normalize the scattering coefficient. The adimensional term $X_{q_1 m}$ is expressed by

$$\frac{\partial}{\partial X_{q_1 m}} = \sum_{I\alpha} \sqrt{\frac{\hbar}{2 M_I \omega_{q_1 m}}} e^{q_1 m}_{\alpha} \frac{\partial}{R_{I\alpha}} \quad (2.16)$$

In principle, these anharmonic coefficients can be calculated by using the '2n + 1' theorem [256]. This theorem makes it possible to compute

the third derivative of the total energy by utilizing first-order derivatives of the ground-state density and wavefunctions, avoiding computationally demanding supercell calculations. From the coefficients obtained, the anharmonic broadening of phonon is determined, which is linked to the inverse of the lifetime due to phonon-phonon interaction through a Heisenberg relation [150]:

$$\frac{1}{\tau_{q_1 m}} = 2\Gamma_{q_1 m} = \frac{\pi}{\hbar^2 N_q} \sum_{q_2 m', m''} \left| V^{(3)}_{q_1 m, q_2 m', q_3 m''} \right|^2 \times \left[\left(1 + f_{BE,q_2 m'} + f_{BE,q_3 m''}\right) \delta\left(\omega_{q_1 m} - \omega_{q_2 m'} - \omega_{q_3 m''}\right) + 2\left(f_{BE,q_2 m'} - f_{BE,q_3 m''}\right) \delta\left(\omega_{q_1 m} + \omega_{q_2 m'} - \omega_{q_3 m''}\right) \right] \quad (2.17)$$

where $\tau_{q_1 m}$ is the phonon lifetime, corresponding to the half width at half maximum of phonon broadening with wave vector q_1 and mode m. N_q denotes the number of q points sampled within the first Brillouin zone (BZ) and f_{BE} is the Bose-Einstein distribution function to represent the phonon occupation numbers. The phonon lifetime τ depends on temperature through the Bose-Einstein distribution function. The energy must be conserved in the three phonon interactions by the Dirac function δ.

The three arbitrary wave vectors q_1, q_2, and q_3 have the relationship $q_3 = -q_1 - q_2$. When the resulting wave vector q_3 belongs to the first BZ, the interaction is classified as a normal scattering process. On the contrary, Umklapp processes occur when q_3 falls outside the first BZ, implying a momentum transfer to the lattice to bring q_3 back into the zone. A detailed exploration of normal and Umklapp scattering processes will be provided in Section 2.2.2.

The calculation of the anharmonic third-order dynamical matrix and phonon lifetimes is implemented in the 'd3q' and 'thermal2' codes developed by Paulatto within the Quantum ESPRESSO suite [150,151]. These computational tools utilize the '2n + 1' theorem to efficiently capture three-phonon interactions. The capability has been validated in the literature, demonstrating their precision [68,69,257].

Figure 2.2 shows the computational procedures involved in the 'd3q' and 'thermal2' codes for anharmonic phonon calculations within the

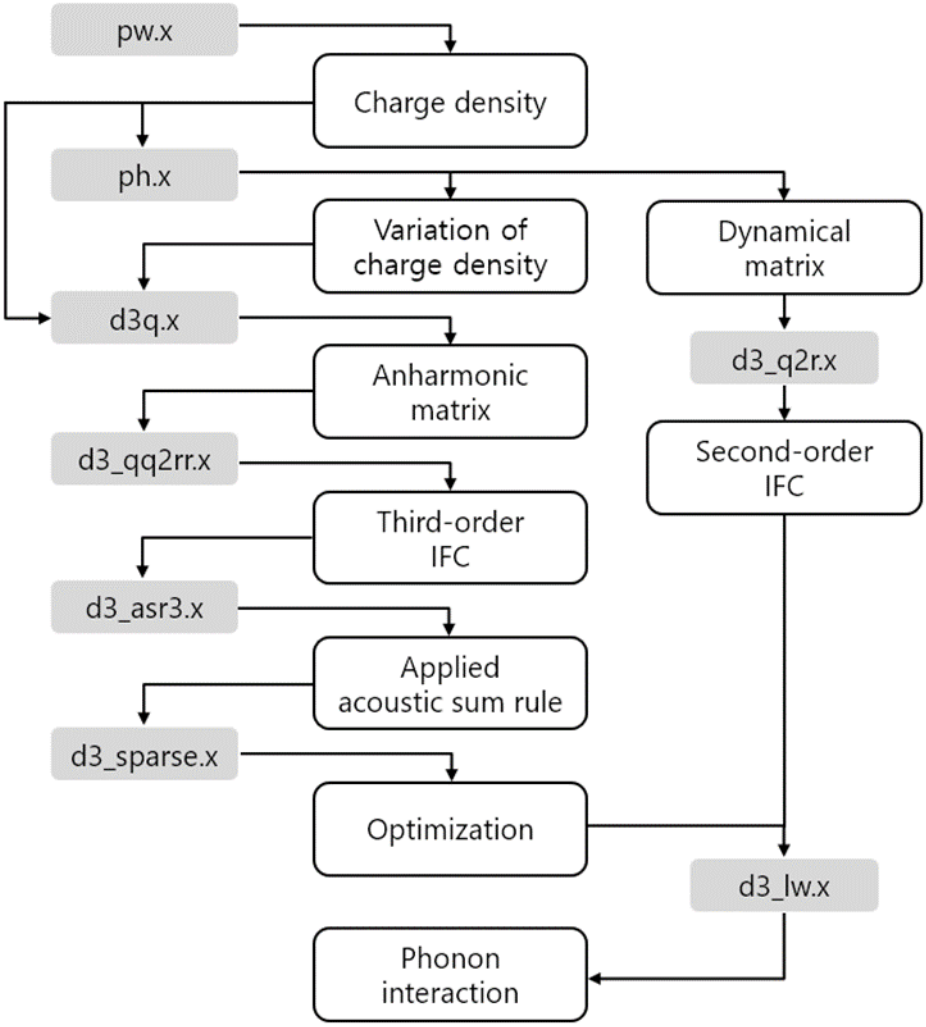

Figure 2.2 Flowchart of the algorithm from DFT to DFPT for anharmonic phonon calculations. Gray boxes indicate the execution codes implemented in the Quantum ESPRESSO suite.

Quantum ESPRESSO suite. Initially, 'pw.x' code undertakes the DFT calculations to obtain the ground state electronic structure and charge density. After that, 'ph.x' performs to compute the second-order dynamical matrices at each wave vector in the Brillouin zone. Next, 'd3_q2r.x' transforms these quantities from reciprocal to real space. The core process, 'd3q.x', derives the third-order energy derivatives relative to atomic displacements, forming the anharmonic matrix. The

'd3_qq2rr.x' mirrors 'd3_q2r.x' but for third-order matrices. The 'd3_asr3.x' then applies the acoustic sum rule to the three-body interatomic force constants to ensure translational invariance. Following this, 'd3_sparse.x' refines third-order IFCs into an optimized sparse format. Finally, d3_lw.x integrates all the preceding data to determine the phonon lifetime, relating to the intrinsic phonon-phonon interaction and the interaction of phonons with the isotopic disorder by natural isotopes.

2.2 MONTE CARLO SIMULATION

This section elucidates the stochastic particle Monte Carlo (MC) method to solve the Boltzmann transport equation (BTE) in phonon transport simulations. This method is a powerful and effective computational technique to describe complex systems in non-equilibrium states through statistical sampling. The required parameters, such as the phonon dispersion and scattering rates, are determined by ab-initio calculations, as discussed in the previous section, ensuring accurate numerical solutions in the MC simulation.

Section 2.2.1 explains the BTE for phonons under a temperature bias with the relaxation time approximation. Section 2.2.2 provides further details on different scattering mechanisms that affect the transport of phonons. In Section 2.2.3, we define our approach to temperature estimation in the context of these simulations. Section 2.2.4 is dedicated to describing our Monte Carlo algorithm to handle large numbers of particles in the investigated devices. Lastly, Section 2.2.5 discusses the post-processing steps to calculate thermal conductivity and interface thermal conductance, following the Monte Carlo simulations.

2.2.1 Boltzmann transport equation with the relaxation time approximation

The Boltzmann transport equation provides a fundamental framework for describing the statistical behavior of a thermodynamic system by considering a probability distribution for the position and momentum of a particle [197]. Since phonons are quasi-particles representing the quantized modes of vibrations of the lattice, the BTE can then be used to describe the distribution and transport of phonons. The phonon distribution function $f_s(r, q, t)$ represents the probability of finding a phonon as a quasi-particle at position r, with a wave vector q for a phonon in state s at time t. Its evolution is governed by the BTE:

$$\frac{\partial f_s}{\partial t} + \vec{v}_{g,s} \cdot \frac{\partial f_s}{\partial r} = \left(\frac{\partial f_s}{\partial t}\right)_{coll} \tag{2.18}$$

where $\vec{v}_{g,s}$ denotes the group velocity of phonon, which is the derivative of angular frequency ω with respect to q. Note that in equation 2.18, external forces are omitted. This is because such forces can be considered negligible in heat transport, given that phonons are unaffected by electric fields.

The right-hand side, $\left(\frac{\partial f_s}{\partial t}\right)_{coll}$, indicates the collision term to account for phonon scattering processes, including phonon-phonon interaction, and phonon-isotope interaction. The complexity of solving the Boltzmann transport equation originates with the complex collision term. To simplify this, the system is assumed to gradually return to its equilibrium state, represented by the equilibrium distribution function, over a relaxation time due to the phonon interactions. This approximation is known as the relaxation time approximation (RTA) [188], and is described as follows:

$$\left(\frac{\partial f_s}{\partial t}\right)_{coll} = -\frac{f_s - f_{BE,s}}{\tau_s} \tag{2.19}$$

where τ_s is the relaxation time of phonon state s. In thermal equilibrium, the distribution function for phonons is given by the Bose-Einstein distribution [258]:

$$f_{BE,s}(\omega_s, T) = \frac{1}{e^{\hbar\omega_s/k_B T} - 1} \tag{2.20}$$

where k_B is the Boltzmann constant, and T is the temperature of the local system. The Bose-Einstein distribution is used in dealing with phonons because phonons are bosons, which do not obey the Pauli exclusion principle.

When applying a temperature gradient in the system, the phonon distribution deviates from the Bose-Einstein equilibrium, creating a non-equilibrium state that leads to phonon transport. The Boltzmann transport equation in the framework of the relaxation time approximation becomes more amenable to numerical analysis for Monte Carlo simulations to model how phonons return to equilibrium after being disturbed by the temperature gradient. The following section will thoroughly explore the specifics of phonon interactions corresponding to the relaxation time and boundary conditions.

2.2.2 Scattering mechanisms

In the Monte Carlo simulations for thermal transport, the implementation of phonon scattering processes stands as an essential component. These processes directly influence phonon dynamics through interactions among phonons themselves, with impurities, and with the structural boundaries of the examined device, thereby impacting the thermal energy flow. This section aims to classify the various types of phonon interactions, providing a detailed definition. Furthermore, we explore how these interactions are integrated into Monte Carlo simulations.

2.2.2.1 Phonon-phonon and phonon-isotope scattering

Through the DFT calculations by considering phonon anharmonicity, the effects of intrinsic phonon-phonon scattering mechanisms can be precisely simulated. This ab-initio approach enables the accurate representation of how phonons interact through collisions, as explained in Section 2.1. Such interactions are primarily categorized into two processes: normal (N) and Umklapp (U) scattering, illustrated in Figure 2.3 (a) and (b), respectively.

In the case of N processes, the total energy and momentum of the phonons is conserved, and phonon wave vectors reside within the 1st Brillouin zone in the collision [69]. Therefore, N processes do not directly contribute to thermal resistance due to the momentum conservation, but they still affect heat transport by modifying the out-of-equilibrium phonon distribution.

Conversely, U processes only conserve the energy because the sum of phonon wave vectors falls outside the 1st Brillouin zone, resulting in a momentum flip [69]. This transformation violates the conservation of momentum, leading to thermal resistance. At elevated temperatures, Umklapp processes become a dominant mechanism of thermal resistance because phonons with higher energies are more abundant, making it more likely for conditions where the combined momentum exceeds the 1st BZ.

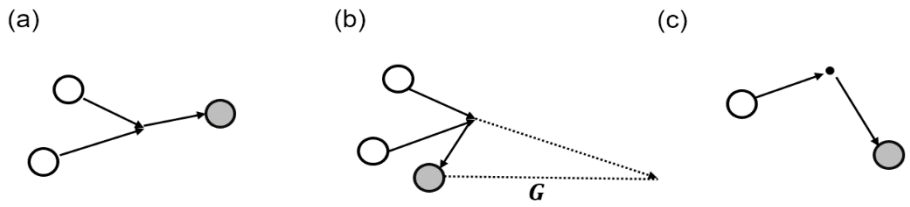

Figure 2.3 Illustration of phonon scattering mechanisms for (a) normal process, (b) Umklapp process, and (c) isotope process.

Furthermore, the presence of isotopes in a material introduces mass disorder, affecting the thermal transport characteristics [202]. If a material consists of atoms of the same element, but with different masses, the mass variation disrupts the uniformity of the lattice vibrations, as shown in Figure 2.3 (c). Consequently, this isotopic disorder contributes additional resistance to phonon flow, which is called phonon-isotope (Iso) scattering. This is particularly significant at lower temperatures, where other scattering mechanisms are less dominant.

Indeed, our analysis comprehensively evaluates these phonon scattering mechanisms over a broad temperature spectrum, ranging from the cryogenic 0.1 K to 1000 K. While our primary focus is on room temperature conditions, this extensive temperature range enables us to thoroughly investigate phonon behavior under extreme thermal scenarios, whether at exceedingly low or high temperatures. Moreover, this study not only examines the temperature dependence of phonon behavior, but also distinctly analyzes the contributions of normal, Umklapp, and isotopic scattering processes. The specific roles of these mechanisms will be delineated in the results chapters, highlighting the significant contributions of our research to understanding phonon interactions and thermal transport phenomena.

The integration of these scattering effects into relaxation time calculations for Monte Carlo simulations can be modeled with the Matthiessen's rule. According to this rule, the total relaxation time τ_s is the inverse of the total scattering rate, which aggregates the effects of normal (N), Umklapp (U), and isotopic (Iso) scattering processes.

Mathematically, this relationship is expressed as

$$\frac{1}{\tau_s} = \frac{1}{\tau_s^N} + \frac{1}{\tau_s^U} + \frac{1}{\tau_s^{Iso}} \tag{2.21}$$

where τ_s^N, τ_s^U, and τ_s^{Iso} are the calculated lifetimes for normal, Umklapp, and isotope processes, respectively.

While the phonon-phonon scattering is typically a three-phonon process, this is approximated as a two-phonon process in our MC algorithm for practical purposes, drawing on the approach proposed by Lacroix et al. [206]. Once a simulated phonon undergoes scattering, the phonon is considered to lose the memory of its initial state, necessitating the random selection of a new state from an equilibrium distribution. In this algorithm, the same energy is assigned to each pseudo particle, ensuring energy conservation. The selection probability of a new state m is proportional to the equilibrium density of states and the interaction rate for that state.

$$P_m \propto \frac{f_{BE,m}(\omega_m, T)}{\tau_m(\omega_m, T)} \tag{2.22}$$

This simplification assumes that the third phonon is part of the equilibrium background and does not change significantly during the interaction. Although this does not capture the full complexity of the three-phonon process, numerous studies have validated the two-phonon approximation as a consistent approach [188,240,241]. The detailed methodology is extensively discussed in previous literature [259].

2.2.2.2 Collision with the device boundary

In order to conduct device simulations for various nanostructures, selecting the appropriate boundary conditions is essential. This is because the interaction of phonons with device boundaries significantly influences its thermal properties, resulting in size-dependent thermal conductivity. Inaccurate boundary conditions can lead to significant errors in predicting device performance, especially

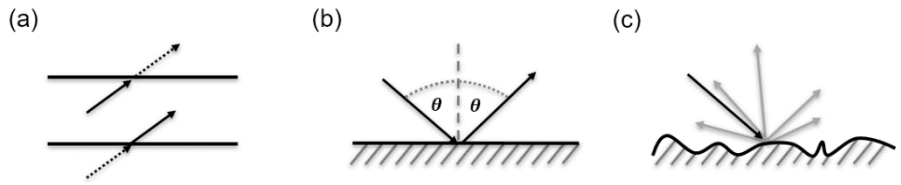

Figure 2.4 Schematic representation of (a) periodic, (b) specular, and (c) diffusive boundary conditions.

in nanoscale devices.

Figure 2.4 shows a schematic representation of (a) periodic, (b) specular, and (c) diffusive boundary conditions. For the periodic boundary condition, when a phonon reaches the external interface, it re-enters from the opposite side with the same state, preserving its wave vector and energy. This method simulates an infinitely repeating system, which is particularly suitable for studying the properties of bulk materials or wider nanofilms, where edge effects are negligible.

Specular boundary conditions assume that phonons are reflected from a smooth boundary in a mirror-like fashion, with the incidence angle equal to the reflection angle, as shown in Figure 2.4 (b). For a phonon with an incident wave vector component normal to the surface boundary ($q_{\perp}^{i}$), the reflected phonon has a wave vector component ($q_{\perp}^{r}$) that is equal in magnitude but opposite in direction, with the relationship $q_{\perp}^{i} = -q_{\perp}^{r}$. This type of boundary is appropriate for ideal device with exceptionally smooth surfaces.

Diffusive boundary conditions are adopted when phonons scatter randomly upon interacting with the surface boundary in various directions. This stands in contrast to specular reflection, where phonons reflect predictably. When phonons collide with a rough boundary, a combination of specular and diffusive scattering can occur. In this study, the probability of specular reflections $P_{specular}$ is determined following Soffer's model [215], which is expressed as:

$$P_{specular}(q^i, \vec{v}^i) = \exp[-(2\frac{v_\perp^i}{|\vec{v}^i|} \times \Delta \times |q^i|)^2] \quad (2.23)$$

where $\vec{v}^i$ is the velocity vector of incident phonon and $v_\perp^i$ is its component normal to the surface boundary. The term Δ represents the root mean square of the surface height deviation, which is called the surface roughness parameter.

In practice, when a phonon encounters a rough surface, diffusive reflection is likely to occur, which randomizes the direction of the phonon's velocity. The reflected state of the phonon is selected from among those energetically equivalent to the initial state as an iso-energy state, thereby conserving the phonon's energy. Mathematically, the component of the reflected velocity normal to the surface should be in the opposite direction to that of the incident normal component ($v_\perp^i \times v_\perp^r < 0$). The probability of reflected state in diffusive scattering can be captured by [188]

$$P_{diffusive}(q^r, \vec{v}^r) \propto [1 - P_{specular}(q^r, \vec{v}^r)] \times v_\perp^r \quad (2.24)$$

This equation signifies that if a phonon does not scatter specularly, it is likely to scatter diffusively. It also highlights that phonons with a higher normal velocity component have a higher chance of undergoing a diffusive scattering event. In the case where $P_{specular}$ equals zero, all phonons are scattered in random directions at rough boundaries, excluding any specular reflection, thus indicating a fully diffusive condition.

2.2.2.3 Collision with a semi-transparent interface

Phonon transmission across the interface between different materials is implemented using a full-band version of the diffuse mismatch model (DMM) in our MC simulation. The DMM characterizes a semi-transparent interface where phonons undergo diffusive scattering upon interaction, subsequently losing the memory of their initial state.

Originally proposed by Swartz and Pohl [235] and later extended to full-band dispersion by Reddy and colleagues [236], the DMM can be

expressed to represent the transmission probability $\alpha_{A\to B}$ of a phonon wave vector q with angular frequency ω_s colliding on the interface from A side as [232]:

$$\alpha_{A\to B}(\omega_s) = \frac{I_{B,,\vec{n}}(\omega_s)}{I_{A,\vec{n}}(\omega_s) + I_{B,\vec{n}}(\omega_s)} \tag{2.25}$$

where $\vec{n}$ is the normal vector to the interface, and $I_{A/B,\vec{n}}(\omega_s)$ are the DMM impedances, which act as material dependent parameters. These impedances are defined as

$$I_{A/B,\vec{n}}(\omega_s) = \frac{\Omega_{A/B}}{2\cdot(2\pi)^3}\sum_{s,A/B}\delta(\omega_{s_{A/B}} - \omega)\left|\overrightarrow{v_s}_{A/B}\cdot\vec{n}\right| \tag{2.26}$$

where $\Omega_{A/B}$ are the volumes of the reciprocal space corresponding to the Brillouin zone of material A and B, respectively, $\overrightarrow{v_s}$ is the phonon group velocity, and δ is the Kronecker delta function. The summation is conducted over all phonon states within the whole first Brillouin zone. In the DMM framework, it is postulated that a phonon loses memory of its initial state, conserving only its energy. Consequently, the transmission probability from material B to A is given by $1 - \alpha_{A\to B}(\omega_s)$.

When a phonon encounters the semi-transparent interface, it randomly undergoes either reflection within the same material or transmission to the adjacent material based on the transmission probability outlined in equations 2.25 and 2.26. Similar to the probabilities associated with rough boundary previously mentioned, a new state is randomly selected from among the iso-energy states in the final material, with the probability P_{DMM} following the rule [232]:

$$P_{DMM}(q^r, \vec{v}^r) \propto [1 - \alpha_{A\to B}(\omega_s)] \times v_\perp^r \tag{2.27}$$

Recent research has validated that MC simulation employing DMM successfully addresses the interface thermal conductance for polytype materials or other two-material systems [239–241].

2.2.3 Definition of temperatures

2.2.3.1 The concept of standard temperature

The temperature at each position within the simulated structure should be continuously updated to accurately determine the thermal properties, such as thermal conductivity and interface thermal conductance, since phonon scattering rates vary with temperature. The standard pseudo-temperature T is derived from the phonon energy density at each position within the simulated device according to the equilibrium Bose-Einstein statistics for each material. The energy density is described by the following simplified relationship [188]:

$$E(T) = \frac{\Omega}{(2\pi)^3} \sum_s \hbar \omega_s f_{BE,s}(\omega_s, T) \tag{2.28}$$

The standard pseudo-temperature T is thus obtained through the energy inversion of the energy-temperature relationship provided by equation 2.28.

However, the standard temperature definition, which assumes an equilibrium condition, might not be suitable for calculating the interface thermal conductance, especially when addressing heat transfer through an interface expected to experience strong out-of-equilibrium conditions [239]. Therefore, a more advanced approach is necessary to determine the precise temperature.

2.2.3.2 The directional temperatures

When considering a thermal gradient between a hot and cold thermostat, phonons propagate this thermal energy by moving within the simulated device. To comprehensively analyze the heat transport dynamics, phonons can be distinguished into two categories based on their direction of motion. [238]. "Forward" phonons are those with a positive velocity vector moving from a hot thermostat to a cold thermostat in the direction of the primary heat flux. Conversely, "backward" phonons are defined by having a negative velocity component from the cold side toward the hot side.

In this context, the directional temperatures, T^+ and T^-, are introduced corresponding to phonon sub-populations with positive and negative velocities, respectively, as detailed in [239]:

$$E^{\pm}(T^{\pm}) = \frac{\Omega}{(2\pi)^3} \sum_{s, v_s>0 \text{ or } v_s<0,} \hbar\omega_s f_{BE,s}(\omega_s, T^{\pm}) \qquad (2.29)$$

where $E^{\pm}$ are the phonon energy density according to the forward or backward phonons, respectively. If the system is in equilibrium, all three temperatures converge to the same value ($T = T^+ = T^-$). Opting for the directional temperatures T^+ and T^- over the standard pseudo-temperature T provides a more accurate representation of non-equilibrium conditions, for instance, thermal resistance at the interface or transient conditions.

2.2.4 Algorithm of Monte Carlo simulation

The Monte Carlo algorithm is used to solve the Boltzmann transport equation, which describes the time evolution of the phonon distribution function. Figure 2.5 shows a flowchart diagram of this algorithm [259]. This starts with loading a full-band material description of the material under investigation. In the past, our study would typically rely on semi-empirical models like the adiabatic bond charge model (ABCM) or adopt the DFT data conducted externally. However, this study employs a direct calculation approach using the Quantum ESPRESSO suite, grounded in DFT principles (see Section 2.1). This method meticulously accounts for phonon anharmonicity, clearly distinguishing between normal and Umklapp scattering mechanisms, and further incorporates the influence of isotopic variation.

To improve accuracy and optimize computational resources, we have integrated the "energy-based variance-reduced method" introduced by Peraud [213]. In energy-based formulation, phonon packets with the same amount of energy are simulated instead of individual phonons. The number of individual phonons in a packet is tuned to maintain the same total energy regardless of their angular frequency. The variance-reduced formulation is based on the concept that only excess particles of the deviation from Bose-Einstein equilibrium statistics are stochastically evaluated. Therefore, the density of simulated particles at equilibrium can be defined as

$$n_s^{eq}(T) = \frac{\Omega}{(2\pi)^3}\left[f_{BE,s}(\omega_s, T) - f_{BE,s}(\omega_s, T^0)\right]\frac{\hbar\omega_s}{E_p} \tag{2.30}$$

where T^0 is the reference temperature, and E_p is the energy resolution parameter to guarantee the same total energy.

The reference temperature enables the focus of computational resources on the "excess" phonon packets that are out-of-equilibrium and contribute to the actual heat transfer in the system. The initial phonon distributions are generated by summing over all phonon states s, based on equation 2.30. Both techniques enhance simulation speeds and yield more precise results while utilizing fewer computational efforts.

Figure 2.5 Flowchart of the Monte Carlo algorithm for phonon transport simulation, adapted from [259].

After the initialization step, which involves loading material data and establishing a random and uniform initial distribution of particles in both real and reciprocal space, the simulation updates the temperature in each position at every time step, as detailed in Section 2.2.3. Particles are then injected from external thermostats into the system, assuming phonon transport from the thermostat to be ballistic. These thermostats act by injecting phonons into the system at a high temperature (hot thermostat) and absorbing phonons at another contact at a lower temperature (cold thermostat), thereby creating a

temperature bias. To replicate the continuous injection of particles from the thermostats, every particle is initialized at the beginning of each time step.

During a time step, the movement of these simulated phonons can be interrupted by temperature-dependent phonon scattering mechanisms or collisions with external boundaries, as outlined in Section 2.2.2. The time until its next phonon scattering event $t_{scattering}$ is randomly determined to reflect the inherent unpredictability of these interactions:

$$t_{scattering} = -\ln(n_{random}) \times \tau_s(T) \tag{2.31}$$

where n_{random} is a randomly generated number between 0 and 1. This random number ensures that the scattering events occur stochastically, mimicking the randomness of such events in materials. $\tau_s(T)$ represents the overall relaxation time for a phonon in state s at the defined temperature, as the inverse of phonon scattering rates. This approach allows the simulation to account for the natural variability in the time between scattering events, with the likelihood of a scattering event increasing over time as the phonon travels without interacting.

When a phonon encounters external boundaries, the time to reach a boundary is derived from the distance d between the phonon and the boundaries in the direction of its transport:

$$t_{boundary} = \min\left(\frac{d^x}{v_s^x}, \frac{d^y}{v_s^y}, \frac{d^z}{v_s^z}\right) \tag{2.32}$$

where $d^{x,y,z}$ are the distances from the phonon to the boundaries in the x, y, and z directions, respectively, while $v_s^{x,y,z}$ are the components of the phonon's velocity in these same directions. If the phonon travels at a constant velocity during its free flight, the time until it hits a boundary is calculated as the minimum of the distances d to the boundaries, divided by the phonon's velocity components in each dimension.

In addition to the previously mentioned times, the phonon's free flight should be properly accounted for over the duration of a time step, even if it does not collide with anything or scatter during that time step.

The remaining time is calculated by taking the time step t_j, adding the duration of the time step δt, and then subtracting the current simulated time $t_{current}$ as follows:

$$t_{remaining} = \left(t_j + \delta t\right) - t_{current} \tag{2.33}$$

This tracking is essential for precisely depicting the phonon's motion, maintaining the integrity of its trajectory throughout the simulation, regardless of whether it experiences collisions or scattering.

Finally, the actual free flight of the particle is determined by whichever of these events happens first:

$$t_{free\_flight} = \min(t_{scattering}, t_{boundary}, t_{remaining}) \tag{2.34}$$

By taking the shortest of these times, the simulation can provide a realistic representation of the phonon's behavior before the end of the time step. Based on the calculated free flight time, the phonon's movement in real space is updated at each time step, and this process continues until the final time step is reached.

The in-depth implementation of our Monte Carlo algorithm is presented in the literature [188,206]. Upon completing the simulation, we conduct post-processing calculations to derive the final results, which will be discussed in the following section.

2.2.5 Thermal conductivity and interface thermal conductance

Thermal conductivity measures a material or system's ability to conduct heat, quantifying the rate at which thermal energy is transferred through the material due to a temperature gradient with a unit of watts per meter-kelvin (W/mK). In Monte Carlo simulations for phonon transport, the local thermal heat flux density is calculated by summing over the contribution of all particles and saved it at each time step.

The thermal conductivity of the simulated device is then determined from the average heat flux density $\vec{q}$ under steady-state conditions along the transport direction $\vec{n}$, utilizing Fourier's law of heat conduction [260]:

$$\kappa_{simulation} = \frac{\vec{q} \cdot \vec{n}}{\Delta T_{contact}} L \tag{2.35}$$

where $\Delta T_{contact}$ is the temperature difference between the hot thermostat T_H and the the cold thermostat T_C, and L is the device length between two thermostats. This approach makes it relatively insensitive to internal temperature variations. Note that the thermal conductivity, as determined by our Monte Carlo simulations, is presented with a 95% confidence interval, by taking into account the variability inherent to the numerical simulation process.

Interface thermal conductance (ITC) measures the ability to transfer heat across the interface between two different materials and is expressed in units of watts per meter squared per kelvin (W/m^{2}K) [235]. It is important for thermal management because it determines the efficiency of heat transfer from one material to another. The interface thermal conductance between two materials is computed as

$$G^I_{simulation} = \frac{\vec{q} \cdot \vec{n}}{\Delta T^I} \tag{2.36}$$

where ΔT^I is the difference in the temperatures on each side of the interface.

The calculation of ITC involves a nuanced definition of ΔT^I. While in

equilibrium states ΔT^I could be considered equivalent to $\Delta T_{contact}$, the situation is less straightforward when strong out-of-equilibrium conditions near the interface, defined by the diffusive mismatch model, are considered.

As discussed in Section 2.2.3, we incorporate the concept of directional temperatures into the ITC calculation to address these complexities. In the results chapter, we will explore how ITC varies with different temperature definitions and validate these findings by comparing them with the analytical solution introduced in Section 2.3.

2.3 ANALYTICAL MODELS FOR COMPARISON WITH NUMERICAL RESULTS

In this section, several well-established analytical models are introduced for thermal properties, which will serve as a benchmark for comparison with our Monte Carlo simulation results.

In systems where the dimensions smaller than the carrier mean free path, transport regimes become ballistic ones, based on the Landauer's formalism [261]. Within this ballistic regime, the analytical thermal conductivity is primarily determined by both the length of the simulated device and the phonon dispersion, especially for small temperature differences [162,239]:

$$\kappa_{ballistic} = \frac{\Omega}{(2\pi)^3}\frac{L}{2}\sum_{s}\hbar\omega_s|\overrightarrow{v_s}\cdot\vec{n}|\frac{\partial f_{BE,s}}{\partial T}(\omega_s,T) \tag{2.37}$$

It should be noted that equation 2.37 is independent of phonon scattering processes, assuming a phonon transmission coefficient of 1.

The thermal conductivity in the diffusive regime, often referred to as the bulk thermal conductivity, is simply described by a solution to the linearized BTE under the relaxation time approximation [218]:

$$\kappa_{diffusive} = \frac{\Omega}{(2\pi)^3}\sum_{s}\hbar\omega_s|\overrightarrow{v_s}\cdot\vec{n}|^2\frac{1}{\lambda_s}\frac{\partial f_{BE,s}}{\partial T}(\omega_s,T) \tag{2.38}$$

where λ_s is the total scattering rate, which is the inverse of the relaxation time of phonon state s.

While the aforementioned analytical models provide reliable insights into thermal transport in their respective regimes, one must account for the transition between these limits to estimate the thermal conductivity in devices with diverse lengths. A straightforward approach for addressing the intermediate transport regime is based on Matthiessen's rule, which sums the ballistic and diffusive thermal resistances (the inverse of thermal conductivity) to represent the overall thermal conductivity as follows [188]:

$$\frac{1}{\kappa_{Matthiessen}} = \frac{1}{\kappa_{ballistic}} + \frac{1}{\kappa_{diffusive}} \tag{2.39}$$

Although this approach offers an approximate value for the transition regime, it has shown considerable discrepancies when compared with numerical MC results for silicon nanofilms with a device length of several hundred nanometers [188]. For a more rigorous description of the thermal conductivity model, the phonon scattering rates should be redefined by considering their spectral dependencies [239]:

$$\lambda_{s,eff} = \lambda_s + 2\frac{|\overrightarrow{v_s} \cdot \vec{n}|}{L} \tag{2.40}$$

where $\lambda_{s,eff}$ is the effective scattering rate for a state s depending on device geometry, specifically for nanofilms where the width is not a determining factor. By substituting the scattering rate from equation 2.40 into equation 2.38, the resulting expression for effective thermal conductivity is [239]

$$\kappa_{effective} = \frac{\Omega}{(2\pi)^3}\sum_s \hbar\omega_s|\overrightarrow{v_s} \cdot \vec{n}|^2 \frac{1}{\lambda_{s,eff}}\frac{\partial f_{BE,s}}{\partial T}(\omega_s, T) \tag{2.41}$$

Next, the analytical model for interface thermal conductance in a lateral heterostructure is expressed as a function of the ballistic and the effective thermal conductivities of each constituent material [239]

$$G^I = \left[\frac{L^L}{\kappa^L_{ballistic}} - \frac{L^L}{\kappa^L_{effective}} + \frac{\Delta T_{contanct}}{q} - \frac{L^R}{\kappa^R_{effective}} + \frac{L^R}{\kappa^R_{ballistic}}\right]^{-1} \tag{2.42}$$

where L^L are L^R are the lengths of the left and right parts of the heterostructure, respectively, relative to a central interface, and the values of $\kappa^{L/R}_{ballistic}$ and $\kappa^{L/R}_{effective}$ corresponding to the lengths L^L are L^R are derived from equation 2.37 and equation 2.41, respectively.

This equation provides an analytical representation of the interface thermal conductance across all transport regimes, considering both material-specific and geometry-dependent thermal properties on either side of the interface. Further details regarding the inner derivation process can be found in our previous works [239].

2.4 SUMMARY

This chapter is pivotal for understanding phonon behavior in nanostructures, from the fundamental quantum mechanical calculations to the statistical simulations that predict phonon transport properties. In the framework of DFT, the Kohn–Sham equation is solved using ground-state electron density to determine the electronic structure's energy. Through DFPT, it examines the system's linear response to small perturbations, such as atom displacements from equilibrium, enabling analysis of lattice dynamics. This approach underlines the complexity of phonon interactions, particularly highlighting the significant influence of anharmonicity on thermal transport. All these calculations are conducted using the Quantum ESPRESSO suite.

Subsequently, the stochastic particle Monte Carlo (MC) method for solving the Boltzmann transport equation (BTE) in phonon transport simulations was introduced. Employing the relaxation time approximation makes it possible to simulate phonon transport by taking into account phonon interactions, impurities, and structural boundaries within various nanostructures. We outlined the Monte Carlo simulation algorithm step-by-step, demonstrating how to calculate thermal properties such as thermal conductivity and interface thermal conductance. It is also discussed analytical models that bridge theoretical understanding with computational simulation in the study of phonon transport in nanostructures.

This theoretical and simulation foundation will be applied in subsequent chapters to detailed investigations of phonon behavior in GaAs and 2D material-based nanostructures.

3 Full band Monte Carlo simulation of GaAs nanostructures for phonon transport based on ab-initio methods

Chapter 3 presents a study on the thermal properties of Gallium Arsenide (GaAs) nanostructures, using Monte Carlo (MC) simulation based on ab-initio calculations for phonon transport. The main goal of this chapter is to elucidate the complex interactions between phonon transport mechanisms and various conditions, such as device dimensions, boundary conditions, and temperatures.

In Section 3.1, the intrinsic properties of GaAs material are calculated by ab-initio methods derived from the density functional theory (DFT), and the thermal conductivity of bulk GaAs is compared with experimental data, proving the accuracy and the predictability of such simulations. Next, we design GaAs nanostructures by setting boundary conditions (3.2.1) and investigate cross-plane nanofilms, in-plane nanofilms, and nanowires, showing the impact of boundary conditions on the thermal conductivity as a function of both device dimension and temperature (3.2.2). Section 3.2.3 offers insights into the transition from ballistic to diffusive transport regimes. This study explores the modal contributions of individual phonon modes to thermal transport, emphasizing the prominent role of optical phonons in nanostructures (3.2.4). Lastly, a novel investigation into the effect of nanopores on the thermal conductivity of GaAs nanowires is discussed, shedding light on the potential presence of nanopores in experimentally synthesized nanowires (3.2.5).

3.1 BULK GAAS

3.1.1 Full-band description of Bulk GaAs

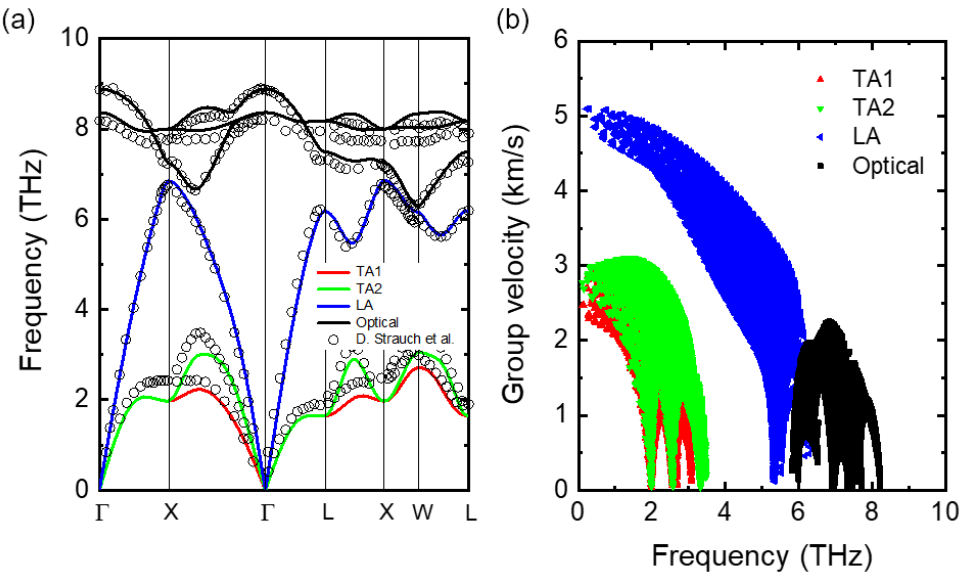

Figure 3.1 (a) Calculated phonon dispersion for GaAs along the high symmetry paths compared with experimental data from Ref. [49]. *(b) Phonon group velocity of TA, LA and optical phonon modes as a function of frequency computed using DFPT.*

The accuracy of thermal transport simulations highly depends on the quality of material properties used as input parameters. Therefore, this study employs a DFPT-based approach to calculate phonon dispersions, phonon group velocities, and scattering rates including isotopic effect throughout the first Brillouin zone (BZ) for GaAs.

To prevent possible inaccuracies arising from excluding some modes, such as optical phonons, this work considers a full-band description that encompasses all phonon modes within the Brillouin zone. Ab-initio parameters are computed using the Quantum ESPRESSO suite [151] with local density approximation and norm-conserving pseudopotentials.

In electronic structure calculations, the first BZ are sampled with a

Monkhorst-Pack [262] mesh of 8 x 8 x 8 in the k-space, and a plane-wave cut-off energy of 90 Ry. A convergence threshold for self-consistency is set at 10^{-8} which specifies the maximum allowed difference between the input and output electron densities in successive iterations. The optimized lattice parameter is a = 5.605 Å which is relaxed to equilibrium, closely matching experimental values [263].

After the electronic calculations are completed, the harmonic second-order and anharmonic third-order force constants are computed by using the density functional perturbation theory (DFPT) on meshes of 4 x 4 x 4 and 2 x 2 x 2 q-points, respectively, with convergence thresholds of 10^{-15} for the harmonic and 10^{-12} for the anharmonic calculations. In the final step, the 'thermal2' code within Quantum ESPRESSO is utilized to determine all phonon properties over a 32 x 32 x 32 mesh with a 2 cm^{-1} Gaussian broadening, which is close to convergence [68,150].

The phonon dispersion is determined by diagonalizing the 2nd order dynamical matrix. The calculated phonon dispersion for GaAs is shown in Figure 3.1 (a), which is in good agreement with experimental results [49]. GaAs has 6 phonon modes derived from the basis of two atoms in its primitive cell. These modes consist of three acoustic modes, i.e., one longitudinal acoustic (LA), two transverse acoustic (TA1 and TA2) modes, and three optical modes. Since the optical modes involve the vibrations of atoms against each other, they have higher frequencies than the acoustic ones.

The phonon group velocity is derived by taking the gradient of the phonon dispersion with respect to each q-point as shown in Figure 3.1 (b). Among acoustic modes, the LA mode has the highest group velocity in the low frequency range because it moves along the same direction of the wave propagation. The group velocities of two TA modes, while lower than that of the LA mode, remain substantial. Conversely, the optical modes exhibit relatively lower group velocities as evidenced by the flatter nature of the optical dispersion curves.

The phonon lifetimes, i.e., the inverse of the phonon scattering rates, are obtained from the 3rd order dynamical matrix considering the

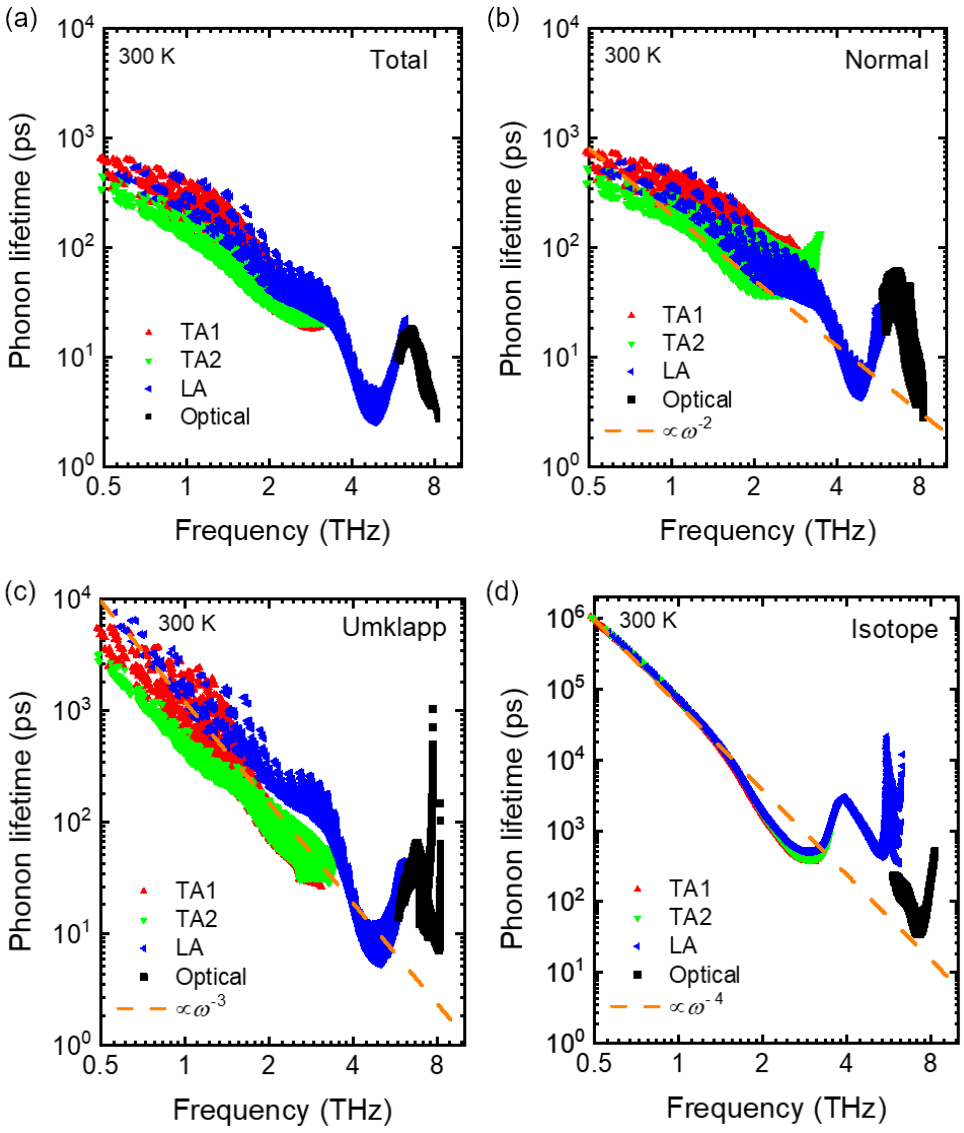

Figure 3.2 Phonon lifetime as a function of frequency at 300 K for different modes computed via DFPT. (a) Total lifetimes from combined all scattering mechanisms. Lifetimes due to (b) normal scattering, (c) Umklapp scattering, and (d) Isotope scattering lifetimes, with yellow dashed lines indicating power-law fits of ω^{-2}, ω^{-3}, and ω^{-4} , respectively.

phonon-phonon interaction due to anharmonicity as detailed in Chapter 2. These scattering processes can be categorized into normal and Umklapp events. The normal processes involve phonon-phonon

interactions where the total momentum is conserved, while the Umklapp processes involve phonon interactions that lead to a net change in momentum beyond the first BZ. Moreover, an isotopic disorder is also taken into consideration. While arsenic is a monoisotopic element, the natural gallium possesses two isotope mixtures, ^{69}Ga (60.11 %) and ^{71}Ga (39.89 %) [264]. The different masses of these isotopes can lead to variations in the phonon properties, referred to as phonon-isotope scattering. All scattering mechanisms are calculated within the temperature range from 0.1 to 1000 K, enabling a detailed examination of phonon transport in diverse thermal environments.

Figure 3.2 (a) presents the calculated total phonon lifetimes τ for each phonon mode over the entire frequency range at 300 K. The results reveal that the phonon lifetimes span several orders of magnitude, ranging from picoseconds to nanoseconds or even longer. At lower frequencies near the Γ point, acoustic modes with quadratic dispersions exhibit long lifetimes. As the frequency increases, the lifetimes of these acoustic modes approach those of the optical modes. Due to the extended lifetimes of acoustic modes, they exert a more pronounced influence on thermal transport than optical modes.

Using the Matthiessen rule, the total lifetimes can be decomposed as $1/\tau=1/\tau^{N}+1/\tau^{U}+1/\tau^{Iso}$ showing the contributions of normal, Umklapp, and isotope scattering mechanisms, respectively, as illustrated in Figure 3.2 (b) to (d). Those lifetimes also decrease with increasing frequency, showing a similar tendency to the total lifetime, but the detailed trends are slightly different. The yellow dashed lines represent a fitting to an inverse power law of the frequency to offer a quantitative depiction of the phonon lifetime's frequency dependence. In the low-frequency region, the lifetimes related to the normal scattering exhibit a ω^{-2} scaling, while those of the Umklapp scattering follow a ω^{-3} trend. These distinct frequency dependencies emphasize the unique characteristics inherent to each type of phonon interaction. Such observations are consistent with findings from other studies [55,265,266].

We also reveal that in GaAs the isotope effect is relatively small compared to other scattering mechanisms, but it still affects the

phonon properties with ω^{-4} dependence. Hence, we can conclude that the optical phonon modes are more sensitive to mass disorder, leading to increased phonon-isotope scattering.

Such power-law fittings provide an analytical means to predict an overall trend, but we can see that it is crucial to calculate on a first-principle basis for accurate material modeling. Thus, these ab-initio calculations enable to include the predictive power of quantum mechanics in the full-band Monte Carlo simulation to simulate the phonon transport instead of using empirical parameters such as Grüneisen parameters.

3.1.2 Comparison with experimental data for bulk GaAs thermal conductivity

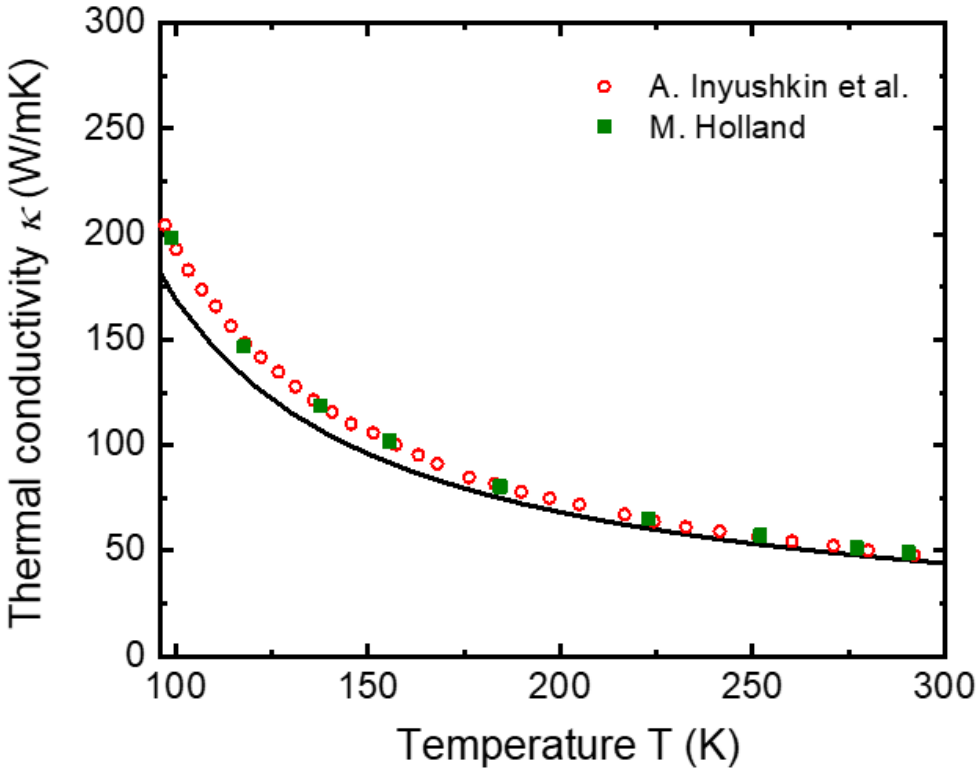

Figure 3.3 Comparison of (solid lines) calculated and (symbols) measured thermal conductivities of Bulk GaAs as a function of temperature. The calculated values are derived from DFT-based material properties. Experimental data from A. Inyushkin et al. (red circles) [39] *and M. Holland (green squares)* [34].

Combining the calculated phonon dispersion, group velocity and scattering rates obtained from ab-initio methods, the thermal conductivity of bulk GaAs is calculated using equation 2.38. Figure 3.3 shows the calculated thermal conductivity compared with experimental measurements [34,39] over a temperature range of 90 K to 300 K. The DFT-based predictions follow the temperature-dependent thermal conductivity observed in experimental results. Phonon scattering becomes less probable at lower temperatures,

leading to an increase in thermal conductivity.

At 300 K, the discrepancy between the calculated value of 45.6 W/mK and the experimental results is approximately 4.6 %. This discrepancy could be attributed to variations in the computed phonon dispersion, particularly in the TA modes, which show some deviations from the experimental data. Nevertheless, it is a reasonable estimation of the thermal conductivity for Bulk GaAs within 5 % of the experimental values at room temperature without using any empirical parameters.

3.2 GaAs NANOSTRUCTURES

3.2.1 Investigated structures depending on boundary condition

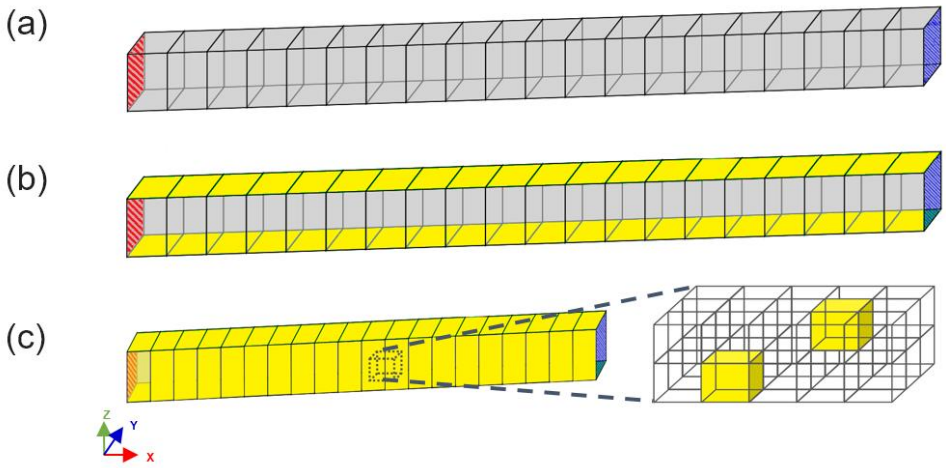

Figure 3.4 (a) Nanofilm in cross-plane configuration (CPNF), (b) Nanofilm in in-plane configuration (IPNF), (c) Nanowire (NW) and partial diffusive internal structure for mimicking nanopores. Red/blue faces for hot/cold thermostats T_H=302 K, T_C=298 K, respectively. Yellow faces for diffusive boundaries.

In this Section, we investigate three different types of nanostructure depending on how the boundary conditions are set, as illustrated in Figure 3.4. Two thermostats are applied at opposite edges of the nanostructures, separated by a distance *L*. Given their arrangement along the *x*-axis, with the hot thermostat (T_H=302 K) on the left and the cold one (T_C=298 K) on the right, the thermal flux is naturally oriented to flow in the positive *x*-direction. A finite rectangular computational mesh, consisting of cells, is employed within our Monte Carlo simulation framework along the *x*-axis for the numerical evaluation of the thermal properties of the devices. Within these nanostructures, the internal faces of the cells excluding the external boundaries are designed to be transparent, thus ensuring continuous phonon transport between adjacent cells [188].

The selection of external boundary conditions is important as it governs the confinement and transport of carriers within the nanostructures, hence affecting their thermal behavior. Figure 3.4 (a) shows a nanofilm with a cross-plane configuration (CPNF) where the thermal flux is perpendicular to the interfaces. All external boundaries are assumed to extend infinitely in the *y*- and *z*-direction by applying periodic boundary conditions. Accordingly, the effects of narrow widths such as zigzag or armchair edges are not considered in this study.

Figure 3.4 (b) presents a nanofilm with an in-plane configuration (IPNF), where the thermal flux flows parallel to the interfaces. This setup is modeled by applying periodic (*x*-*z* planes) and diffusive (*x*-*y* planes) boundaries that randomize the propagation direction of reflected phonons. Each boundary condition's specific definition and implementation are detailed and explained in Chapter 2.

In Figure 3.4 (c), it is illustrated a rough nanowire (NW) having only diffusive external boundaries designed with the same width along the *y*-direction and height along the *z*-direction. Compared to nanofilm configurations that employ a simple cubic mesh along the *x*-direction, our approach extends the mesh into a three-dimensional version comprising hundreds of cells distributed across the *x*, *y*, and *z* directions. Several cells are randomly chosen to represent nanopores based on the given porosity. The boundaries of each nanopore are assumed to be fully diffusive, simulating nanopores with zero transmittance. This enhanced mesh framework allows us to investigate the thermal properties of more complex structures, such as nanowires containing internal nanopores (Porous NW), that will be explained later in Section 3.2.5.

3.2.2 Thermal conductivity of GaAs nanostructures

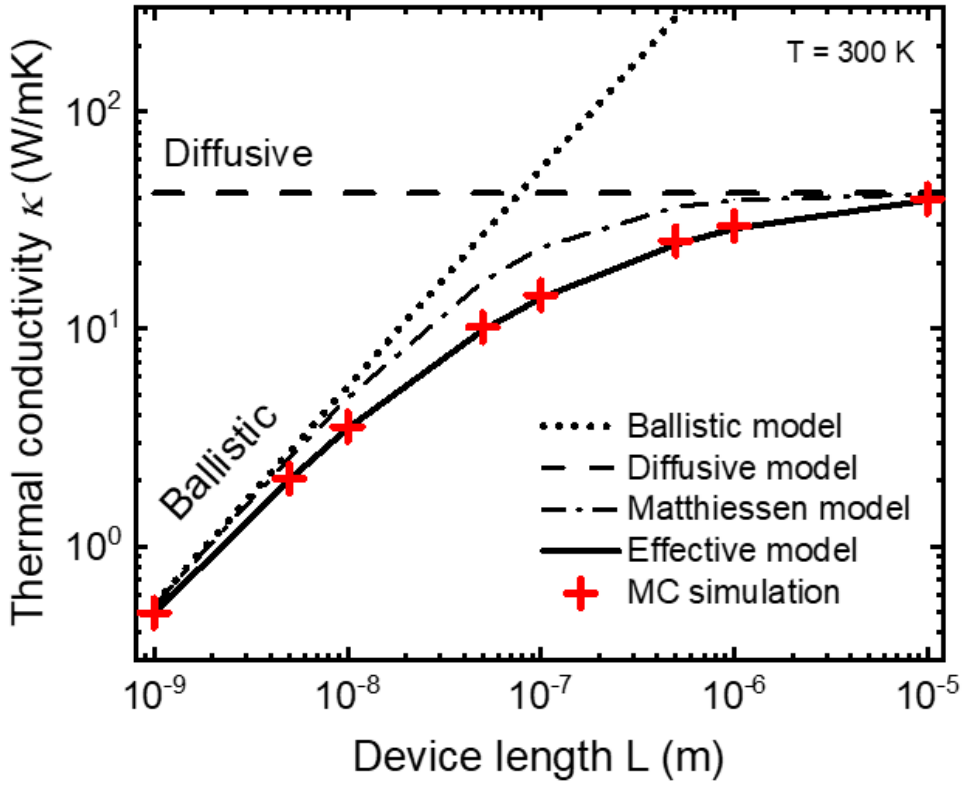

Figure 3.5 Thermal conductivity as a function of length for GaAs CPNF.

We first examine the length-dependent thermal conductivity of GaAs cross-plane nanofilms (CPNF) at room temperature, as shown in Figure 3.5. The Monte Carlo simulation results (red crosses) are compared with several analytical models detailed extensively in Chapter 2. As confirmed in the previous section, the diffusive value of thermal conductivity (dashed line) is 45.6 W/mK, which corresponds to the experimental values within a 5 % difference.

In ultra-short films (L<10 nm), which are on the order of magnitude of the phonon mean free path at the atomic scale, the thermal conductivity calculated by MC simulations converges to the ballistic model (dotted line), derived from Landauer's formalism, which is linearly dependent on the device length L. This concordance between numerical simulations and Landauer's ballistic model at these scales

confirms the validity of the MC approach in capturing the ballistic transport regime. As the length of the nanofilms increases, the calculated thermal conductivities move towards the diffusive value displaying an asymptotic behavior.

The Matthiessen model (point-dashed line) is often used in the literature because it simply adds the ballistic and diffusive thermal resistances (the inverse of thermal conductivity) [267,268], but fails to accurately characterize the intermediate regime, also referred to as the quasi-ballistic regime. When considering a CPNF within the intermediate regime with a length of 100 nm, the Matthiessen model predicts a thermal conductivity that is approximately 40 % higher than that determined by the Monte Carlo simulation. On the other hand, the effective model (solid line), already validated for silicon nanofilms [188], provides impressively accurate results.

It should be noted that even though the effective model reproduce the MC results with very good accuracy, it has limitations in more complex structures (cf. the following). Consequently, our MC results show good agreement across all phonon transport regimes, i.e. ballistic, quasi-ballistic, and diffusive, without using any fitting parameters, offering a robust tool for capturing the complexities of thermal behavior.

Beyond the investigation of only CPNF in Figure 3.5, which employed only periodic boundary conditions, Figure 3.6 presents the results for in-plane nanofilms (IPNF) and nanowires (NW) that incorporate rough boundary conditions. Here, 'rough' means a fully diffusive condition wherein all phonons are scattered in random directions at external boundaries, excluding any specular reflection. By comparing IPNF and NW structures to CPNF, the impact of rough boundaries on thermal transport can be examined.

Figure 3.6 (a) shows the evolution of thermal conductivity for CPNF, IPNF and NW with the device length L at 300 K. The width is fixed at 100 nm and a simple cubic mesh is utilized to maintain consistency within the simulation for all structures. The results of our MC simulations are represented by crosses in Figure 3.6 (a): red for CPNF, blue for IPNF, and green for NW. Correspondingly, solid lines of the

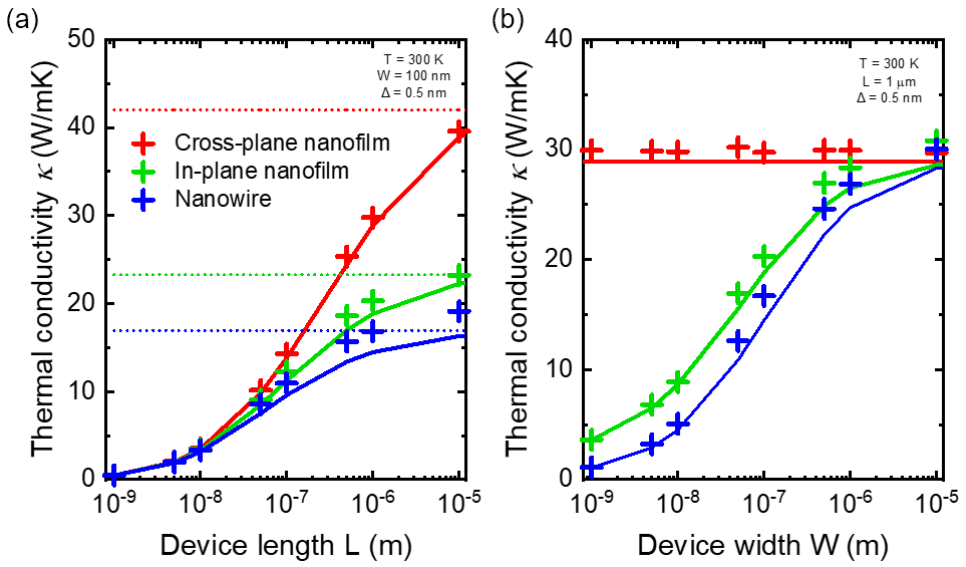

Figure 3.6 Thermal conductivity κ as a function of (a) the length L for a width W = 100 nm and (b) the width W for L=1 μm for CP and IP nanofilms and also for nanowires at 300 K. Solid and dotted lines represent for effective model and long-device thermal conductivity, respectively.

same colors denote the effective model, and dotted lines stand for the calculated long-device thermal conductivity within this model. The dotted lines serve as a benchmark, providing a visual gauge of the length-dependent thermal transport properties across the different structures.

In devices shorter than 10 nm, in which ballistic transport is expected, our findings indicate that the thermal transport properties are almost identical regardless of device type. This means that the effect of diffusive boundaries on thermal transport is negligible in devices with lengths, which is the order of magnitude of phonon mean free path. However, rough boundaries play a significant role in reducing thermal conductivity in longer devices for IPNF and NW. Specifically, IPNF and NW exhibit decreases in thermal conductivity of approximately 41 % and 52 %, respectively, when compared to CPNF for a length of 10 μm. This reduction is due to the increased phonon scattering at the rough

external interfaces when the heat transport is diffusive in longer devices.

Additionally, in cases of IPNF and NW exceeding 100 nm in length, a divergence emerges between the numerical MC results and the calculations of the effective model, unlike the close alignment observed in CPNF. This divergence highlights the limitations of the analytical model with the need for more sophisticated modeling approaches in such nanostructures.

In Figure 3.6 (b), the thermal conductivity of the same three different devices is investigated as a function of device width *W* with a uniform length of 1 μm. As expected, the CPNF is independent of width in thermal conductivity, because it is modeled as having infinite width without rough boundaries through the application of periodic boundary conditions.

In contrast, the IPNF and NW have a marked sensitivity to variations in width, with this effect being most notable at narrow widths due to the presence of rough boundaries. Differences in thermal conductivity are evident in thin devices with a width of 1 nm, attributable to the transition into a diffusive transport regime at a device length of 1 μm. In this regime, the effect of rough boundaries becomes increasingly pronounced. The degree of reduction in thermal conductivity relative to CPNF is significantly influenced by the number of rough interfaces: two rough interfaces along the *x-y* planes in IPNF, and four in NW.

As the width increases, thermal conductivities exhibit an increase towards the CPNF values for both IPNFs and NWs. Once the device width exceeds the length, the impact of rough boundaries becomes less significant, resulting in a close alignment of thermal conductivity behaviors for all device types at widths around 10 μm. From these observations, we conclude that the reduction in thermal conductivity in the diffusive transport regime is intricately linked to the number of rough boundaries.

3.2.3 Degree of ballistic transport via the Knudsen number

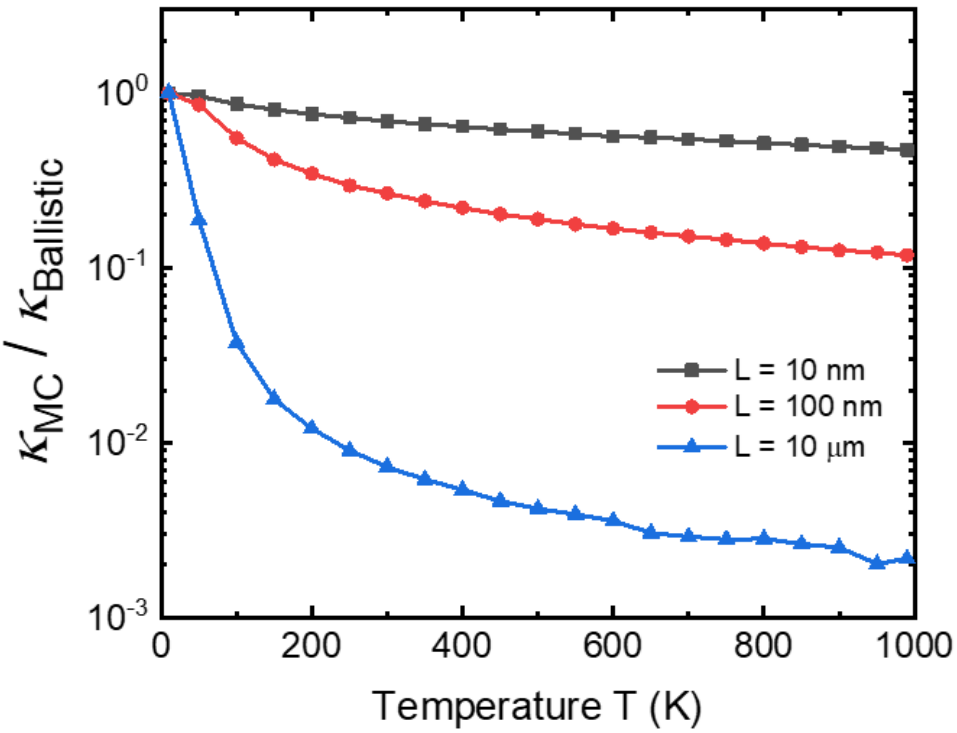

Figure 3.7 The Knudsen number calculated by MC simulation as a function of temperature for CPNF with three different device lengths.

In the previous Section 3.2.2, it is established that the transition through ballistic, intermediate, and diffusive transport regimes depends on the device length. We now extend this study to explore how these regimes change across a temperature ranging from 0.1 to 1000 K, aiming to comprehend the transition between different transport modes as temperature varies.

To facilitate this study, the concept of the Knudsen number (K_D) is adopted as a tool for characterizing the degree of ballistic transport [240,241]. This dimensionless number is defined as the ratio of the thermal conductivity calculated by MC simulation to the ballistic one (Equation 2.37). While this interpretation of K_D slightly deviates from its traditional definition based on the mean free path and characteristic

dimensions, it remains consistent with the original intent.

Figure 3.7 presents the variation of the Knudsen number with temperature, ranging from 0.1 to 1000 K for CPNF of three distinct lengths : 10 nm in black (mimicking ballistic case), 100 nm in red, and 10 µm in blue. If the value of K_D is 1, it means that the system is operating in a fully ballistic transport regime, where heat carriers move freely without colliding with each other. For the ultra-short 10 nm device, the Knudsen number remains above 0.5 across the entire temperature range, indicating that ballistic transport is the dominant heat conduction mechanism with minimal phonon scattering events.

At a length of 100 nm, K_D values fall between 0.1 and 0.8, evidence of an intermediate transport regime where both ballistic and diffusive characteristics are mixed, except for regions at very low temperatures. In this regime, phonons begin to interact with each other, but there is still a significant probability of ballistic movement. Conversely, in a 10-µm long device, K_D values decrease dramatically with rising temperature, signifying a rapid transition from ballistic to diffusive transport. At 300 K, K_D drops below 0.01, denoting a predominantly diffusive transport regime.

This analysis not only highlights the crucial role of temperature in determining the dominant transport mechanisms, but also elucidates the complex interplay between device size and thermal conditions via the Knudsen number.

3.2.4 Modal contribution of each phonon modes

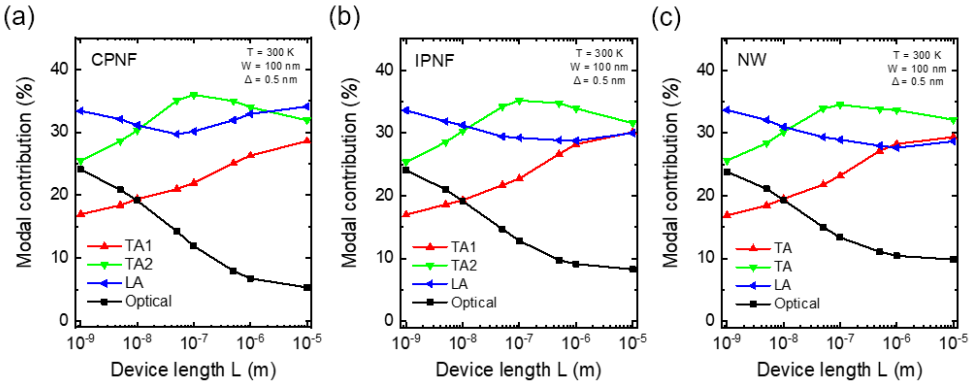

Figure 3.8 Modal contributions of each phonon mode to the total heat flux as a function of length L for (a) CPNF, (b) IPNF, and (c) NW at 300 K.

The influence of device size and temperature on thermal conductivity has been analyzed within GaAs nanostructures, confirming their impact on heat transport regimes. Our current focus moves to the contributions of individual phonon modes to heat transport through numerical Monte Carlo simulations. As said before, GaAs possesses three acoustic and three optical phonon modes. To facilitate a view of the overall trends, the contributions from the optical modes are aggregated into one single "optical" category.

Figure 3.8 shows the modal contributions of each phonon mode to the total heat flux density with device lengths for (a) CPNF, (b) IPNF, and (c) NW at 300 K. The sum of all contributions for each length equals 100 %, which shows how much each phonon mode contributes relatively to the total heat flux. Even though the total amount of heat flux varies across the structures, the relative contributions of each mode are consistent via normalization.

For all structures, the contribution of optical modes remains below 10 % in a 10 µm long device with similar properties to the bulk state [55]. Such a low contribution from optical modes can be expected from material properties due to their relatively low group velocities and shorter lifetimes (cf. Figure 3.2). As a result, their role in the thermal

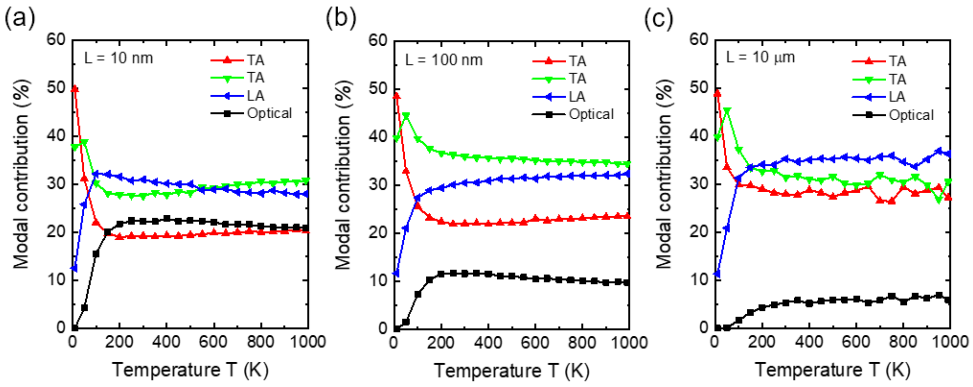

Figure 3.9 Temperature-dependent modal contributions to the total heat flux density in CPNF for device lengths of (a) 10 nm, (b) 100 nm, and (c) 10 µm.

dynamics of bulk systems is often overlooked [54]. On the other hand, the combined contributions of the three acoustic modes exceed 90 %, indicating that they are responsible for most heat transfer regardless of device type. Notably, the LA mode, with its high group velocity, maintains a substantial contribution across all device lengths and types.

However, as the device length decreases, a rapid increase in the contribution of optical modes is observed within nanostructures. At 10 nm device length, corresponding to the ballistic transport regime, their contributions overcome 20 %, making them a non-negligible factor. This trend of increasing optical mode contribution in shorter nanostructures has also been previously observed in silicon [155]. Furthermore, since this trend is evident across all device types, it is independent of the structural influence of rough boundaries.

As the difference in mode contribution depending on the device type is small, we measure the modal contributions at lengths of 10 nm, 100 nm, and 10 µm in CPNF to investigate the temperature-dependent behavior of phonon modes, as depicted in Figure 3.9 (a), (b), and (c), respectively. At low temperatures below 100 K, the LA and optical modes with relatively high frequencies are difficult to thermally activate, therefore resulting in low contributions across all device lengths. Beyond approximately 200 K, the contributions from each mode stabilize and remain almost uniform with temperature changes.

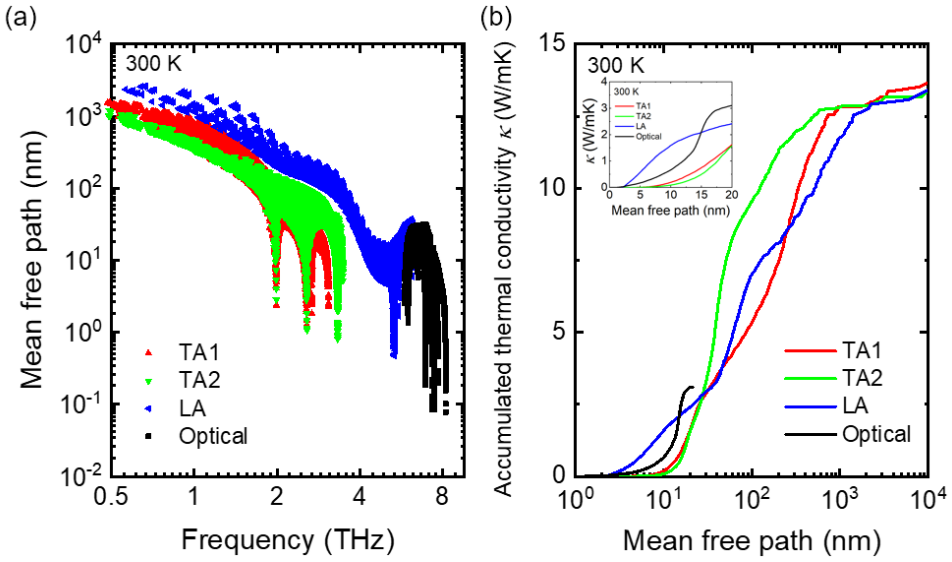

Figure 3.10 (a) The calculated phonon mean free path (MFP) as a function of frequency and (b) accumulated thermal conductivity with respect to mean free path for individual phonon modes at 300 K. The inset shows a zoomed-in view of the accumulated thermal conductivity for phonon modes within the mean free path range of 0 to 20 nm.

In ultra-short devices with a length of 10 nm (mimicking ballistic case), the contribution of optical modes exceeds 20 %, confirming their importance in heat transfer at this scale, except for temperatures below 100 K. As device length increases, the influence of optical modes declines to around 10 % and 5 % for 100 nm and 10 µm devices, respectively. The slight fluctuations observed in the 10 µm device can be attributed to challenges inherent in the numerical MC simulations for longer devices. These challenges stem from the increased computational complexity and the need for more simulation iterations to achieve statistical convergence in extended structures. Nonetheless, these minor deviations do not impede the analysis of the general trends in Figure 3.9 (c).

To better understand the influence of optical modes within nanostructures, the phonon mean free path (MFP) for each mode is investigated which is calculated by multiplying their group velocities with their lifetimes from ab-initio data. Acknowledging that the

contribution of each mode to heat transport remains relatively unchanged with temperature, our calculations on the mean free path (MFP) are focused at a standard temperature of 300 K.

Figure 3.10 (a) presents the phonon mean free path for each mode as a function of frequency at 300 K. While the acoustic modes exhibit mean free paths ranging from a few nm to over 1 μm near the Γ point, the MFPs for optical modes are much lower, typically well below 100 nm. Therefore, the relatively short MFPs of optical modes have less impact on the thermal conductivity than acoustic modes in longer devices.

To analyze the pronounced increase in the contribution of optical modes as device length decreases, the accumulated thermal conductivity is calculated with respect to the mean free paths of each mode, as shown in Figure 3.10 (b). As expected, most of the thermal conductivity is determined by acoustic phonons with MFPs longer than 100 nm. However, in the MFP range of less than 10 nm, contributions to the thermal conductivity are mainly due to LA and optical modes. This result explains the findings in Figure 3.8, where the LA mode exhibits the highest modal contribution in nanostructures with lengths below 10 nm. Moreover, the sharp increase in accumulated thermal conductivity within this MFP range suggests that optical phonons can transport heat more effectively, contributing substantially to the overall thermal conductivity, as shown in the inset of Figure 3.10 (b). Hence, it reflects that within device lengths comparable to the MFP of optical modes, optical phonons can travel further with reduced scattering, making them more efficient heat carriers in thermal transport.

This study demonstrates why optical modes have a considerable contribution to nanostructures and why their impact surges as the device length shortens. Through this study, it reveals that phonon mode contributions to thermal transport are significantly influenced by device size. These size-dependent characteristics provide an indirect but effective indicator to discern the transport regimes within these nanostructures. This approach offers valuable insights for the strategic design to optimize thermal properties.

3.2.5 Degradation effect of nanopores in GaAs porous nanowire

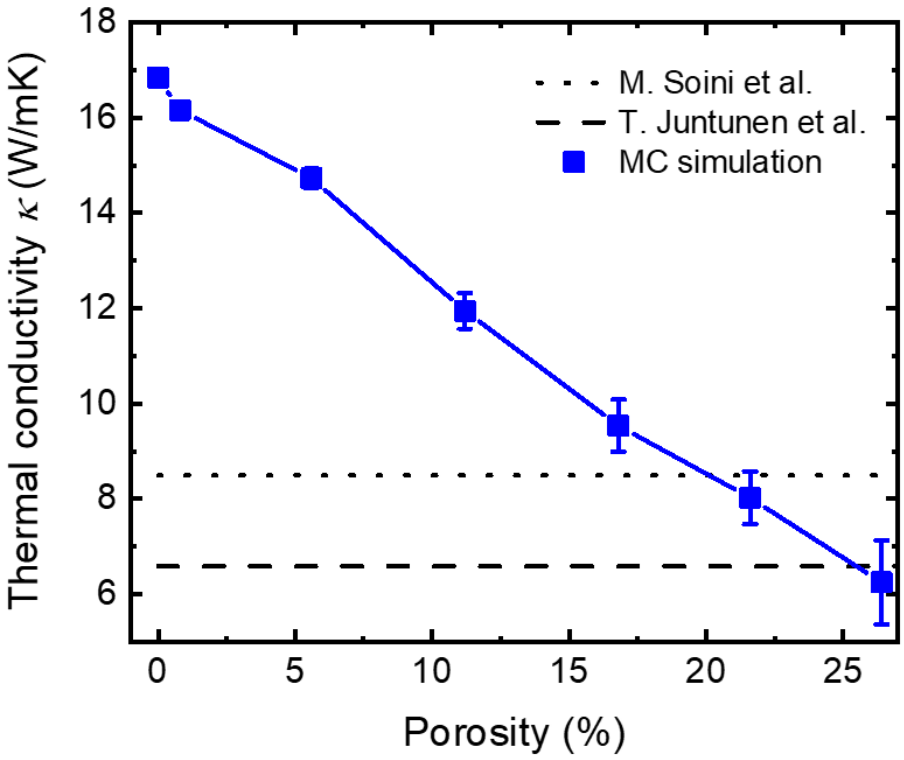

Figure 3.11 The thermal conductivity against porosity for GaAs porous nanowires. The blue squares represent MC simulation results. Experimental data from M. Soini et al. (dotted lines) [43] *and T. Juntunen et al. (dashed lines)* [48].

This study advances the design of nanostructures within MC simulations to investigate the characteristics of porous nanowires. Figure 3.11 provides a comparative analysis between the thermal conductivity results from MC simulations of porous nanowires (blue squares) and experimental data from M. Soini et al. (dotted lines) [43] and T. Juntunen et al. (dashed lines) [48]. For the simulation, the length of NW is set to 1 μm with a 100 nm square cross-sectional dimensions (width and height), aligning the scale with that of the experimental NWs, which have around 100 nm diameter.

It is found that the thermal conductivity of normal NW at 0 % porosity is approximately twice as high as experimental values. This discrepancy can prompt an exploration into the possibility of unintentional nanopore formation within NWs during the experimental synthesis process. Various synthesis techniques such as molecular beam epitaxy (MBE) [43], metalorganic vapor-phase epitaxy (MOVPE) [48], and vapor-liquid-solid (VLS) method [269] have unique influences on the nanowire quality. In these processes, variables such as precursor concentration, temperature, catalyst size, and growth time, as well as factors like strain effects, phase transitions, and surface energy can contribute to the formation of internal nanopores [44,270].

By considering the complexities involved in the VLS method with potential for porous NW, the design of nanowires with MC simulations is aimed to provide a realistic representation of the experimental conditions with a three-dimensional cubic mesh, structured in 5 x 5 x 5 cells along the *x*, *y*, and *z* axes, respectively. This mesh is configured to randomly introduce nanopores according to the specified porosity, and their boundaries are treated as fully diffusive to mimic the effect of nanopores with zero transmittance. Excluding the case of 0% porosity, ten different configurations are generated to account for the random distribution of nanopores for each porosity level. This randomness leads to slight variations in the results for each configuration. To provide a statistically reliable representation of these variations, error bars calculated with a 99 % confidence interval are included, as shown in Figure 3.11.

Within a low porosity range, specifically below 5 %, the impact of nanopores on thermal conductivity appears minor and shows minimal variation in results, as indicated by the imperceptible error bars. As the porosity increases, however, a significant degradation effect of nanopores on the thermal conductivity becomes evident with the increasingly varied influence of nanopore distribution.. The calculated thermal conductivities fit the experimental data of M. Soini et al. at 20 % porosity, and our results closely match the values reported by T. Juntunen et al. within the margin of error for a porosity of approximately 25 %.

This highlights the important role of nanopores as phonon scattering

sites, thus reducing the efficiency of heat transfer. Even if the lower experimental values may not be solely attributable to internal nanopores, the significance of this study remains pertinent because it provides a comprehensive understanding of how microstructural variations influence macroscopic thermal properties.

3.3 SUMMARY

In this chapter, we have explored the thermal transport characteristics of GaAs nanostructures via Monte Carlo simulations. The ab-initio derived material properties of bulk GaAs validate the computational approach against experimental data and provide a solid foundation for subsequent MC simulations. Thus, it reinforces the applicability of DFT and DFPT in capturing the essential physics of phonon transport.

Through the precise design of GaAs nanostructures with the implementation of boundary conditions, it is shown that the thermal conductivity is highly dependent on device dimensions and temperature. This study also provides insights into the transport regime transition from ballistic to diffusive regimes by means of the Knudsen number. The modal contributions of phonon modes to thermal transport make it possible to reveal the substantial contribution of optical modes, especially in lengths corresponding to their mean free path. The final section addresses the degradation effect of nanopores on the thermal conductivity of GaAs nanowires, considering potential imperfections in the synthesis process. Nevertheless, a more accurate simulation, including the complexity of the fabrication process, remains a challenge. Further investigation is required to capture their subtleties of phonon scattering and transport with greater precision.

Throughout this chapter, the effect of device size, boundary effects, and temperature on thermal conductivity has been meticulously analyzed, and it could be widely used to explore the thermal properties of various materials and nanostructures for optimizing nanostructure designs to achieve desired thermal transport properties. In the next chapter, this simulation methodology will be applied to investigate two-dimensional materials and their various structural configurations, extending the scope of our research into novel material systems.

4 FULL BAND MONTE CARLO SIMULATION OF THERMAL TRANSPORT ACROSS LATERAL INTERFACE BETWEEN 2D MATERIALS

Chapter 4 extends beyond the study of bulk material covered in Chapter 3, exploring the thermal properties of novel two-dimensional (2D) materials using full-band Monte Carlo (MC) simulations. The main focus lies on exploring the lateral heterostructures based on various 2D materials, such as hexagonal boron nitride (h-BN), graphene, molybdenum disulfide (MoS_2), and tungsten diselenide (WSe_2). It offers a comprehensive investigation of the unique characteristics within these structures, mainly focusing on the transport of phonons across the interfaces.

Section 4.1 begins with a detailed discussion of the density functional theory (DFT) calculations for 2D materials like h-BN, graphene, MoS_2, and WSe_2. These calculations provide essential material properties, including phonon dispersions, velocities, and scattering rates, vital for MC simulations. (4.1.1). Then, a comparative thermal conductivity analysis against experimental data is presented to validate the accuracy and reliability of the DFT calculations used in the study (4.1.2).

Next, Section 4.2 advances into the realm of lateral heterostructures, describing h-BN/graphene (4.2.1) and MoS_2/WSe_2 combinations (4.2.2). In the device geometry, the lateral interface between 2D materials is defined by the diffuse mismatch model (DMM). The study investigates the interface thermal conductance (ITC) and examines the evolution of phonon modal contributions near the interface. A key aspect of this study is the implementation of directional temperature in calculating the ITC. The use of directional temperature not only accurately determines the ITC but also sheds light on the complex thermal dynamics within these nanostructures.

4.1 2D MATERIALS

4.1.1 DFT calculations for 2D materials

Before the investigation of devices based on 2D monolayer materials (h-BN, graphene, MoS_2, WSe_2), our study employs ab-initio calculations to derive material properties such as phonon dispersions, phonon group velocities, and scattering rates, which are essential as input parameters for subsequent MC simulations. Detailed discussions on each material and the rationale behind their selection are comprehensively presented in Chapter 2. The prefix '2D' or 'monolayer' before each material name is omitted throughout the text for consistency and brevity. Ab-initio calculations are performed using the Quantum ESPRESSO suite together with the local-density approximation (LDA) and norm-conserving pseudopotentials [150,151]. Despite the known limitations of LDA in accurately representing layered materials, mainly due to the lack of van der Waals (vdW) interactions, it has nonetheless been shown to compute phonon characteristics with high accuracy for the materials investigated in this study [69,150].

For electronic calculations, the in-plane lattice parameters are 2.5045 Å for h-BN, 2.4381 Å for graphene, 3.1880 Å for MoS_2, and 3.3171 Å for WSe_2, which are close to the experimental values, respectively [271–274]. The vacuum separation is set to 7 Å along the z-direction to prevent non-physical interactions between the periodic images. The k-point meshes for Brillouin zone sampling are 24 x 24 x 1 for h-BN, 16 x 16 x 1 for both graphene and MoS_2, and 8 x 8 x 1 for WSe_2. The plane-wave energy cutoff is 100 Ry to achieve the energy convergence and, given graphene's semi-metallic nature, cold smearing of 0.25 Ry is used.

Except for WSe_2, the harmonic second-order and anharmonic third-order force constants are performed using q-point meshes of 16 x 16 x 1 and 4 x 4 x 1, respectively. In the case of WSe_2, the meshes used are 4 x 4 x 1 and 2 x 2 x 1, respectively. Finally, all phonon properties are calculated using a well-converged mesh of 128 x 128 x 1 q-points with a Gaussian broadening of 10 cm^{-1} for h-BN, graphene, and WSe_2. For MoS_2, a mesh of 140 x 140 x 1 q-points and a broadening of 2 cm^{-1}

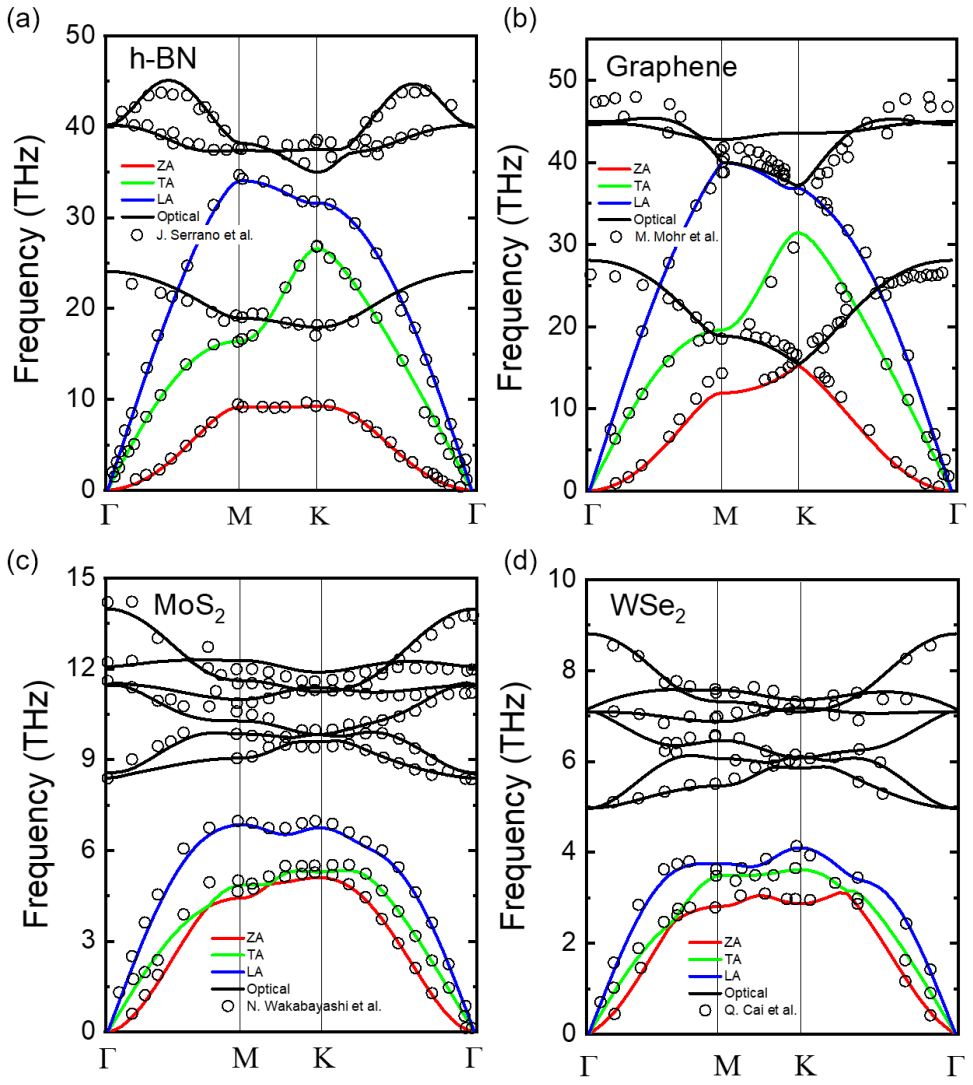

Figure 4.1 Calculated phonon dispersions for (a) h-BN, (b) Graphene, (c) MoS_2, and (d) WSe_2 along the high symmetry paths as compared to the experimental data [275–278].

are used. Detailed methodology and application of ab-initio calculation for phonon are already discussed in Chapter 3.

Figure 4.1 shows the calculated phonon dispersion compared with experimental results along the high symmetry paths. The solid lines represent the theoretical predictions of our DFT calculations, while the

open circles indicate the values obtained from experimental measurements. The experimental data for h-BN, graphene, and WSe_2 determined from inelastic x-ray scattering (IXS) measurement, and the data for MoS_2 are measured by neutron scattering technique [275–278]. It can be appreciated a satisfactory agreement between the calculated and experimental data, validating the accuracy of our model, and our results do not suffer from unphysical negative frequencies.

Both h-BN and graphene have two atoms per primitive cell, resulting in six phonon modes: longitudinal acoustic (LA), transverse acoustic (TA), and flexural acoustic (ZA), modes and three optical modes (ZO, TO, LO). Their phonon dispersions extends up to approximately 50 THz. The modes with the lowest frequencies in both the acoustic and optical branches are associated with their out-of-plane motion, respectively. In the vicinity of the Gamma point (Γ), the ZA mode displays the quadratic dispersion, while the LA and TA modes exhibit linear dispersion, showing the in-plane stiffness of the lattice.

In contrast to bulk h-BN, which is a polar material, the LO–TO splitting caused by long-range Coulomb interactions at the Gamma point is not observed due to the unique characteristics of the 2D material [279], as shown in Figure 4.1 (a). For graphene, as demonstrated in Figure 4.1 (b), while there are some discrepancies in the optical modes compared to experimental results, overall the phonon dispersion shows excellent agreement with the experimental data..

In Figure 4.1 (c) and (b), the phonon dispersion relations for MoS_2 and WSe_2 are illustrated, respectively. Both MoS_2 and WSe_2 contain three atoms per primitive cell, with a central layer of Mo or W atoms, each covalently bonded and sandwiched between two layers of S or Se atoms [280]. This tri-layered atomic arrangement presents a more complex phonon spectrum with three acoustic and six optical modes than that of binary compounds such as h-BN and graphene. Note that we consider the optical modes collectively rather than distinguishing between them in detail, which is beyond the scope of this study.

The acoustic modes of MoS_2 and WSe_2 exhibit a less pronounced dispersion. At higher frequencies, the optical modes reflect the mass difference between the heavier transition metal atoms (either Mo with

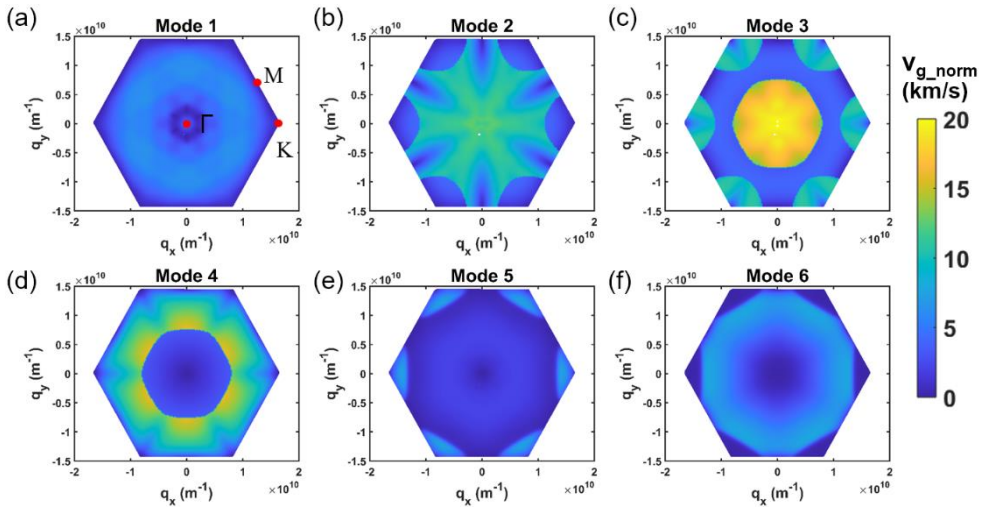

Figure 4.2 Cartography of the phonon group velocity for h-BN over all Brillouin zone at 300 K. Panels (a)-(f) depict the group velocities for modes 1 to 6. High symmetry points are marked with red dots in panel (a).

an atomic mass number of 95.95 or W with 183.84) and the lighter chalcogenide atoms (either S with an atomic mass number of 32.06 or Se with 78.97) [281]. The substantial atomic masses in TMDCs account for their lower optical frequencies when contrasted with h-BN and graphene, which are composed of lighter atoms. Furthermore, the significant mass disparity in MoS_2 and WSe_2 leads to a broader phonon spectrum due to the different relative movements of the heavier and lighter atoms. For WSe_2, while its phonon dispersion closely resembles that of MoS_2, it has a generally lower frequency range because the atomic mass of W is approximately twice that of Mo.

Figure 4.2 presents a detailed cartographic representation of phonon group velocities, which are computed as the norm at each q-point across the full Brillouin zone for h-BN at 300 K. Unlike 3D systems such as GaAs in Chapter 3, 2D materials allow for the entire BZ to be intuitively visualized through contour mapping. High symmetry points in the Brillouin zone are indicated by red dots in panel (a). Panels (a) through (f) in Figure 4.2 display the group velocities for modes 1 to 6, categorizing modes 1 to 3 as acoustic and modes 4 to 6 as optical.

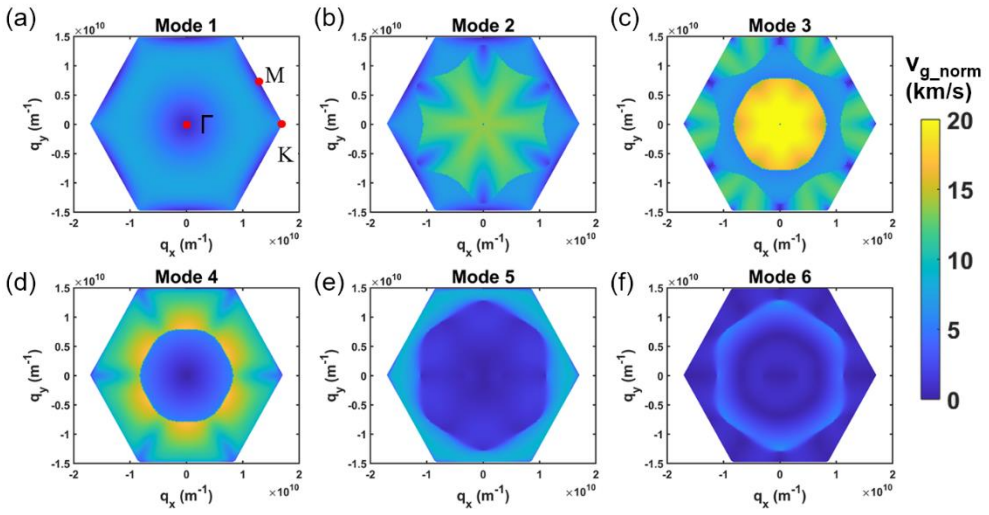

Figure 4.3 Cartography of the phonon group velocity for graphene over all Brillouin zone at 300 K. Panels (a)-(f) depict the group velocities for modes 1 to 6.

The results reveal that the phonon group velocities are distinctly non-isotropic. Such anisotropy emphasizes the importance of employing a full-band description of the BZ rather than relying on a simplified isotropic analytical formula. In mode 3, which corresponds to the LA mode, we observe the highest group velocity near the Gamma point. This is consistent with the expected behavior of LA mode shown in Figure 4.1 (a).

Similar to Figure 4.2 for h-BN, Figure 4.3 displays the group velocity distribution for graphene, mapped over the same velocity range for 0 to 20 km/s. The overall patterns of group velocity distribution in graphene appear analogous to those in h-BN. But, the brighter colors in the acoustic modes from mode 1 to 3 for graphene indicate higher group velocities when compared to h-BN.

Figure 4.4 and 4.5 illustrate the phonon group velocity distribution for MoS_2 and WSe_2, respectively, which, in contrast to h-BN and graphene, features a total of nine phonon modes due to its more complex structure. Thus, modes 1 through 3 are the acoustic phonon modes, while modes 4 through 9 represent the optical phonon modes.

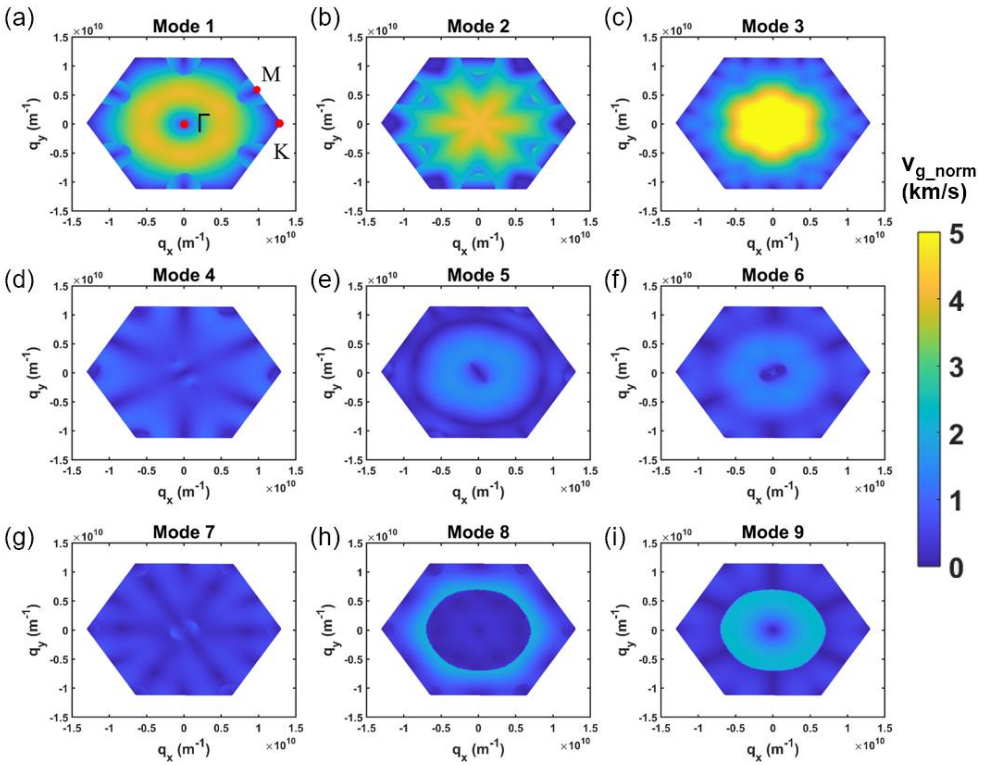

Figure 4.4 Cartography of the phonon group velocity for MoS_2 over all Brillouin zone at 300 K. Panels (a)-(i) depict the group velocities for modes 1 to 9.

Reflecting their distinct vibrational properties, expected to lower group velocities when compared to the aforementioned 2D materials, a velocity range is adjusted to 0 to 5 km/s.

As a result, both MoS_2 and WSe_2 exhibit reduced phonon group velocities, a consequence of the higher atomic masses of their constituent transition metal and chalcogenide atoms. Specifically, mode 3 (LA) near the Gamma point displays the highest group velocities in both materials. Across the Brillouin zone, modes 1 and 2 of MoS_2 show generally higher velocities than those in WSe_2.

In the optical region, encompassing modes 4 through 9, both materials demonstrate comparably low group velocities, suggesting a minor contribution from these modes to thermal transport compared to

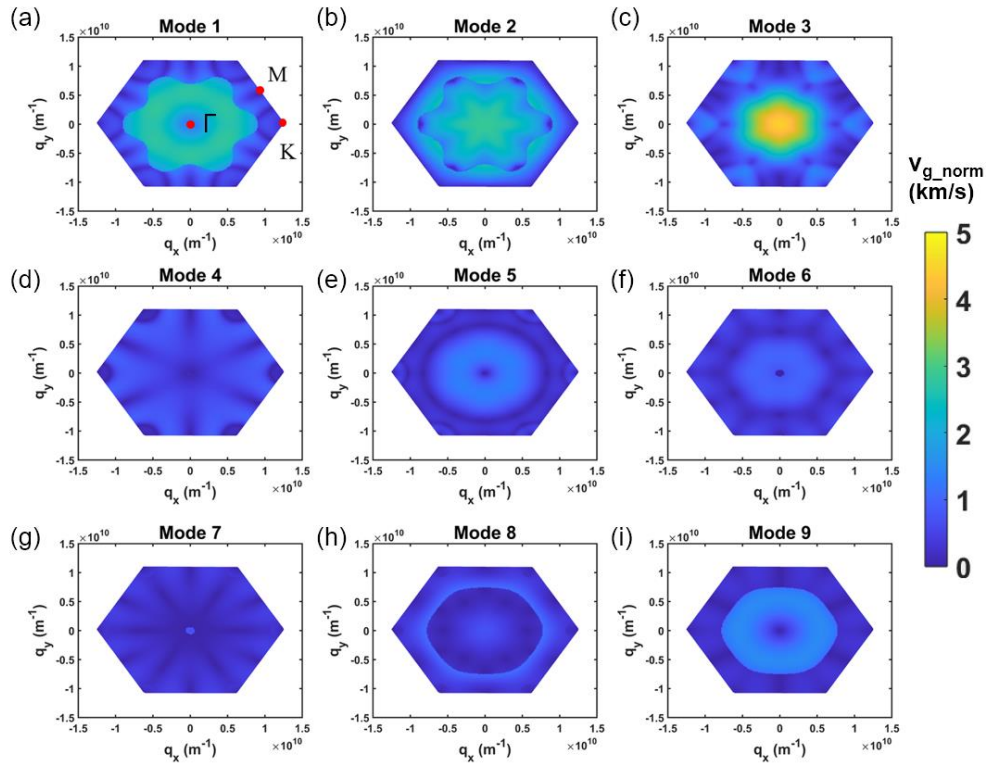

Figure 4.5 Cartography of the phonon group velocity for WSe_2 over all Brillouin zone at 300 K. Panels (a)-(i) depict the group velocities for modes 1 to 9.

acoustic modes. However, a subtle distinction is observed in modes 8 and 9, where MoS_2 has more pronounced regions of higher velocity, inferring that WSe_2 may possess the lowest thermal transport properties. By integrating these findings with the phonon scattering rates discussed in next page, the thermal conductivity of each material can be predicted with high accuracy.

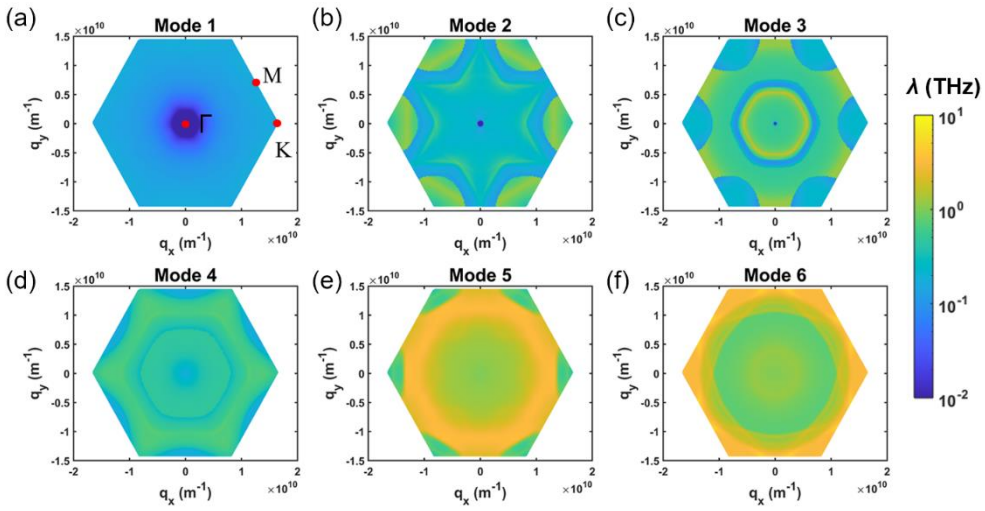

Figure 4.6 Cartography of the phonon scattering rate for h-BN over all Brillouin zone at 300 K. Panels (a)-(f) depict the scattering rates for modes 1 to 6. High symmetry points are marked with red dots in panel (a).

Figure 4.6 shows the cartography of phonon scattering rates, which are the sum of the contributions of normal, Umklapp, and isotope scattering mechanisms at each q-point across the entire Brillouin zone for h-BN at 300 K. As with Figure 4.2, the data is organized for modes 1 to 6, with modes 1 to 3 represented as acoustic and modes 4 to 6 as optical. Due to the wide range of scattering rates, which span several orders of magnitude, a logarithmic scale is employed to map values across a spectrum ranging from 10^{-2} to 10^{1} THz. This figure provides a clear visualization of the scattering rate's variation, offering insights into the dynamic phonon interactions within h-BN.

The acoustic modes 1 to 3 in Figure 4.6 (a) to (c) exhibit markedly low scattering rates near the Gamma point, with this trend being most pronounced for mode 1. In mode 2, heightened phonon scatterings are displayed at the K points, while mode 3 is characterized by stronger scattering at the M points. Such localized scattering phenomena suggest that interactions at specific symmetry points in the BZ are more likely to disrupt phonon transport in these modes. Remarkably,

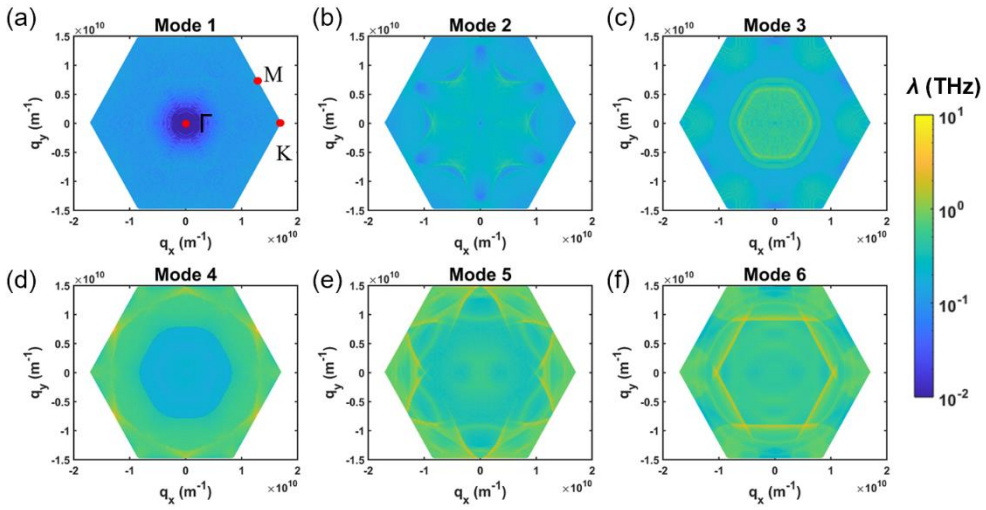

Figure 4.7 Cartography of the phonon scattering rate for graphene over all Brillouin zone at 300 K. Panels (a)-(f) depict the scattering rates for modes 1 to 6.

modes 5 and 6, corresponding optical modes, show consistently high scattering rates throughout the BZ. This widespread scattering implies that these optical modes may be significantly impeded by interactions, leading to a diminished thermal transport property.

In Figure 4.7, the phonon scattering rates at 300 K are illustrated for graphene across the BZ, using the same logarithmic scale range as used to h-BN. A comparison with the h-BN results reveals a universally lower scattering rate across all phonon modes in graphene. In particular, this is noteworthy in modes 5 and 6, where the scattering rates remain low, showing the exceptional characteristics of graphene. Composed solely of carbon atoms with sp^2 hybridization, these strong bonds are less susceptible to vibrational disruption, resulting in lower phonon scattering rates. Therefore, even though graphene exhibits phonon dispersion and group velocity profiles similar to those of h-BN, these results are strongly correlated with the superior thermal conductivity of graphene.

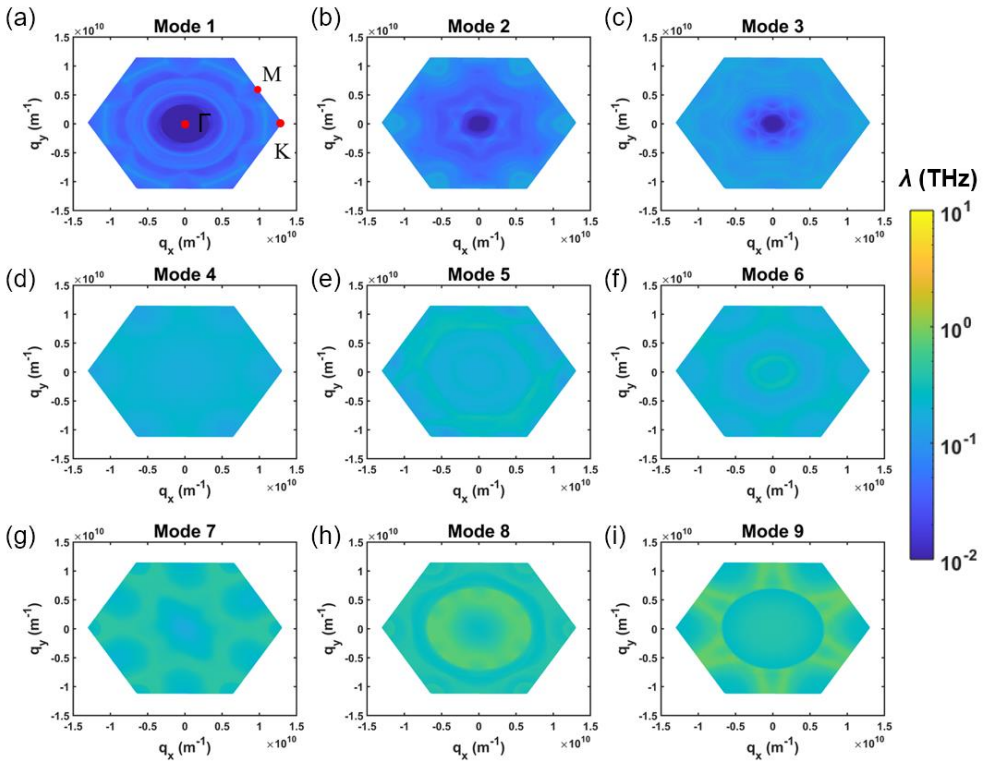

Figure 4.8 Cartography of the phonon scattering rate for MoS_2 over all Brillouin zone at 300 K. Panels (a)-(i) depict the scattering rates for modes 1 to 9.

Figures 4.8 and 4.9 illustrate the phonon scattering rates for MoS_2 and WSe_2, respectively, including nine distinct phonon modes. For direct comparison, the identical logarithmic scale range as h-BN and graphene has been employed. Across all modes, MoS_2 shows small scattering rates near the Gamma point in the acoustic modes 1 to 3, even less than in h-BN and graphene. Similarly, scattering rates in the optical modes are observed below 10 THz as shown in Figure 4.8 (d) to (i). However, considering lower group velocities of MoS_2, its thermal conductivity properties are likely to be lower compared to h-BN and graphene.

In the case of WSe_2, the behavior diverges significantly from that of MoS_2. Except for modes 4 and 5, WSe_2 exhibits strong phonon scattering across the modes. Interestingly, mode 7 shows a significant scattering peak at the Gamma point. This could be due to the heavier

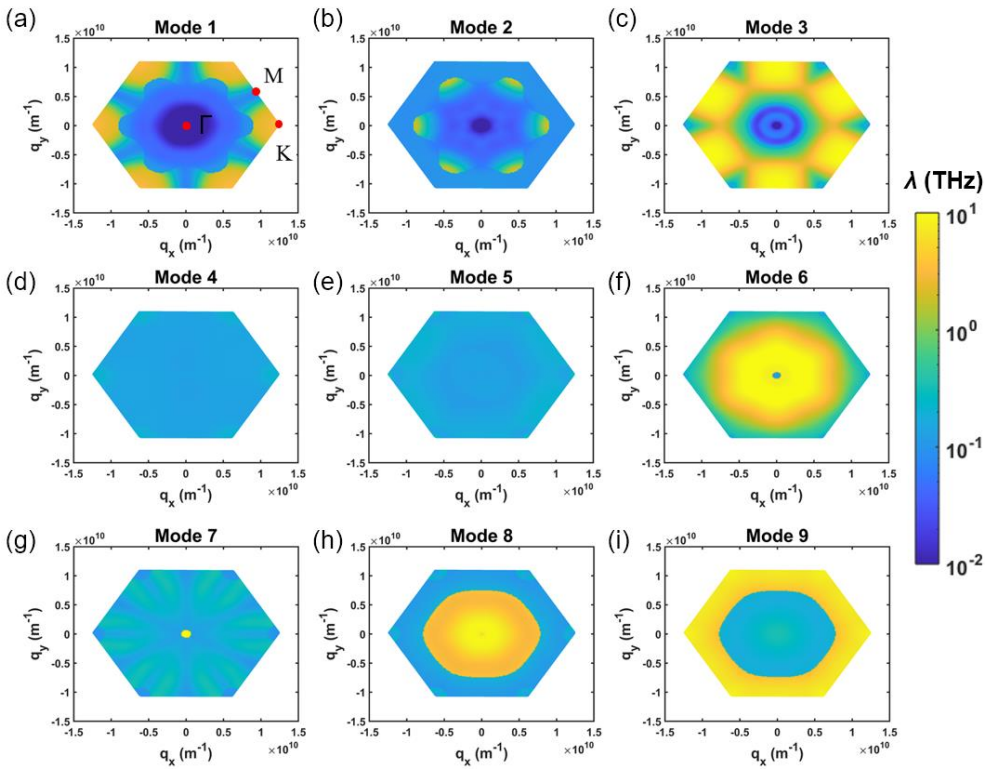

Figure 4.9 Cartography of the phonon scattering rate for WSe_2 over all Brillouin zone at 300 K. Panels (a)-(i) depict the scattering rates for modes 1 to 9.

atomic mass of Se compared to S in MoS_2, which can lead to a higher degree of anharmonicity in the lattice vibrations and hence increased phonon interactions and scattering. Consequently, this substantial phonon scattering implies a reduced phonon lifetime, which could adversely affect the thermal conductivity of WSe_2. The observed scattering behavior provides valuable insights into the intrinsic phonon scattering mechanisms at play within 2D materials.

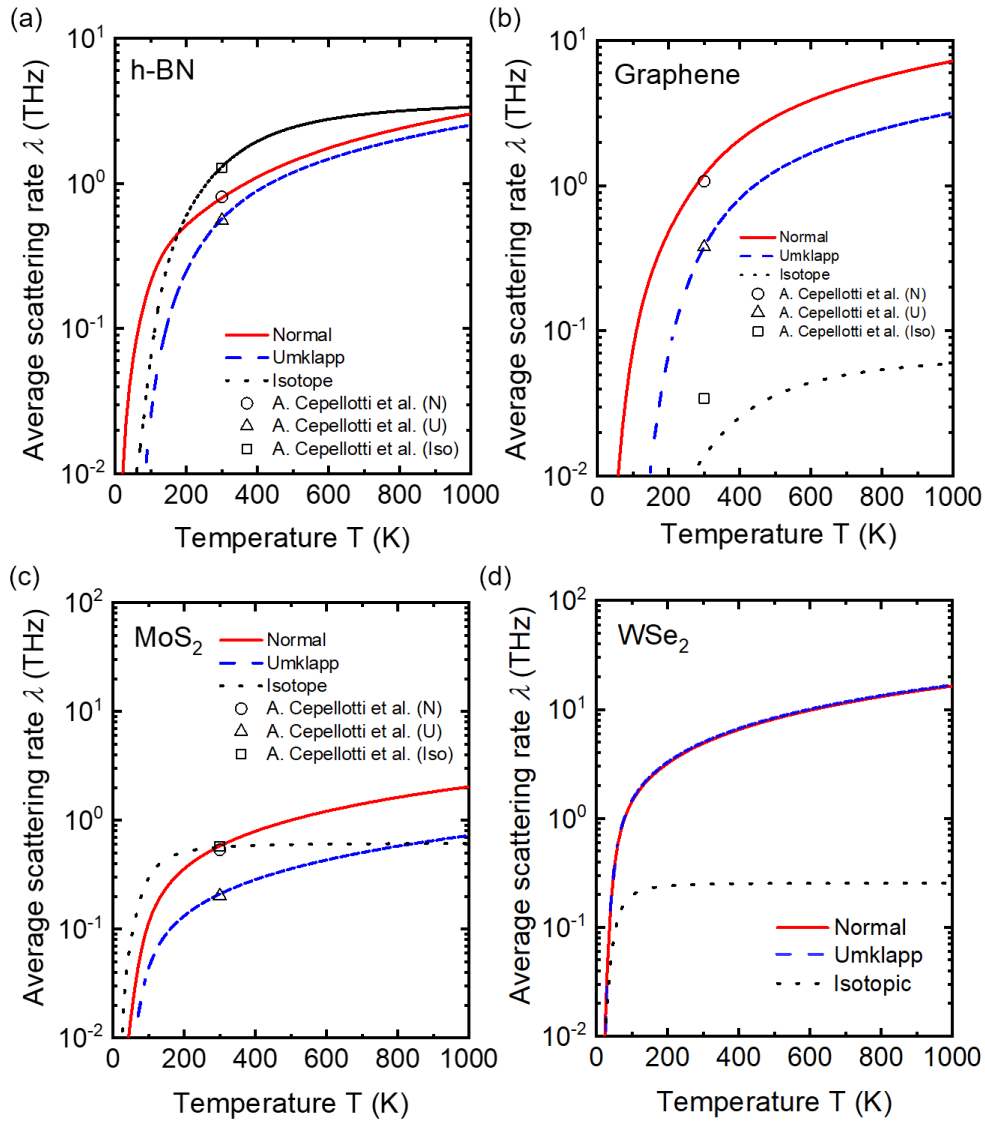

Figure 4.10 Average phonon scattering rates for (a) h-BN, (b) Graphene, (c) MoS_2, and (d) WSe_2. These rates, which include normal (red solid line), Umklapp (blue dashed line), and Isotope (black dotted line) processes, are plotted as functions of temperature, ranging from 0.1 to 1000 K. Data points from the work of A. Cepellotti et al. at 300 K are denoted by symbols [69]*: circles for normal (N) processes, triangles for Umklapp (U) processes, and squares for isotope (Iso) scattering.*

To further comprehensive analysis, we examine the average phonon scattering rates for h-BN, graphene, MoS_2, and WSe_2 over an extensive temperature range from 0.1 to 1000 K. The analysis distinguishes the phonon scattering processes into normal (N) and Umklapp (U) events, as well as to isotope scattering (Iso), with in-depth definitions and explanations provided in Section 2.1.3. The average scattering rate of each mechanisms is expressed as

$$< \lambda^i > = \frac{\sum_s f_{BE,s}(f_{BE,s}+1)\frac{(\hbar\omega_s)^2}{k_B T^2}\lambda_s^i}{\sum_s f_{BE,s}(f_{BE,s}+1)\frac{(\hbar\omega_s)^2}{k_B T^2}} \tag{4.1}$$

where i refers to each scattering processes (N, U, Iso), and $f_{BE,s}$ is the Bose-Einstein distribution function for a phonon in state s. For phonon-isotope scattering, natural isotopic concentrations are chosen: B (19.9% ^{10}B, 80.1% ^{11}B), N (99.634% ^{14}N, 0.366% ^{15}N), C (98.93% ^{12}C, 1.07% ^{13}C), Mo (14.77% ^{92}Mo, 9.23% ^{94}Mo,15.9% ^{95}Mo, 16.68% ^{96}Mo, 9.56% ^{97}Mo, 24.19% ^{98}Mo, 9.67% ^{100}Mo), S (94.99% ^{32}S, 0.75% ^{33}S, 4.25% ^{34}S, 0.01% ^{36}S), W (0.12% ^{180}W, 26.5% ^{182}W, 14.31% ^{183}W, 30.64% ^{184}W, 28.43% ^{186}W), and Se (0.89% ^{74}Se, 9.37% ^{76}Se, 7.63% ^{77}Se, 23.77% ^{78}Se, 49.61% ^{80}Se, 8.73% ^{82}Se) [281].

Figure 4.10 shows the temperature dependence of the average phonon scattering rates for h-BN, graphene, MoS_2, and WSe_2, respectively. The normal scattering is represented by a red solid line, Umklapp scattering by a blue dashed line, and isotope scattering by a black dotted line. Except WSe_2, comparative values at 300 K have been extracted from existing literature where analogous calculations were performed [69].

Across all examined materials, the phonon-phonon scattering mechanisms, corresponding normal and Umklapp events, increase with temperature because the increased vibrational energy by high temperature raises the likelihood of phonons interacting with one another. However, phonon-isotope scattering exhibits a slightly different temperature dependence since the isotopic composition remains constant with temperature, except at low temperatures where anharmonic effects are suppressed.

For h-BN in Figure 4.10 (a), a distinctive feature of 2D materials is highlighted that normal scattering dominates over Umklapp scattering at all temperatures. The reduced dimensionality amplifies the role of normal scattering, which enables phonons to largely conserve their momentum. This prominent behavior indeed has implications for phonon transport and its hydrodynamics behavior in 2D system [282]. In the hydrodynamic regime, phonons could propagate in collective wave-like motions, also referred to as 'second sound' [69,283]. Additionally, the substantial isotope mixture in B atoms in h-BN leads to strong phonon-isotope scattering that surpasses phonon-phonon scattering beyond 200 K, highlighting the importance of considering this effect in thermal transport simulations.

In graphene, the dominance of normal processes over Umklapp processes is even more pronounced than in 2D h-BN, as shown in Figure 4.10 (b). The strong covalent bonds between carbon atoms in graphene are a major factor contributing to this dominance of normal processes. The flexural phonon modes are significant contributors to thermal transport due to its strong carbon bonding and highly symmetric structure, which in turn lead to enhanced normal scattering [71]. Regarding isotope scattering, although there are slight differences in the literature, its impact is relatively low in graphene, primarily attributed to the material's pure carbon composition. This results in remarkably high graphene's thermal conductivity, as phonons carry thermal energy more efficiently across the lattice with fewer interruptions.

Figure 4.10 (c) displays the investigation of MoS_2 showing a trend similar to that of h-BN and graphene, where normal scattering processes take precedence over Umklapp events. This tendency becomes more pronounced at temperatures exceeding ambient conditions. A noteworthy observation is that phonon-isotope scattering in MoS_2 is comparable to phonon-phonon scattering at 300 K. This can be attributed to the presence of various isotopes of the Mo atom. The data provided by A. Cepellotti et al. align precisely with these findings.

Contrary to the scattering behavior typically observed in other 2D materials, WSe_2 exhibits a completely different pattern. In this material, there is no discernible dominance of normal scattering processes over Umklapp processes across the entire temperature range. This phenomenon may stem from the considerable atomic mass of both W and Se atoms compared to those in other materials. Umklapp processes in WSe_2 are not suppressed to the extent they are in lighter 2D materials, thus altering the balance between the two scattering mechanisms. This could be a consequence of increased anharmonicity by heavier atoms, thereby facilitating Umklapp scattering.

Moreover, despite the substantial variety of isotopes in W and Se, WSe_2 demonstrates relatively lower phonon-isotope scattering than MoS_2. This indicates that phonon-isotope scattering is influenced not only by the natural abundance of isotopes but also by the mass variance among them. For instance, Mo atoms span a mass variance of up to 8 atomic mass units across their stable isotopes, while W isotopes, exhibiting a range in mass numbers from 180 to 186, may not introduce the same level of scattering.

The research into the phonon scattering mechanisms within WSe_2 at varying temperatures reveals a gap in our understanding, particularly regarding the temperature-dependent behavior of phonon interactions. These gaps underscore the necessity for targeted studies on the influence of thermal effects on phonon lifetimes and transport in heavier 2D materials. Such in-depth analysis could provide a robust theoretical framework for future research to explore the peculiarities of phonon dynamics in these materials.

In summary, Figure 4.10 (a) to (d) elucidate the complex interplay between scattering mechanisms and temperature, underscoring the distinctiveness of 2D materials. It is crucial to note that these scattering rates represent average values, offering insights into the relative contributions of each scattering mechanism rather than serving as absolute measures.

4.1.2 Comparison with experimental data for 2D material thermal conductivities

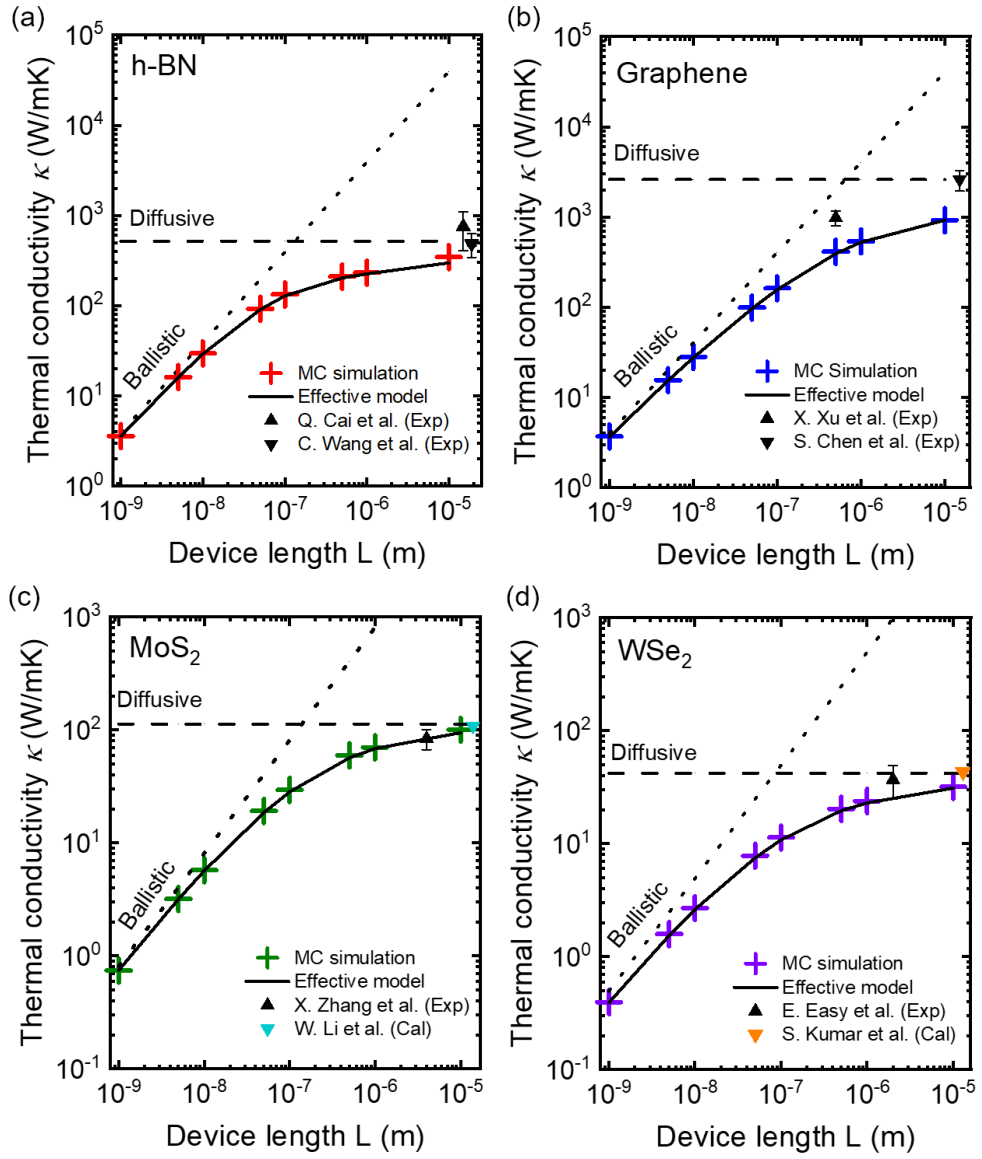

Figure 4.11 Thermal conductivities of (a) h-BN, (b) Graphene, (c) MoS_2, and (d) WSe_2 nanofilms as a function of device length. Data points include Monte Carlo simulations (crosses), effective model (lines), and experimental results (triangles) [66,86,87,97,98,104,284,285]

In Section 4.1.1, we obtained the phonon properties of various 2D materials necessary for Monte Carlo (MC) simulations through DFT calculations. In this section, the accuracy of the DFT data is validated by examining the length-dependent thermal conductivity of h-BN, graphene, MoS_2, and WSe_2 nanofilms at room temperature. The results are also compared against experimental measurements and theoretical values from other references, as illustrated in Figure 4.11.

For these analyses, we utilize the device type depicted in Figure 3.4 (a), which is a nanofilm in a cross-plane configuration (CPNF) in MC simulation. It's important to note that the unit cell volume of the 2D materials is normalized to a reference volume, typically the volume of a corresponding unit cell in the bulk crystal structure. The thickness in the perpendicular direction is chosen based on the experimental thickness of the corresponding bulk material, utilizing c/a ratios of 1.317 for h-BN, 1.367 for graphene, 1.945 for MoS_2, and 1.962 for WSe_2 [69,271]. The symbol 'c' refers to the interlayer spacing in bulk materials, with h-BN having an interlayer spacing of 3.298 Å, graphene with 3.333 Å, MoS_2 with 6.201 Å, and WSe_2 with 6.508 Å. These calculations exclude the vacuum space between periodic repetitions of the 2D slab.

In Figure 4.11 (a), the MC results for h-BN, indicated by red crosses, show a trend converging towards the ballistic model (dotted line) for shorter device lengths where phonons are less likely to scatter, resulting in ballistic transport. As the device length increases, the calculated thermal conductivities approach the diffusive limit (dashed line), exhibiting asymptotic behavior. The effective model (solid line) aligns with the MC results across all device lengths, thereby demonstrating its applicability to 2D device systems as well. At a device length of 10 μm, the thermal conductivity values are in agreement with the experimental measurements for monolayer (triangle) [87] and bilayer (inverted triangle) h-BN [86], within the margin of error.

In Figure 4.11 (b), a discrepancy between MC simulation results for graphene, depicted by blue crosses, and the experimental values represented by triangles is observed. At a device length of 500 nm, our MC result yields a thermal conductivity of 411 W/mK, whereas the

experimental result shows a much higher value of 981 ± 184 W/mK [66]. Even though the calculated thermal conductivity at the diffusive limit is 2603 W/mK, which agrees with the experimental result of 2600 ± 658 W/mK [284], it still diverges from the MC results for longer devices. This divergence can be attributed to the use of the implementation of the scattering using a relaxation time approximation (RTA), in which phonons return to equilibrium at an average rate in solving the Boltzmann transport equation (BTE) within our MC simulations [188,206], as detailed in Section 2.2.1.

As illustrated in Figure 4.10, normal processes are typically dominant over Umklapp processes in 2D materials, and this is particularly pronounced in graphene. The RTA assumes that each scattering events contribute to relaxation towards equilibrium, but N processes do not directly contribute to thermal resistance. Instead, they redistribute the out-of-equilibrium phonon population [69]. Therefore, the RTA usually does not capture this redistribution accurately. To overcome the limitations of the RTA, alternative methods such as the iterative solutions to the BTE or the implementation of Callaway's model are often employed for such 2D systems [68,69,202].

For MoS_2 nanofilms, despite concerns regarding the limitations of RTA in 2D systems, the MC simulation results (green crosses) agree perfectly with experimental data (triangle) [97]. With a nanofilm length of 10 µm, our result closely approaches the diffusive value of 112 W/mK, displaying remarkable accuracy compared to the theoretical calculations of 108 W/mK (sky blue triangle) from other studies [98], as depicted in Figure 4.11 (c). Furthermore, in Figure 4.11 (d), the results for WSe_2 (purple crosses) also match the experimental data (triangle) [285] within the margin of error. Similarly, the diffusive value of the theoretical limit calculated using our DFT data coincides almost perfectly with other theoretical calculations (orange triangle) from the literature [104].

Although the RTA may fall short, especially in graphene, where normal processes are extremely dominant, our model still demonstrates overall reliability, as shown by the close agreement with experimental measurements. The alignment of our long-device thermal conductivity results with theoretical predictions confirms the accuracy of calculated

DFT data, underscoring the robustness of our simulation methods. Consequently, our findings provide a trustworthy foundation for exploring heterostructures based on 2D materials in the next section.

4.2 LATERAL HETEROSTRUCTURE BASED ON 2D MATERIALS

4.2.1 2D h-BN/Graphene lateral heterostructure

4.2.1.1 Device geometry

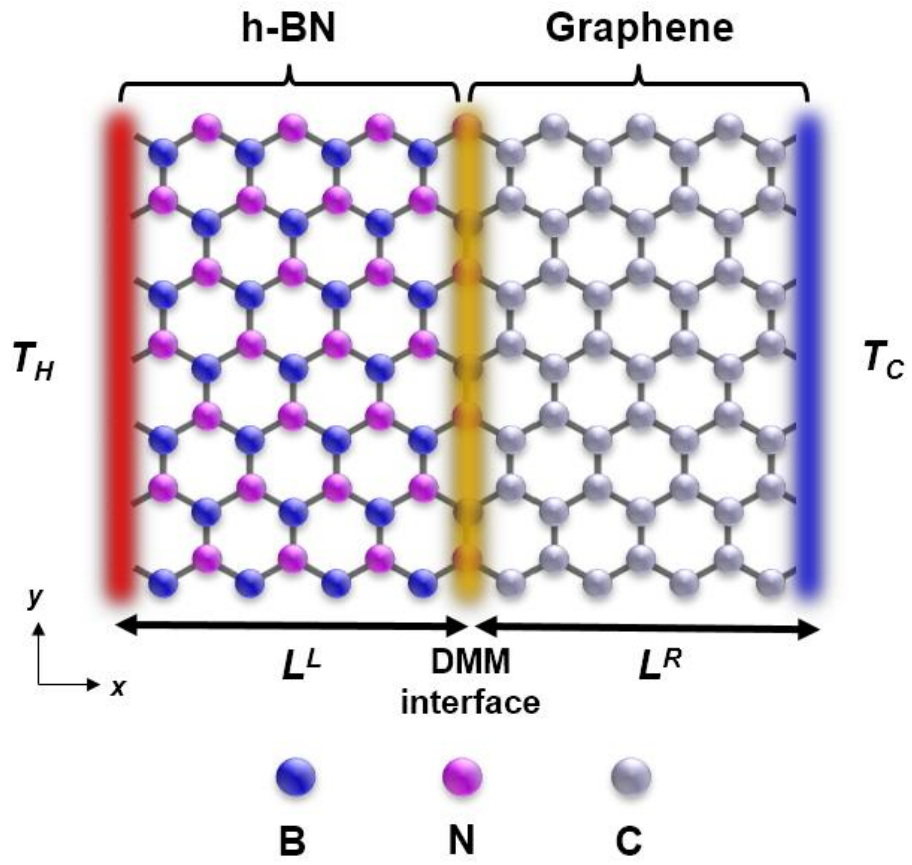

Figure 4.12 Sketch of the simulated h-BN/graphene lateral heterostructure. Red/blue faces for hot/cold thermostats with T_H = 302 K, T_C = 298 K, respectively. Yellow zone indicates the DMM interface.

Figure 4.12 shows the investigated h-BN/graphene lateral heterostructure, illustrating the top view of the in-plane nanostructures. The red and blue regions indicate hot and cold thermostats set at 302 K and 298 K, respectively, positioned on opposite ends of the structure. Given their arrangement with the hot thermostat on the left and the cold one on the right, the thermal flux is naturally oriented to flow in the positive x-direction. The structures are assumed to extend infinitely in the y-direction by applying periodic boundary conditions, thereby eliminating edge effects from the analysis.

The lengths of the h-BN and graphene regions are denoted as L^L and L^R, respectively, and their sum constitutes the total device length L. The central yellow zone represents the diffusive interface, which is situated at the central region of the structure by employing the diffuse mismatch model (DMM) [232,235]. Regardless of variations in the device length L, the defined DMM interface is consistently placed at the midpoint between the two materials ($x = L/2$) to facilitate the study of the interface thermal conductance. A finite rectangular mesh, consisting of cells of lengths no greater than 1 nm, is employed in our MC simulator along the x-axis for the numerical evaluation of the thermal characteristics of the devices.

4.2.1.2 Calculation of the interface thermal conductance

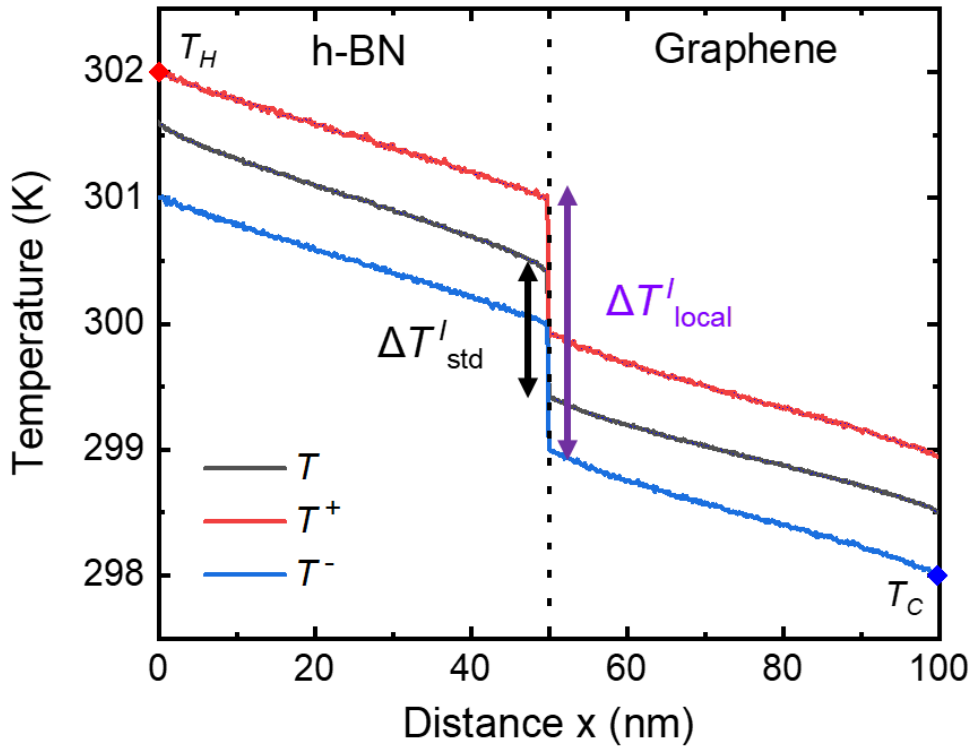

Figure 4.13 Calculated temperature profiles of T (black), T^+ (red) and T^- (blue) for a length h-BN/graphene heterostructure with L = 100 nm. Red and blue diamonds show the temperature of the hot and cold thermostats, respectively.

In lateral heterostructures, measuring the temperature in each material region and quantifying the interface thermal conductance (ITC) at the junction between the two materials is important for developing devices with optimal performance and advancing the understanding of thermal phenomena. The ITC, which is computed by dividing the heat flux density by the difference in the temperatures on each side of the interface, reflects the efficiency of heat transfer from one material to another [239].

As discussed in the Section 2.2.3, defining temperature within the simulation is critical for correctly determining the ITC. The standard

temperature T assuming an equilibrium state based on Bose-Einstein statistics may not be suitable for describing heat transfer in heterostructures. Therefore, we utilize the concept of directional temperature (T^+ and T^-), defined from the energy density associated with the phonon sub-populations possessing positive and negative velocities, respectively. This approach enables us to compute accurately the ITC by capturing the anisotropic nature of heat flow within these structures [238,239].

Figure 4.13 displays the calculated temperature profiles of the standard temperature T (black), as well as the directional temperatures T^+ (red) and T^- (blue) in a 100 nm h-BN/graphene heterostructure, composed of 50 nm lengths of both h-BN and graphene. In the heterostructure depicted in Figure 4.12, the h-BN is in contact with the hot thermostat, while the graphene touches the cold thermostat.

At each contact point, the standard temperature shows discrepancies with the hot and cold thermostats, represented by red and blue diamonds. However, the directional temperatures maintain continuity near the respective hot and cold thermostats. If there is no temperature bias, all temperatures would align ($T^+ = T^- = T$) at equilibrium. At the interface, a distinct temperature drop is observed, indicating a significant thermal gradient. Depending on the selected temperature definitions, there are two different temperature drop at interface [239].

$$\Delta T^I_{\mathrm{std}} = T(x-\epsilon) - T(x+\epsilon) \tag{4.2}$$

$$\Delta T^I_{\mathrm{local}} = T^+(x-\epsilon) - T^-(x+\epsilon) \tag{4.3}$$

where ϵ represents an infinitesimally short distance, for the purposes of numerical measurement, it is set to 2 Å.

Thus, these two quantities lead to the different ITC values as depicted in Figure 4.14. Using the standard temperature difference $\Delta T^I_{\mathrm{std}}$ (black crosses), the ITC results are consistently double those calculated using directional temperatures $\Delta T^I_{\mathrm{local}}$ (purple crosses) across all device lengths. The results based $\Delta T^I_{\mathrm{local}}$ are well matched with analytical model [239] (dotted line) because of the advantage of directional

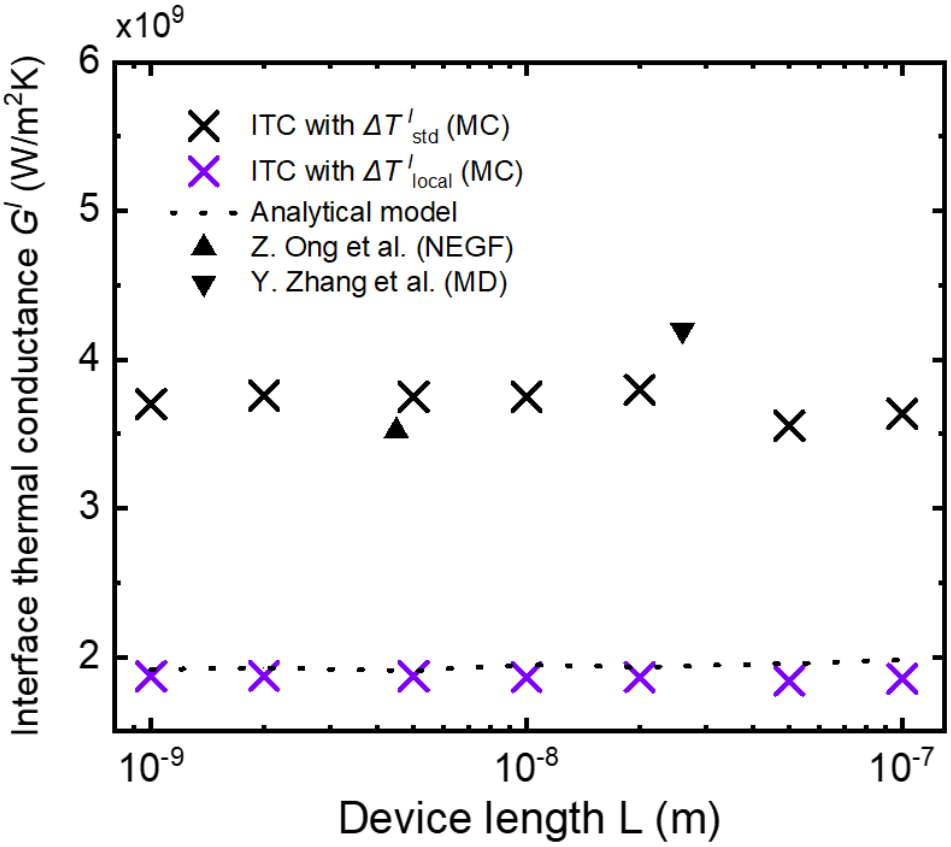

Figure 4.14 Comparison of interface thermal conductance (ITC) calculated using the standard temperature difference (black crosses) and the directional temperatures (purple crosses) as a function of the device length. The analytical model is represented by the dotted line, while results from other studies employing NEGF [286] *and MD* [287] *methods are indicated with triangles for comparison.*

temperatures in capturing the behavior of phonons that actually interact with the interface. When compared with results from the non-equilibrium Green's function (NEGF) method [286] and molecular dynamics simulation [287], those results using the $\Delta T^I_{\mathrm{std}}$ for the ITC calculation show similarly results far from the analytical model and our MC results employed $\Delta T^I_{\mathrm{local}}$.

Previous studies have confirmed that MC simulations with directional temperatures accurately estimate the ITC in bulk materials such as silicon and germanium [240,241]. Our study extends this validation to

the ITC prediction between 2D materials, reinforcing the method's applicability in these novel structures.

4.2.1.3 Evolution of phonon modal contribution near the interface

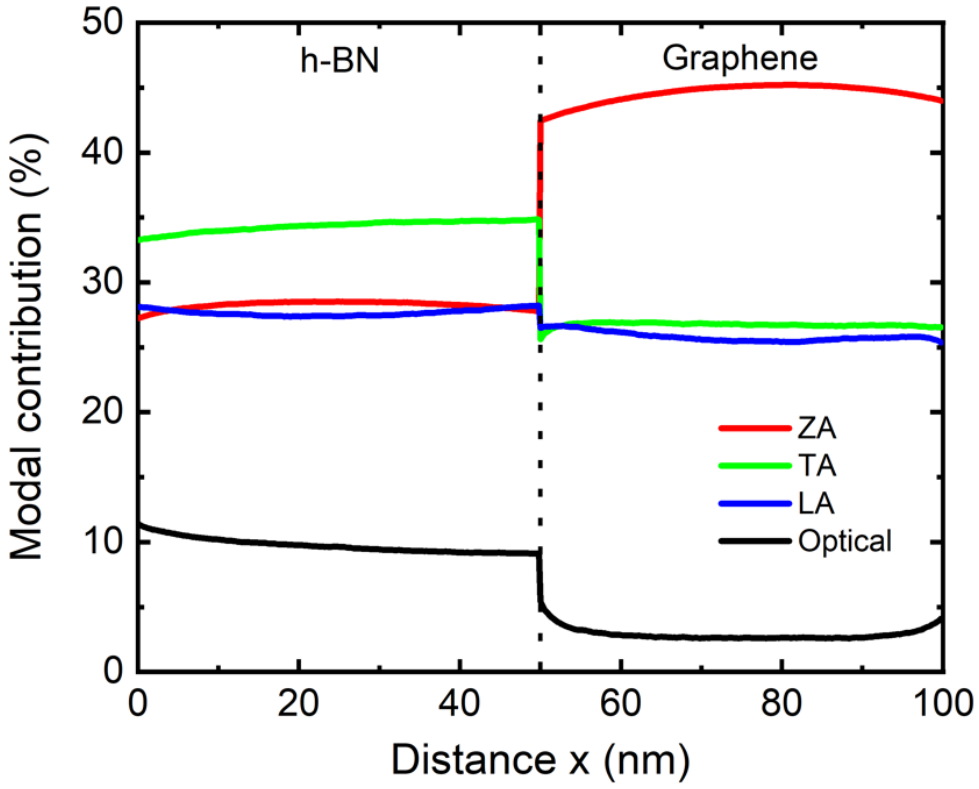

Figure 4.15 Modal contributions of phonon modes to the total heat flux density in a 100 nm long h-BN/graphene heterostructure.

To further investigate the phenomena occurring near the interface, we calculate the modal contribution of the each phonon modes to the total heat flux density along the *x*-axis in a 100 nm long h-BN/graphene lateral heterostructure, as shown in Figure 4.15. The contributions of all modes at each position sum up to 100 percent, in line with the conservation of total heat flux. In both material regions, the contribution of optical modes is obviously small compared to acoustic modes. Remarkably, the ZA mode contributes over 40 % to

the heat flux density in graphene, playing a more significant role than in the h-BN area. This is because the low atomic mass and high strength of the carbon-carbon bonds allow for more pronounced flexural movements, leading to a larger contribution from ZA modes to thermal transport.

A key point in this figure is that the phonon modes are significantly perturbed upon traversing the DMM interface, exhibiting a distinct curvature. This behavior indicates a strong non-equilibrium transport regime within a few nanometers of the interface. Consequently, the adoption of a standard temperature assuming equilibrium exhibits clear limitations due to the pronounced non-equilibrium region around the interface. Therefore, the adoption of directional temperatures instead of standard temperatures offers a more accurate representation of these non-equilibrium conditions, thus facilitating a precise calculation of the ITC for lateral heterostructures with interfaces.

4.2.1.4 *Effect of diffusive interface between 2D materials compared to homogeneous 2D nanofilm*

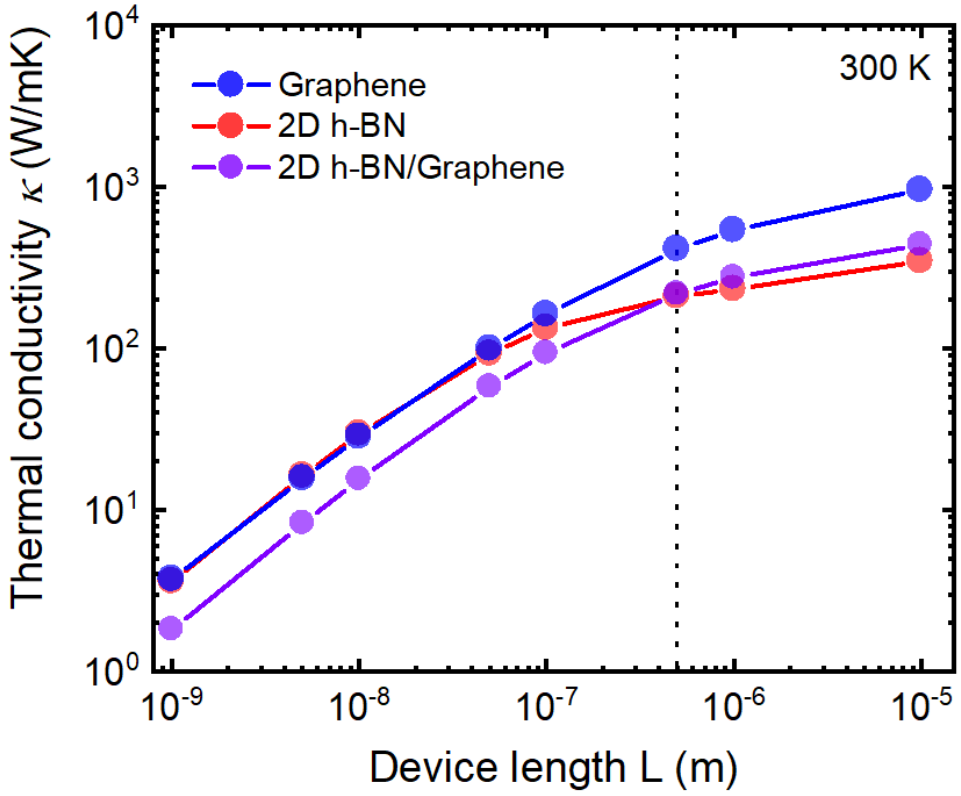

Figure 4.16 Comparison of thermal conductivity as a function of device length for h-BN nanofilms (red line), graphene nanofilms (blue line), and their combined h-BN/graphene heterostructure (purple line) at 300 K. The conductivities for h-BN and graphene are based on the MC results from Figure 4.11 (a) and (b).

Figure 4.16 presents the thermal conductivity for h-BN (red), graphene (blue) nanofilms, and the h-BN/graphene heterostructure (purple) as a function of device length. The data for h-BN and graphene nanofilms are extracted from the MC results, previously presented in Figure 4.11 (a) and (b), respectively. This side-by-side comparison sheds light on the role of interfaces within the heterostructure and their effect on thermal transport.

The calculated results of the h-BN/Graphene lateral heterostructure exhibits an intriguing dependency on the device length. For device lengths below approximately 500 nm, the thermal conductivity of the heterostructure is reduced relative to that of homogeneous h-BN and graphene nanofilms, due to phonon scattering at the interface between the two materials. However, as the device length increases beyond 500 nm, the thermal conductivity of the heterostructure begins to surpass that of homogeneous h-BN nanofilm, while still remaining below the thermal conductivity of graphene. This indicates a diminishing influence of the interface on thermal resistance with increased length, allowing the inherently high thermal conductivity of graphene to progressively dominate within the heterostructure.

4.2.2 2D MoS_2/WSe_2 lateral heterostructure

4.2.2.1 Device geometry

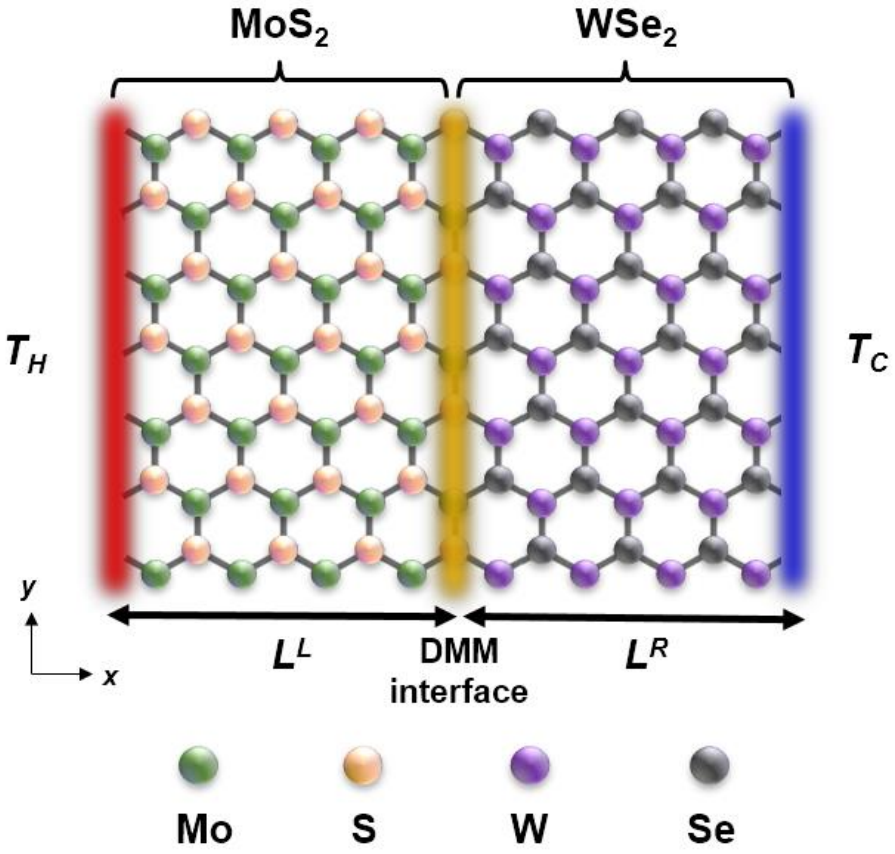

Figure 4.17 Sketch of the simulated MoS_2/WSe_2 lateral heterostructure. Red/blue faces for hot/cold thermostats with T_H = 302 K, T_C = 298 K, respectively. Yellow zone indicates the DMM interface.

Figure 4.17 illustrates a 2D MoS_2/WSe_2 lateral heterostructure, which closely mirrors the design of the 2D h-BN/graphene heterostructure depicted in Figure 4.12. To distinguish between the two different materials within this heterostructure, each atom is color-coded: Mo atoms are in green, S atoms in yellow, W atoms in purple, and Se atoms in gray. MoS_2 is positioned on the left in contact with the hot thermostat and WSe_2 is situated on the right adjoining the cold thermostat. Aside from this, the setup maintains the same conditions as the previously mentioned 2D h-BN/graphene heterostructure.

4.2.2.2 Calculation of the interface thermal conductance

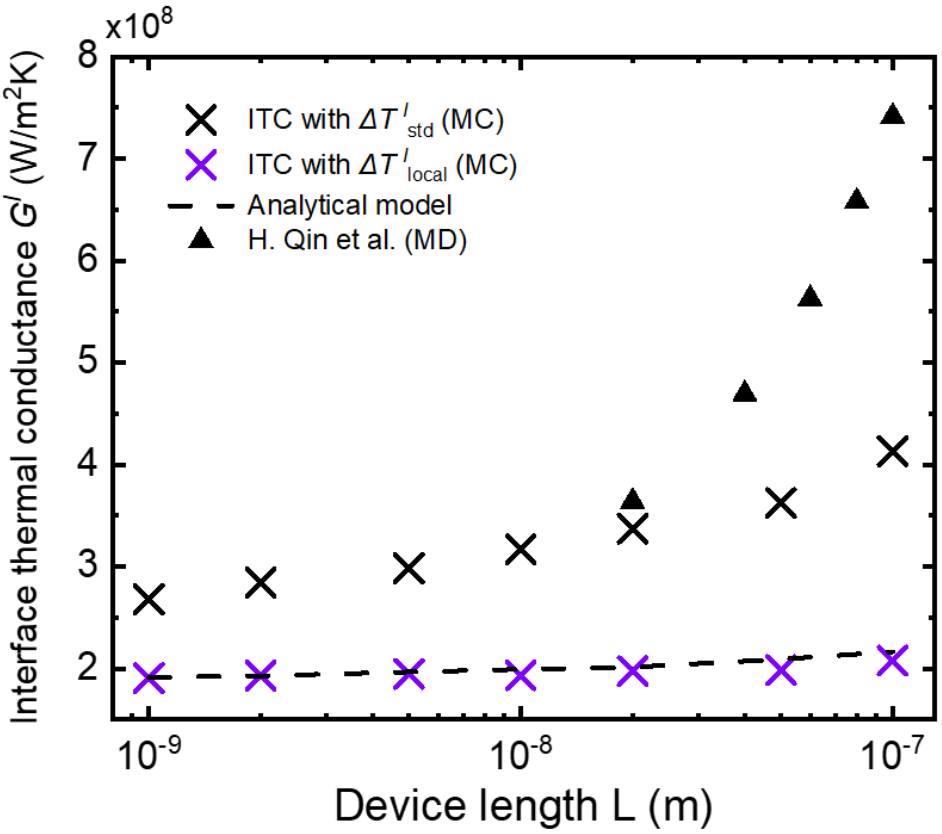

Figure 4.18 Comparison of interface thermal conductance (ITC) calculated using the standard temperature difference (black crosses) and the directional temperatures (purple crosses) as a function of the device length. For comparative purposes, the analytical mode and results from other studies employing MD method [126] *are indicated with the dotted line and triangle, respectively.*

Similar to the analysis in Section 4.2.1, Figure 4.18 presents the interface thermal conductance (ITC) results calculated across various device lengths for a MoS_2/WSe_2 lateral heterostructure. ITC calculations based on standard temperature differences (black crosses) show excessive values and an unexpected length-dependent trend, deviating from analytical predictions (dashed line). This phenomenon is also reflected in results obtained using molecular dynamics (MD) methods (triangles) from other studies [126], which show an even more

pronounced length-dependence.

On the other hand, directional temperature-based calculations (purple crosses) demonstrate length-independent ITC, in agreement with theoretical expectations. The work from Z. Liang et al. also highlighted that introducing an extremely rough interface leads to a size-independent interface thermal resistance [288], which is analogous to our findings. The standard temperature oversimplifies the complex phonon interactions at the interface, whereas directional temperatures provide an advanced approach that captures the thermal properties in a non-equilibrium system, leading to more accurate ITC calculations.

4.2.2.3 Unexpected length dependence on ITC

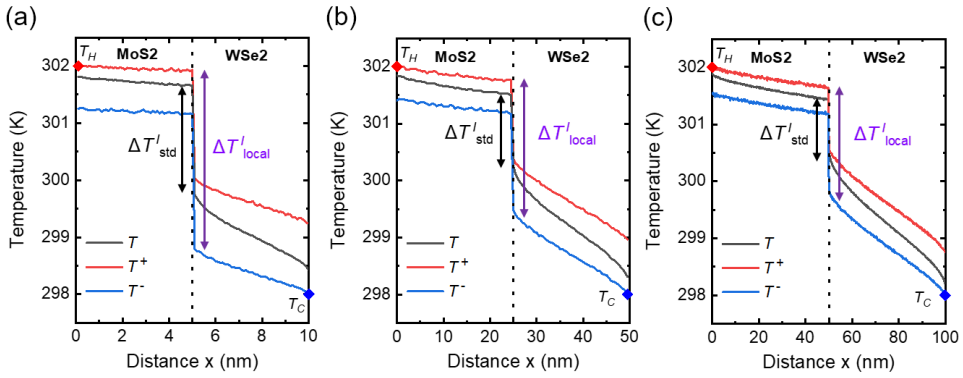

Figure 4.19 Temperature profiles of T (black), T^+ (red) and T^- (blue) for MoS_2/WSe_2 heterostructures of varying lengths: (a) 10 nm, (b) 50 nm, and (c) 100 nm. Red and blue diamonds show the temperature of the hot and cold thermostats, respectively.

To investigate the unexpected length dependence of the ITC calculated using the standard temperature, the temperature profiles are calculated for MoS_2/WSe_2 heterostructures of lengths 10 nm, 50 nm, and 100 nm, as shown in Figure 4.19 (a), (b), and (c), respectively. As with Figure 4.13, the profiles include the standard temperature T in black, alongside directional temperatures T^+ in red and T^- in blue.

In panel (a), the device with a length of 10 nm exhibits nearly flat temperature profiles which are attributed to phonons moving in a ballistic regime due to the very short length, allowing the temperature of the thermostat to be transmitted almost directly. As the device length increases, the internal temperature gradient becomes steeper, leading to a reduction in the temperature jumps ($\Delta T^I_{\mathrm{std}}$ and $\Delta T^I_{\mathrm{local}}$) at the interface.

With the extension of the device length, the curvatures of the standard temperature near the interface are notably observed, contrasting the more consistent profiles of the directional temperatures. This curvature indicates a deviation from equilibrium, particularly near the diffusive interface, where non-equilibrium conditions are expected to prevail. This leads the standard temperature, which assumes equilibrium, to exhibit this anomalous behavior.

In a heterostructure, the diffusive interface between two materials, defined by the DMM, is significantly influenced by the lattice constants of these materials, affecting the efficiency of phonon transmission across the interface [235]. For instance, in the h-BN/graphene lateral heterostructure, the relatively low lattice mismatch of approximately 2.7 % results in less pronounced effects on the ITC, not exhibiting significant length dependence when calculated using the standard temperature.

However, in the MoS_2/WSe_2 heterostructure, the larger lattice mismatch of around 3.9 % leads to more substantial impacts on the ITC. This mismatch contributes to increased phonon scattering at the interface, manifesting as a notable length-dependent behavior in the ITC when calculated using standard temperature. In conclusion, a substantial mismatch can increase phonon scattering and lead to non-equilibrium conditions, which can be more accurately captured by using directional temperatures instead of assuming a standard temperature across the interface.

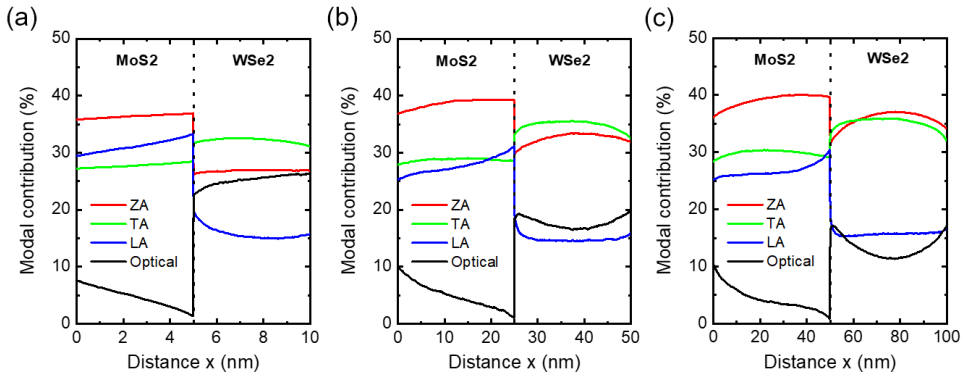

Figure 4.20 Modal contributions of phonon modes to the total heat flux density in MoS_2/WSe_2 heterostructures for device lengths of (a) 10 nm, (b) 50 nm, and (c) 100 nm.

Lastly, Figure 4.20 provides the modal contributions of various phonon modes within MoS_2/WSe_2 heterostructures with varying lengths of 10 nm, 50 nm, and 100 nm to analyze the phenomenon occurring near this interface in more detail. Similar to the h-BN/graphene heterostructure in Figure 4.15, phonon modes exhibit significant perturbation when traversing the DMM interface in the MoS_2/WSe_2 heterostructure.

Regardless of the device length, the substantial contribution from the ZA mode is consistent due to their enhanced role in 2D structures. A noteworthy observation is the increasing curvature of the modal contributions as the length of the heterostructure expands. In panel (a), representing the length of 10 nm, the variations in modal contribution are relatively flat. In contrast, panel (c) for the 100 nm device exhibits much more pronounced curvature, notably near the interface.

The enhanced curvature observed in longer heterostructures suggests the system is far from the equilibrium regime, particularly near the interface where non-equilibrium conditions are more pronounced. This trend agrees with the temperature profile analysis previously detailed in Figure 4.19.

4.3 SUMMARY

This chapter presented an in-depth analysis of thermal transport in 2D materials (h-BN, graphene, MoS_2, and WSe_2) and their lateral heterostructures. In DFT calculations, the accuracy of the results is evidenced by the good agreement between calculated phonon dispersion and experimental data, avoiding the issue of unphysical negative frequencies. A significant advancement presented in the chapter is the detailed cartographic representation of phonon group velocities and scattering rates for 2D materials. It reveals distinct non-isotropic characteristics, underscoring the importance of employing a full-band description of the Brillouin Zone.

Through the analysis of average phonon scattering rates, we found that normal scattering dominates over Umklapp scattering at all temperatures for these 2D materials. Moreover, substantial isotope mixtures in h-BN and MoS_2 result in strong phonon-isotope scattering comparable to phonon-phonon scattering at 300 K. The reliability of our simulation methodology is validated by calculating the thermal conductivity, which is closely aligned with experimental measurements. While slight discrepancies are observed in graphene, where normal processes are highly dominant, the overall accuracy is commendable.

In the study of the lateral heterostructures, it is shown that the standard temperature, based on Bose-Einstein statistics, falls short in accurately describing heat transfer within these heterostructures. Since phonons are notably perturbed near the interface, where a strong non-equilibrium transport regime is observed, the standard temperature fails to effectively capture the behavior of phonons at the interface. To address this, we introduced the concept of directional temperatures, which enable the precise computation of the ITC. Notably, results obtained using directional temperatures show a strong match with the analytical model and do not exhibit the length-dependent variations seen with standard temperature calculations.

Overall, the results of Chapter 4 contribute to the fundamental understanding of thermal transport in 2D materials, particularly in lateral heterostructures, providing key insights for developing efficient thermal management strategies in nano-devices.

5 TRANSIENT THERMAL RESPONSE IN 100 NM 2D H-BN/GRAPHENE HETEROSTRUCTURE

Chapter 5 presents a comprehensive study of the transient thermal response in 100 nm 2D h-BN/graphene lateral heterostructures. Utilizing advanced Monte Carlo (MC) simulation based on ab-initio calculations for phonons, this study focuses on understanding the heat transfer mechanisms in transient regime with picoseconds (ps) time scale beyond the steady-state regime as discussed in Chapter 4.

Section 5.1.1 shows positional mapping at various positions within the investigated heterostructure to analyze how transient thermal properties manifest spatially. It initially explores the unique material properties of h-BN and graphene relevant to transient thermal analysis, such as volumetric heat capacity and ballistic thermal conductance (5.1.2). Next, Section 5.2 discusses the changes in heat flux density and temperature over time (5.2.1), introduces a semi-analytical model for transient response based on directional temperatures (5.2.2), and then calculations of relaxation, delay, and rise times are provided to characterize the temporal response (5.2.3). Furthermore, the study presents the contributions of different phonon modes to the heat flux density (5.3.1) and quantifies mode-dependent thermal behaviors in detail (5.3.2). At last, Section 5.4 examines how interfaces within the heterostructures influence the transient thermal response by comparing homogeneous h-BN and graphene nanofilms without interface, thus revealing interface effects. This analysis provides valuable insights for understanding thermal dynamics in heterostructures, emphasizing the complex interplay between material properties and transient thermal processes.

5.1 INTRODUCTION

5.1.1 Positional mapping in 100 nm h-BN/graphene heterostructure

In Chapters 3 and 4, the analysis predominantly focused on the system's steady-state dynamics, reached when its response to thermal stimuli stabilizes and no further temporal changes are observed in its thermal properties. Determining this steady-state is pivotal as thermal properties such as thermal conductivity and interface thermal conductance are calculated in these conditions. However, as devices are miniaturized to the nanometer scale, power density increases, which can cause localized heating during operation [2,289]. This transient response between the initial behavior by an external bias and the steady-state can lead to rapid temperature changes [290]. Such a miniaturization results in important challenges for effective thermal management to prevent overheating and ensure device reliability. High-temperature fluctuations in nanoscale devices may induce device malfunction, which has driven research toward developing advanced thermal interfaces and cooling technologies [291–293]. Therefore, understanding the transient response is essential for accurate device performance predictions.

This chapter explores the thermal transient response of the monolayer h-BN/graphene lateral heterostructure by measuring thermal properties at six different positions in 0.1 ps increments. Figure 5.1 presents the 100 nm 2D h-BN/graphene heterostructure maintaining the same structural configuration illustrated in Figure 4.12. To closely replicate the transient high-temperature conditions encountered in operational devices, the cold thermostat is set at 300 K. The hot thermostat is then instantaneously switched from 300 K to 400 K at t=0 s.

The investigation strategically targets regions adjacent to the thermostats, the central areas, and the interfaces of each material: three in the h-BN region (positions A to C) and three in the graphene region (positions D to F). Position A (x = 2 nm) is located at the extreme edge adjacent to the hot thermostat to examine thermal effects originating from the heat source within the device. Position B (25 nm) is centered within the h-BN section, allowing for observing the

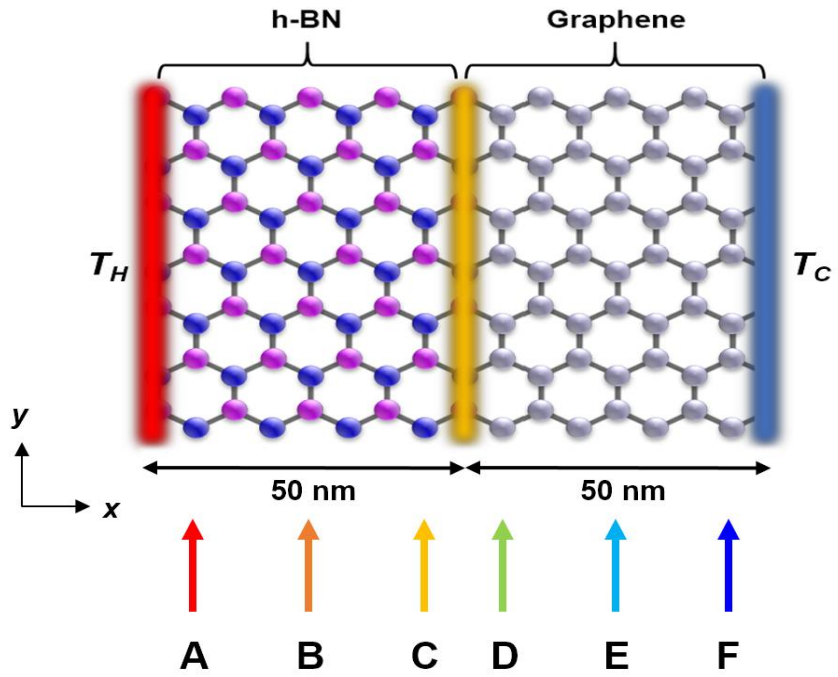

Figure 5.1 Sketch of the simulated 100 nm h-BN/graphene lateral heterostructure with specific positions (A to F) marked for thermal transient analysis. Positions A, B, C, D, E, and F are located at 2, 25, 48, 52, 75, and 98 nm, respectively, along the x-axis within the structure. Red/blue faces for hot/cold thermostats with T_H = 400 K, T_C = 300 K, respectively. Yellow zone indicates the DMM interface.

material's intrinsic thermal transient response. Position C (48 nm) resides near the h-BN/graphene interface, providing insight into the interface effects. Similarly, positions D (52 nm), E (75 nm), and F (98 nm) offer a mirrored arrangement in the graphene region. This mapping facilitates a comprehensive spatial analysis of how transient thermal behavior manifests across the heterostructure.

Moreover, the choice of the 100 nm length scale is particularly significant due to the non-trivial interplay between ballistic and diffusive transport regimes at this scale [294]. Investigating these regimes at the nanoscale not only offers valuable insights into their complicated thermal behaviors, but also guides the development of more effective thermal management strategies.

5.1.2 Key material properties in transient thermal analysis

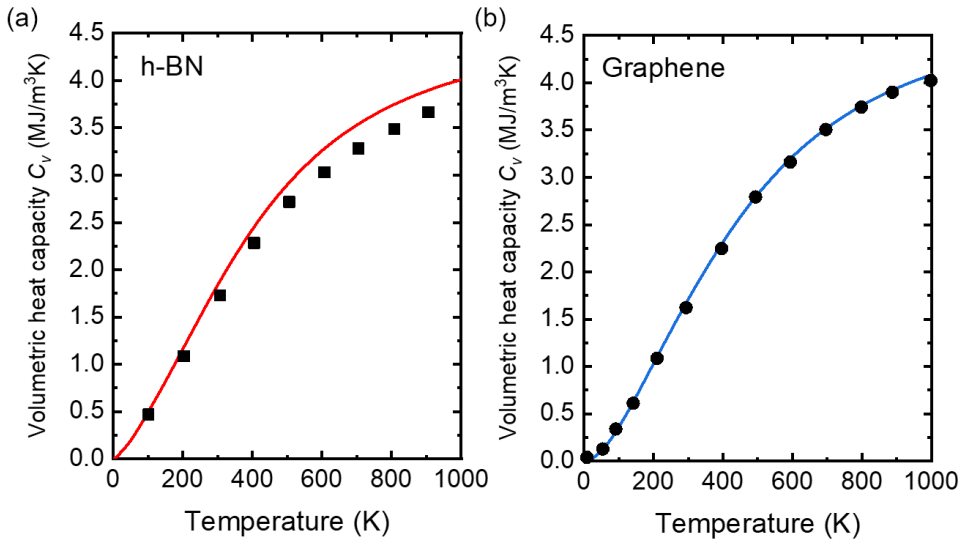

Figure 5.2 The calculated volumeteric heat capacity of (a) h-BN and (b) graphene at various temperatures. Black squares and circles present experimental data on bulk h-BN [296,297] *and graphene* [298].

Understanding the intrinsic material characteristics of heat transfer and storage is crucial for studying transient thermal response. The first fundamental property in transient thermal analysis is the volumetric heat capacity C_V since it is defined as the amount of heat energy required to raise the temperature of a unit volume of a material by dictating how a material reacts to temporal changes in heat [295]. The volumetric heat capacity can be calculated as follows:

$$C_V(T) = \frac{\Omega}{(2\pi)^3} \sum_s \hbar\omega_s \frac{\partial f_{BE,s}}{\partial T}(\omega_s, T) \tag{5.1}$$

where Ω is the volume of the reciprocal space, $\hbar\omega_s$ is the phonon energy in a state s, and $\frac{\partial f_{BE,s}}{\partial T}$ is the temperature derivative of the Bose-Einstein distribution function at temperature T.

Figure 5.2 shows the calculated volumetric heat capacity C_V of (a) 2D h-BN and (b) graphene across temperatures ranging from 0.1 K to

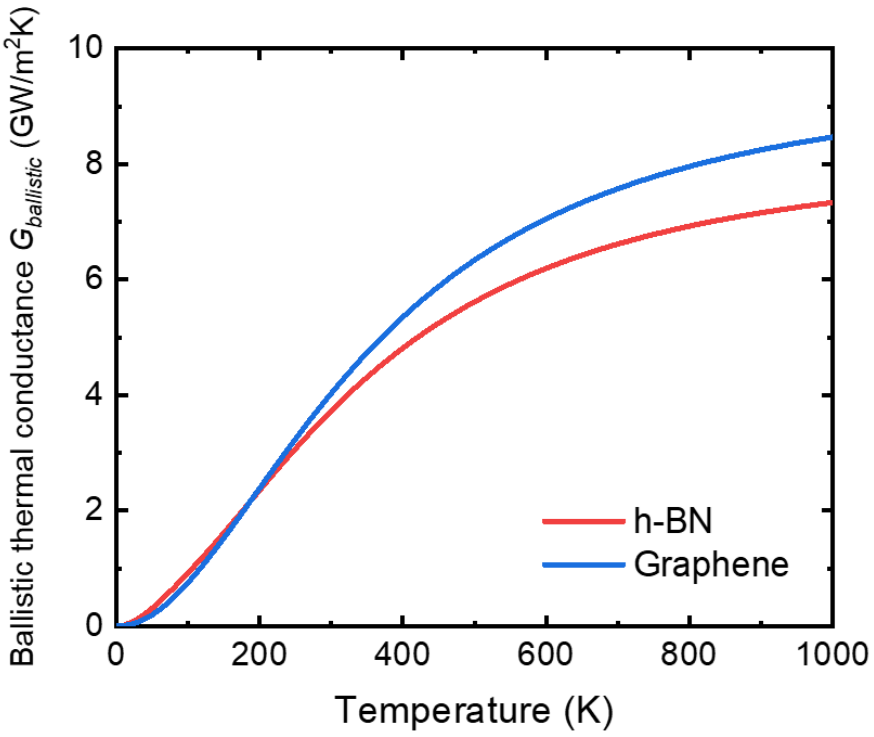

Figure 5.3 The calculated Ballistic thermal conductance of (a) h-BN (red line) and (b) graphene (blue line) as a function of temperature.

1000 K compared to experimental data [296–298]. The curves (in units of MJ/m^{3}K) increase with temperature, representing values of 1.84 MJ/m^{3}K for h-BN and 1.71 MJ/m^{3}K for graphene at 300 K. In Figure 5.2 (a), a slight discrepancy at higher temperatures for h-BN is observed, which can be attributed to the experimental data being for bulk h-BN, not monolayer h-BN. The close match between the calculated curves and the experimental data points around room temperature emphasizes the accuracy of the DFT-based material information for these two-dimensional materials.

Despite the notable differences in thermal conductivities of h-BN and graphene, observed in Chapter 4, their volumetric heat capacities are quite similar and of the same order of magnitude. The heat capacity relies on the phonon density of states, which is influenced by the

atomic arrangement. Since both h-BN and graphene have identical two-dimensional honeycomb lattice structures, this accounts for their similar heat capacities.

Like the volumetric heat capacity C_V, the ballistic thermal conductance $G_{ballistic}$ is also an important material property in transient thermal analysis because it describes how quickly heat can be transferred within a material without phonon scattering [299]. This is particularly relevant in a system like the 100 nm h-BN/graphene lateral heterostructure, where the physical sizes are comparable to the mean free path of phonons facilitating ballistic transport.

The ballistic thermal conductance is computed as [239]:

$$G_{ballistic} = \frac{\Omega}{(2\pi)^3}\frac{1}{2}\sum_{s}\hbar\omega_s|\overrightarrow{v_s}\cdot\vec{n}|\frac{\partial f_{BE,s}}{\partial T}(\omega_s, T) \qquad (5.2)$$

where $|\overrightarrow{v_s}\cdot\vec{n}|$ is the magnitude of the group velocity along the transport direction. Note that this is size-independent, unlike the ballistic conductivity derived in equation 2.37 of Chapter 2.

Figure 5.3 displays the temperature dependence of the ballistic thermal conductance for h-BN and graphene, represented by the red and blue lines respectively. At 300 K, the result of h-BN is 3.73 GW/m²K and that of graphene is 4.03 GW/m²K, with graphene exhibiting a higher value as anticipated. The discrepancy between the ballistic thermal conductance of these two materials becomes larger as the temperature rises.

Building upon the two material properties defined for h-BN and graphene, we can calculate the characteristic time for homogeneous nanofilms using a lumped thermal capacity model [300], which is the simplest transient heat conduction approach. The characteristic time is calculated by dividing the volumetric heat capacity by the thermal conductance and then multiplying by a given length. For instance, the estimated characteristic time for heat to diffuse to a length of 98 nm, corresponding to position F in Figure 5.1, is 48.2 ps for h-BN and 41.6 ps for graphene, respectively. These estimations will be compared with the results of numerical Monte Carlo simulations in the subsequent

Section 5.4.

In the following section, we will examine the transient thermal response of the designed system in various aspects, where an understanding of the volumetric heat capacity and ballistic thermal conductance of each material will be instrumental in this analysis.

5.2 SPATIAL VARIATION OF TRANSIENT THERMAL RESPONSE

5.2.1 Heat flux density and temperature evolution

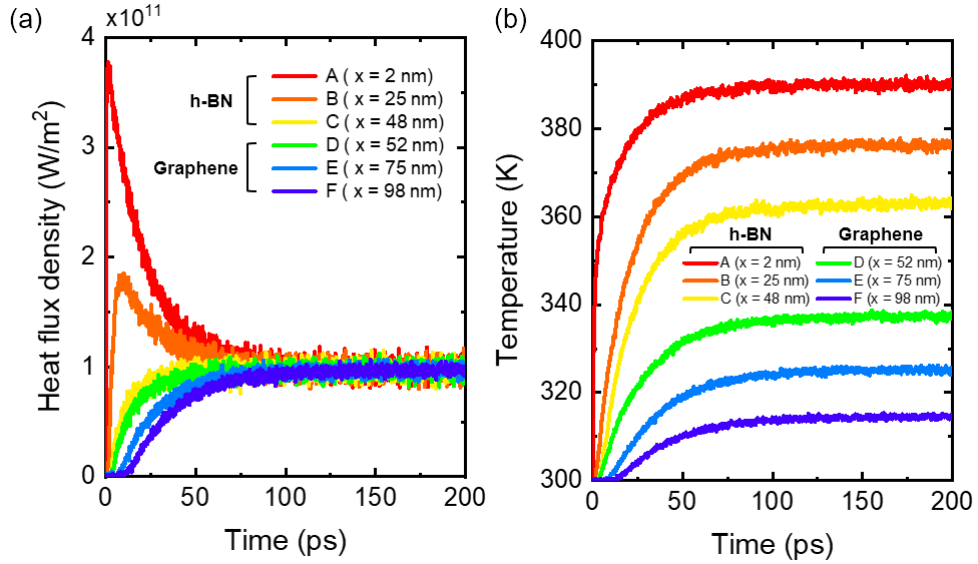

Figure 5.4 Transient (a) heat flux density and (b) temperature profiles at 6 points in 100 nm h-BN/graphene lateral heterostructure, measured from 0 to 200 ps. The rainbow color grade intuitively represents the varying heat flux densities according to their respective positions : red for position A, orange for B, yellow for C, green for D, blue for E, and navy for F (see also Figure 5.1).

Figure 5.4 (a) displays the transient heat flux density at six selected positions (A to F) within a 100 nm h-BN/graphene lateral heterostructure captured from 0 to 200 ps calculated from our Monte Carlo (MC) simulation. At t=0, a thermal gradient of T_H= 400 K and T_C = 300 K is applied. It is shown that the system approaches a steady-state within 200 ps, converging to a uniform value of approximately 9.72×10^{10} W/m^2 across all positions.

However, the thermal transient response within tens of ps exhibits significant variation depending on the position in the device. At position A, closest to the hot thermostat, the initial heat flux density

peaks instantaneously, displaying a magnitude almost four times greater than the steady-state value. This is consistent with the expected immediate response to high-temperature bias because a high thermal flux emitted by the hot thermostat with 400 K propagates ballistically in this region. The transient peak is also observed at position B, reaching twice the magnitude of the steady-state despite its moderate distance from the heat source. Conversely, at positions C and D near the interface between two materials, the peak in the heat flux density does not appears during the transient state. Beyond the interface, positions E and F initially show a delayed response and converge more slowly to the steady-state value than other locations. The extent of this delay and the rate of convergence will be quantitatively analyzed and presented with specific values in Section 5.2.3.

In Figure 5.4 (b), the temperature profiles for the designated positions illustrate the system's thermalization process over time. As observed in the results of heat flux density, the temperature reaches a steady-state within 200 ps, indicating that it no longer undergoes significant changes with time. The rate of temperature rise and the subsequent maintenance of higher temperatures are directly proportional to the proximity to the hot thermostat. Thus, the highest temperatures are observed at position A, with progressively lower temperatures recorded towards position F. There is a pronounced temperature drop between positions C and D despite the short 4 nm distance, which is indicative of interfacial thermal resistance.

Interestingly, while the sharp peaks are evident in the heat flux density responses near the hot thermostat, the temperature profiles show a more gradual increase. This observation can be explained even by the static Fourier description of heat conduction, in which the heat flux density is directly proportional to the temperature gradient. As positions become closer to the hot thermostat, the temperature initially exhibits a sharper increase, resulting in a steeper temperature gradient, leading to peaks in heat flux density. Additionally, this observation may highlight the limitations of standard temperature calculations, which assume equilibrium conditions based on the Bose-Einstein statistics, as discussed in Chapter 4. Such an approach may not fully capture the rapid changes inherent in the transient state.

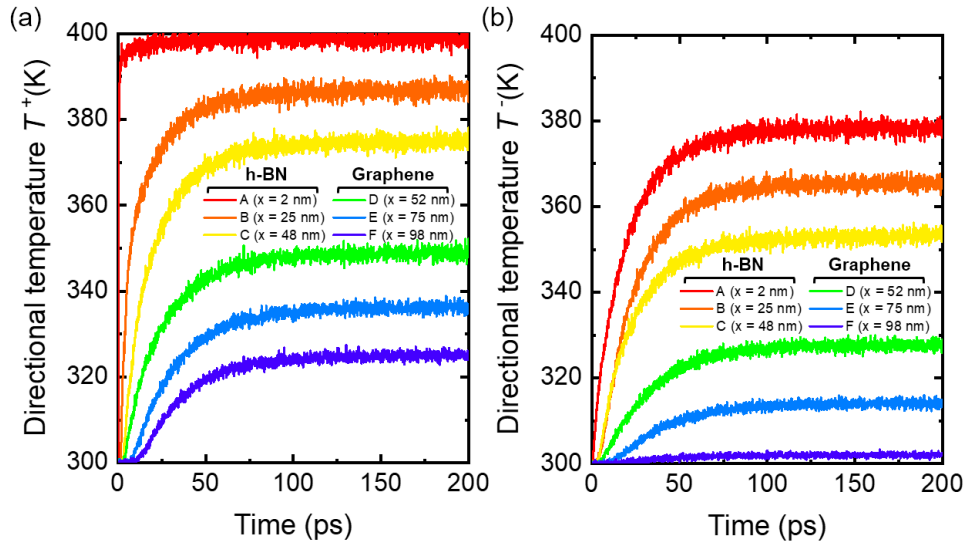

Figure 5.5 Calculated directional temperature profiles of (a) T^+ and (b) T^- for a length h-BN/graphene heterostructure with L = 100 nm at positions A to F.

To further investigate the transient regime, Figure 5.5 shows the calculated directional temperatures, T^+ in panel (a) and T^- in panel (b), for the same positions. In Figure 5.5 (a), the red line corresponding to position A exhibits an immediate increase, analogous to the heat flux density results, swiftly approaching the hot thermostat's temperature of 400 K in a few ps. This immediate rise is explained by the definition of directional temperature T^+, which considers phonons with positive velocity moving from the hot toward the cold thermostat [239]. The temperature at position F, in proximity to the cold thermostat, remains consistently close to the cold thermostat's temperature of 300 K throughout the measurement period, as depicted in Figure 5.5 (b). This consistency is due to the calculation of directional temperature T^- based on phonons with negative velocity moving away from the cold thermostat. Therefore, directional temperatures appear to be more effective parameters for modeling the representation of the transient state, marked by rapid changes, compared to standard temperature measurements.

5.2.2 Semi-analytical model for transient response

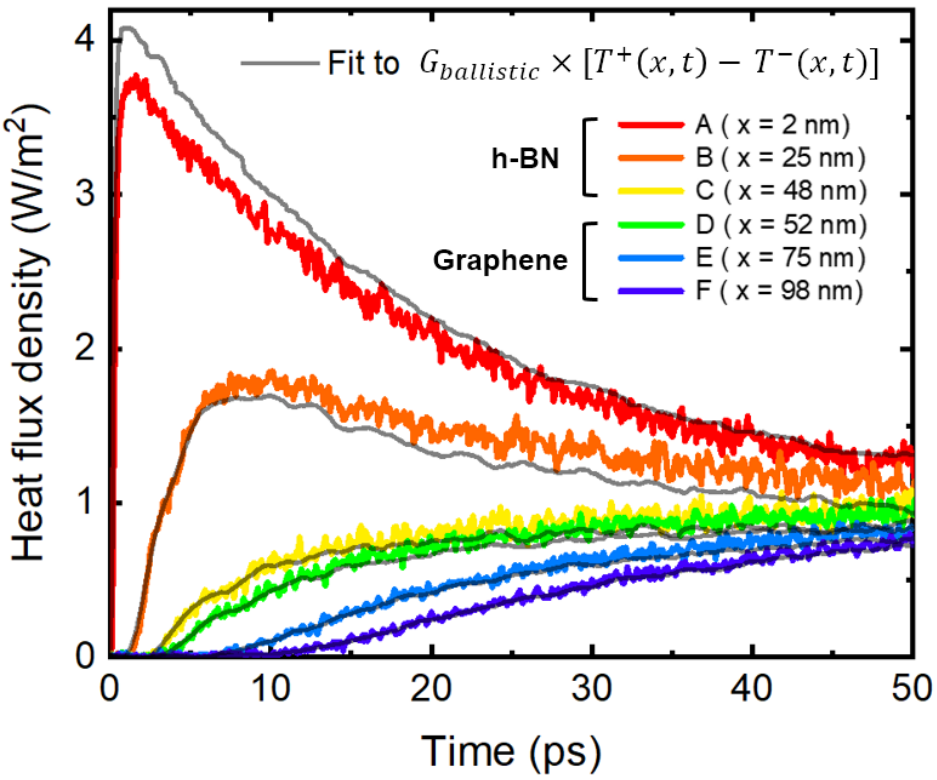

Figure 5.6 Heat flux density profiles at position A to F as a function of time for a 2D h-BN/graphene lateral heterostructure. The gray solid line represents a fit to the semi-analytical model (Equation 5.3).

In Chapter 4, it was shown that the use of directional temperatures instead of the standard temperature is more consistent in dealing with the non-equilibrium transport regime. Now, we can propose the semi-analytical (SA) model for the heat flux density in the transient regime at any position as the product of the ballistic thermal conductance of material and the difference of directional temperatures obtained from the MC simulation as follows [239,301]:

$$q(x,t) = G_{Ballistic} \times [T^+(x,t) - T^-(x,t)] \tag{5.3}$$

Where $q(x,t)$ denotes the heat flux density at a given position x and

time t. For position A, the value of $G_{Ballistic}$ at 400 K is employed to simulate the conditions near the hot thermostat, whereas for all other positions, the 300 K value is utilized. The ballistic conductance values for h-BN at positions A to C and for graphene at positions D to F are sourced from Figure 5.3, respectively. The temperature differences are calculated based on the results from Figure 5.5.

Figure 5.6 illustrates the transient heat flux density at various positions across a 2D h-BN/graphene lateral heterostructure, with a time scale expanded up to 50 ps. The heat flux density values at each position are derived from the data presented in Figure 5.4 (a). The gray solid line represents the results of fitting using the semi-analytical model expressed by equation 5.3. Apart from a slight discrepancy at the peak in position A, the SA model effectively captures the rapid changes in heat flux density within the initial tens of ps. Moreover, it accurately reflects the transition of the system towards a steady-state over time.

The established SA model, previously validated in literature with a time-independent form for its accuracy in simulating steady-state responses in silicon-based junctions and heterostructures [239,301], can be extended to reproduce the transient thermal behavior in particular in the case of 2D material-based heterostructures. This extension highlights the model's capability for analyzing temporal thermal phenomena in nanoscale devices beyond static conditions.

5.2.3 Calculation of relaxation, delay, and rise times

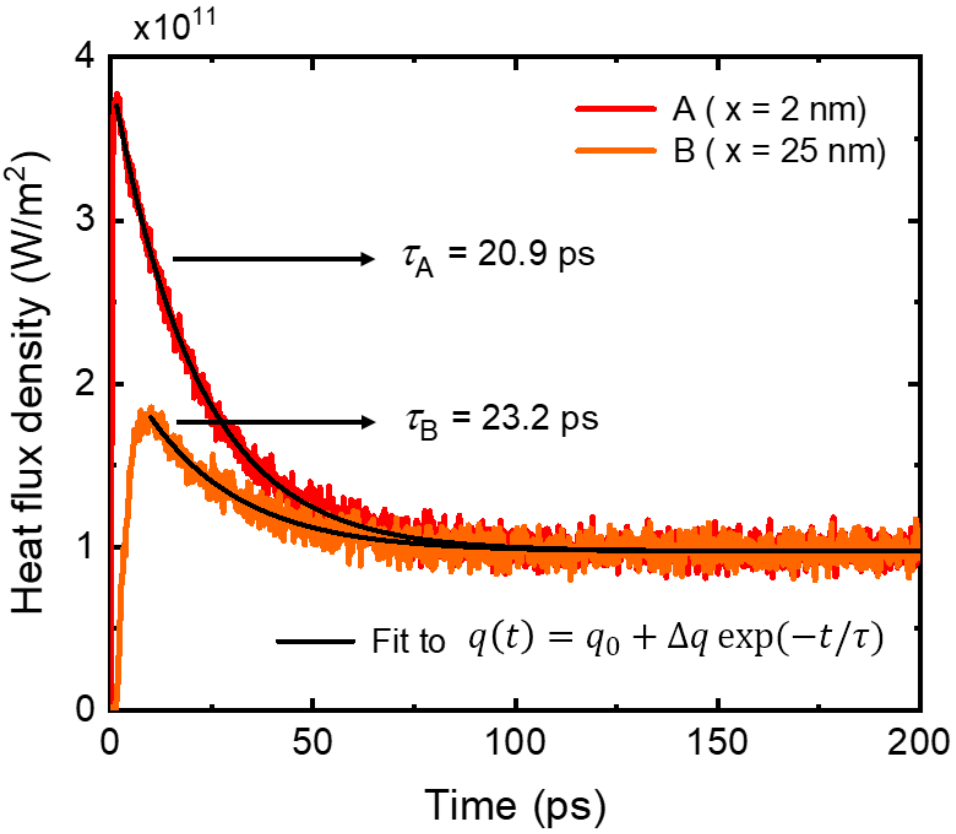

Figure 5.7 Extraction of relaxation times for positions A (2 nm) and B (25 nm) from the hot thermostat, using exponential decay fitting (black lines) based on equation 5.4. Displayed are the results with relaxation times of 20.9 ps for position A and 23.2 ps for position B.

To accurately evaluate the thermal transient response, a quantitative extraction at each position is crucial. Firstly, the relaxation time, which is the time required for the system to return near to its thermal steady-state. At positions A and B, situated 2 nm and 25 nm from the hot thermostat, respectively, the observed peaks in the transient response are dominated by ballistic transport at these nanoscale distances, where phonons propagate without scattering. Over time, diffusive transport becomes increasingly influential, evidenced by the relaxation of heat flux and the gradual temperature stabilization, signifying the transition towards a steady-state.

The thermal relaxation time of the heat flux density can be modeled by an exponential decay function [302], which characterizes how the system relaxes from the peak back to the steady-state:

$$q(t) = q_0 + \Delta q \cdot \exp(-t/\tau) \tag{5.4}$$

where $q(t)$ represents the heat flux density at time t, q_0 is the steady-state heat flux density, and Δq is the initial difference between the peak heat flux density and q_0. The constant τ indicates the relaxation time, which is the time constant for the decay process. Note that the fitting of the exponential decay to the heat flux density data is initiated at the time of the peak.

Figure 5.7 presents the extraction of relaxation times at positions A and B using equation 5.4. The relaxation time extracted at position A is 20.9 ps, marginally faster than the 23.2 ps observed at position B. A shorter relaxation time, as seen at position A, means a more expeditious return to thermal equilibrium facilitated by the ballistic transport of phonons that enables rapid thermal energy dissipation. In contrast, the more gradual relaxation at position B suggests a slower heat dissipation due to less scattering among phonons, allowing for a longer persistence of non-equilibrium conditions and a delayed return to thermal equilibrium.

Now we extend our analysis to further characterize the dynamic thermal behavior by examining delay and rise times at all specified positions within the heterostructure. In this study, the delay time is defined as the time between initiating a thermal event and the onset of the rise in heat flux density, reaching 10 % of its maximum value. The rise time is measured from this 10 % threshold to the point where the heat flux density achieves 90 % of its maximum value. For positions A and B exhibiting pronounced peaks, delay and rise times are calculated with reference to the maximum point of the peak heat flux density rather than the steady-state value. For the remaining positions, C through F, where a distinct peak is not observed, we define the maximum based on the steady-state value of the heat flux density. This analysis allows us to capture the characteristic response of each

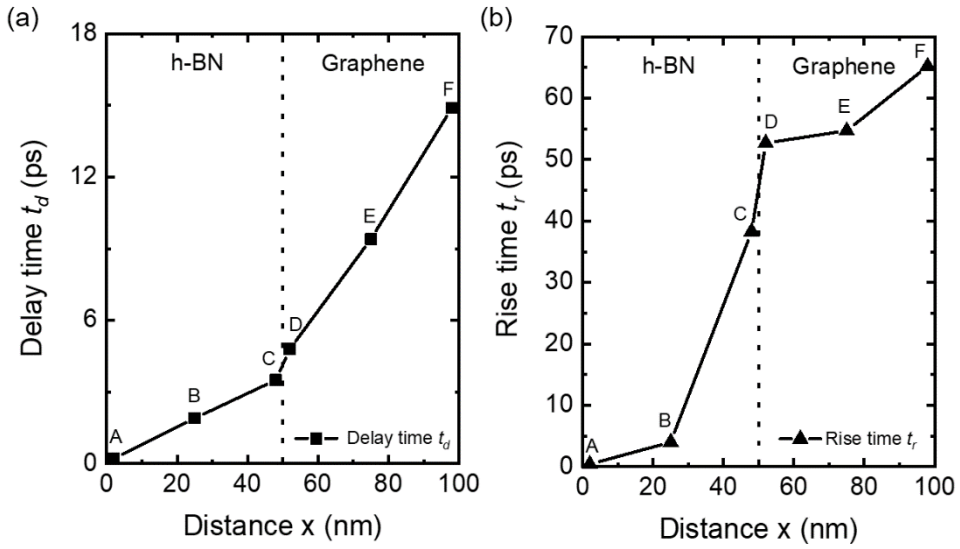

Figure 5.8 The calculated (a) delay time and (b) rise time for heat flux density at positions A through F within a 100 nm h-BN/graphene heterostructure.

position within the thermal transient process, which can vary depending on the distance from the heat source and the material properties.

Figure 5.8 shows the calculated (a) delay time and (b) rise time for heat flux density across positions A to F within a 100 nm h-BN/graphene lateral heterostructure. Panel (a) reveals that delay time increases linearly with the distance from the hot thermostat. A pronounced increase in delay time is observed between positions C and D, indicative of thermal resistance at the interface that impedes heat flow, thereby extending the delay time. Despite h-BN's lower thermal conductivity compared to graphene, the more gradual increase in delay times within the h-BN region indicates a significant role of ballistic transport at scales below 50 nm. After experiencing considerable scattering at the interface, delay time exhibits a further increase with greater distances. At position F, located 98 nm from the hot thermostat, the delay time is measured at 14.9 ps, highlighting that the thermal response can be significantly delayed as a function of distance from the heat source.

In Panel (b), the rise time also appears to increase with the distance from the hot thermostat, but the relationship is not linear. Positions A and B exhibit rise times within 4 ps, reaching the peak values very rapidly. In contrast, Position C necessitates a substantial duration to reach the steady-state value, diverging from the trend observed in delay times. Interestingly, positions D, E, and F in the graphene region show minimal variation in rise times, suggesting that graphene's superior thermal conductivity moderates the impact of distance on rise times. Therefore, rise time is influenced by both the distance from the heat source and the inherent material properties, demonstrating the complex nature of thermal behavior in h-BN/graphene heterostructure.

In summary, the calculation of relaxation, delay, and rise times provides insights into the thermal transient dynamics and the efficiency of heat distribution of the heterostructure. The combined analysis of these timescales is instrumental in designing materials and devices to maintain performance and reliability.

5.3 PHONON MODE-DEPENDENT TRANSIENT RESPONSE

5.3.1 Modal contribution in heat flux density

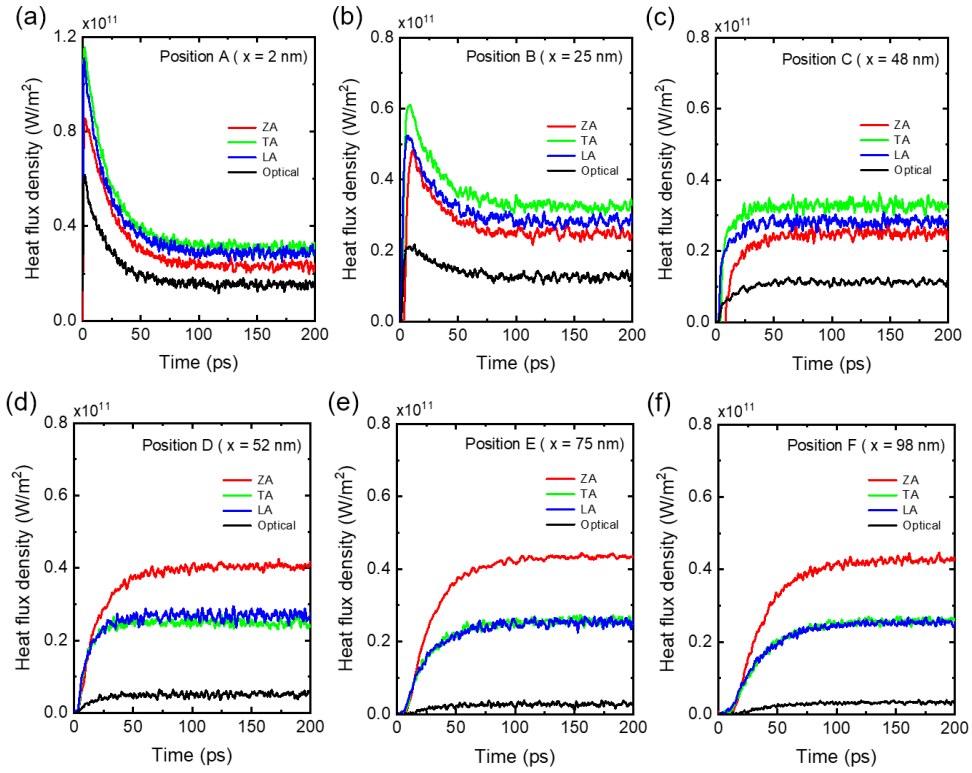

Figure 5.9 Phonon mode-dependent transient heat flux density in a 100-nm h-BN/graphene heterostructure. Panels (a)-(c) represent the h-BN region and (d)-(f) correspond to the graphene region. The data are segmented by phonon modes, with the flexural acoustic (ZA) mode represented by red lines, the transverse acoustic (TA) mode by green lines, the longitudinal acoustic (LA) mode by blue lines, and the optical phonon modes by black lines.

In this section, we aim to investigate the thermal response of various phonon modes within a 100 nm h-BN/graphene lateral heterostructure. Figure 5.9 shows the transient heat flux density, segmented by phonon modes at each position. Since h-BN and graphene have six different phonon modes, the flexural acoustic (ZA)

mode is represented by the red line, the transverse acoustic (TA) by the green line, the longitudinal acoustic (LA) by the blue line, and the three optical modes are collectively denoted by the black line. Positions A through F correspond to panels (a) through (f), respectively, with panels (a) to (c) belonging to the h-BN region and panels (d) to (f) the graphene region.

The summation of heat flux density across all phonon modes at each position is in accordance with the results presented in Figure 5.4 (a). Thus, the sum of all phonon modes converges to a uniform value in the steady-state. In the h-BN region represented by panels (a) to (c), the TA mode displays the highest contribution, followed by the LA and ZA modes in terms of contribution. Notably, the optical mode also contributes significantly to the transient response, exhibiting a pronounced peak at position A near the hot thermostat, comparable to that of the acoustic modes.

Moving to the graphene region, depicted in panels (d) to (f), a clear dominance of the ZA mode is evident, indicative of the excellent flexural movements in graphene, leading to a larger contribution from ZA modes. Relative to the h-BN area, the contribution of optical modes in graphene is less, reflecting the acoustic modes' superior thermal characteristics in this material. These trends are consistent with the modal contributions previously demonstrated in Figure 4.15 for the same structure. Therefore, the impact of each mode is distinctly discernible in the transient state and continues into the steady-state.

5.3.2 Calculation of mode-dependent relaxation, delay, and rise times

Table 1 The mode-dependent relaxation time at positions A and B

[ps]	ZA	TA	LA	Optical
Position A	22.7	20.4	19.8	20.5
Position B	22.5	23.4	23.1	25.7

Next, the relaxation time of each phonon mode at positions A and B is computed utilizing equation 5.4 from Section 5.2.2, with the results summarized in Table 1. The results reveal that the decay process from the transient peak to the thermal steady-state varies according to the phonon mode. At position A, the ZA mode exhibited the longest relaxation time of 22.7 ps, indicating the slowest response among the modes. At position B, there is an overall increase in relaxation times, especially for the optical mode, which jumped from 20.5 ps to 25.7 ps. Due to the significantly slower velocity of the optical modes compared to the acoustic modes, it can greatly influence the relaxation process at varying distances. Compared to the relaxation times of 20.9 ps for position A and 23.2 ps for position B in the total heat flux density, as shown in Figure 5.4, the relaxation times derived from the TA mode, which shows the largest contribution in h-BN, closely match these values at 20.4 ps for position A and 23.4 ps for position B, respectively.

A closer inspection of the initial transient response in Figure 5.9 reveals variations across different phonon modes, even at the same position. Expanding upon the preliminary observations in Figure 5.8, Figure 5.10 presents the calculated (a) delay time and (b) rise time for each phonon mode at respective positions. While the delay time increases linearly with distance from the hot thermostat, mirroring the trend observed in Figure 5.8 (a), the rate of this increase depends on the phonon mode. Within the h-BN region from position A to C, the ZA mode exhibits the most significant delay compared to other modes. Reflecting its rapid group velocity, the LA mode demonstrates the lowest delay.

Upon crossing the interface into the graphene region, despite the

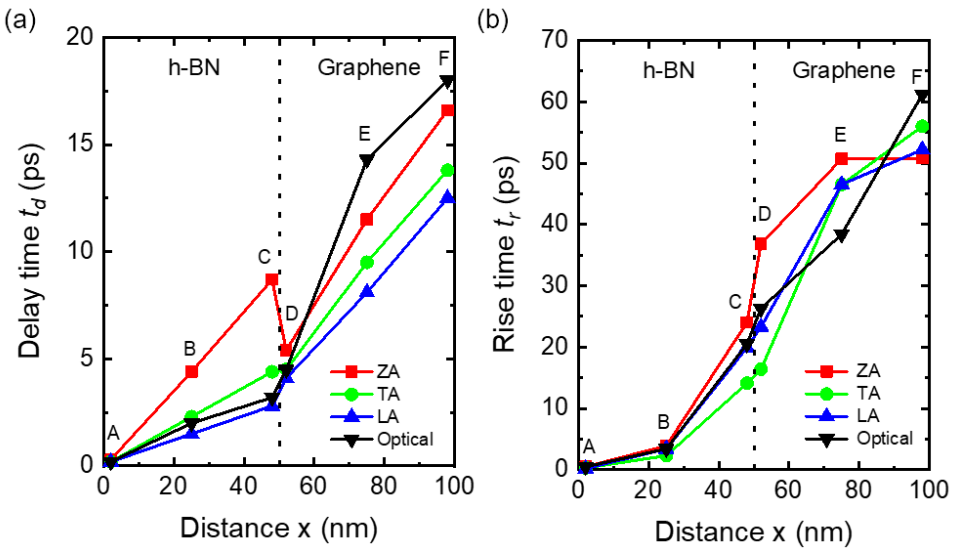

Figure 5.10 The calculated mode-dependent (a) delay time and (b) rise time for heat flux density at positions A through F within a 100 nm h-BN/graphene heterostructure.

influence of the diffusive interface and the increasing distance, there is a notable reduction in the delay time of the ZA mode at position D, which underscores the remarkable thermal characteristics of graphene's ZA mode. Conversely, the optical mode responds relatively fast in the h-BN region, but experiences the most significant delay increase as distance extends, reaching a pinnacle in the highest delay time at position F.

Figure 5.10 (b) shows that the rise times for modes at positions A and B are nearly indistinguishable by ballistic phonon transport. However, as approach the interface, the rise-time differences between modes become markedly apparent. The ZA mode in the h-BN region exhibits the longest rise time, even longer than that of the optical mode, while the ZA mode in graphene shows the smallest variance in rise time with increasing distance. The optical mode, significantly influenced by distance, displays a distinct pattern of growing rise time, with a notable surge between positions E and F. This suggests that the pronounced rise in time from E to F, as seen in Figure 5.8 (b), can likely be attributed to the optical mode.

5.4 EFFECT OF THE INTERFACE ON TRANSIENT THERMAL RESPONSE

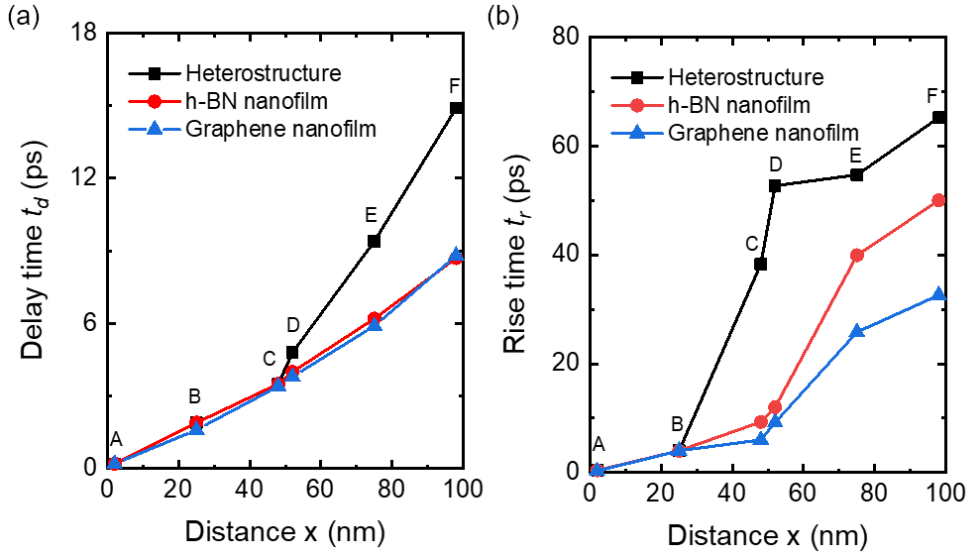

Figure 5.11 Comparative analysis of (a) delay time and (b) rise time for h-BN (red line) and graphene (blue line) nanofilms and h-BN/graphene heterostructure (black line). Data points A through F indicate specific positions.

Lastly, we investigate the impact of the interface on the transient thermal response by comparing homogeneous nanofilms of 2D h-BN and graphene with the h-BN/graphene heterostructure. The transient responses are measured under an identical temperature bias across homogeneous nanofilms with a uniform length of 100 nm. Then, delay and rise times are recorded at designated positions from A to F.

Figure 5.11 presents (a) delay time and (b) rise time for the heterostructure, as well as homogeneous h-BN and graphene nanofilms, corresponding to the black, red, and blue lines, respectively. The results for the heterostructure are obtained from Figure 5.8 for comparison. In Figure 5.11 (a), the delay time exhibits an almost linear trend from the heat source. While graphene displays a slightly shorter delay time than h-BN, the difference is negligible. Since the heterostructure consists of h-BN material up to a distance of 50 nm, it maintains a consistent delay time with h-BN nanofilm. Starting from position D, the slope of delay time changes, indicating that the

interface causes further delay in the transient response. As the distance increases, the discrepancy in delay times becomes more pronounced, resulting in a twice difference at Position F.

The rise times at positions A and B are consistent across different structures by ballistic transport as shown in Figure 5.11 (b). In general, graphene exhibits the quickest rise time, followed by h-BN and then the heterostructure as expected. Interestingly, despite being the same h-BN material at position C, the rise time in the heterostructure differs significantly compared to the homogeneous h-BN nanofilm, suggesting that the interface in the heterostructure notably impedes phonon diffusion in the transient regime. When moving from position C to D, the rise time in the h-BN and graphene nanofilms without an interface does not significantly change, unlike in the heterostructure. At position F, the rise time is about twice that of the graphene nanofilm compared to the heterostructure consisting of the same material at this position, which indicates a substantial overall effect of the interface. In summary, the rise time is influenced by a combination of factors, including the distance from the heat source, device structure, and material properties.

Additionally, the accuracy of homogeneous nanofilms' calculated delay and rise times can be cross-verified by the characteristic time through a lumped thermal capacity model, as discussed in Section 5.1.2. For h-BN and graphene nanofilms with a length of 98 nm, the characteristic times were 48.2 ps and 41.6 ps, respectively. These times are comparable to the combined delay and rise times, $t_d + t_r$, of 58.7 ps for h-BN and 41.4 ps for graphene nanofilms at position F (98 nm), providing a physical verification for the transient thermal analysis conducted. Note that using ballistic thermal conductance in these estimations allows for an inference about the extent of ballistic transport. The close alignment of characteristic time and $t_d + t_r$ for graphene suggests a predominantly ballistic transport, while the discrepancy observed for h-BN indicates a mix of diffusive and ballistic transport in its transient response.

5.5 SUMMARY

In Chapter 5, we have presented a detailed examination of the transient thermal response in 100 nm h-BN/graphene lateral heterostructure via Monte Carlo simulations. The study is motivated by the fact that transient temperature fluctuations can critically affect the functionality of nanometer-scaled devices.

Firstly, we quantify the volumetric heat capacity for h-BN and graphene, showing the values of 1.84 MJ/m^3K and 1.71 MJ/m^3K at 300 K, respectively, comparing them with experimental values to ensure accuracy. It is also noted that graphene exhibits higher ballistic thermal conductance than h-BN at room temperature. Through positional mapping, the study analyzes transient thermal properties across various locations of the heterostructure, revealing that initial heat flux density is maximal almost instantaneously near the hot thermostat and that phonon trajectories are notably disturbed at interfaces in transient state. The semi-analytical model proposed offers a robust representation of the transient heat flux density based on directional temperatures, effectively capturing not only rapid initial changes, but also the system's transition towards the steady-state.

By defining the relaxation, delay, and rise times, we characterized the dynamic thermal behavior, observing that these parameters are significantly affected by distance from the heat source and material properties. Our study also examined the transient heat flux density by phonon modes, noting the pronounced impact of TA and ZA modes in the h-BN and graphene regions, respectively. It is found that the interface's impact on the transient thermal response is considerable, presenting a substantial difference in the rise time within the heterostructure compared to homogeneous nanofilms.

This research can provide critical insights into the thermal dynamics of nanoscale devices, highlighting the importance of transient response analysis and the essential role of device architecture in thermal management for device reliability.

6 CONCLUSION AND PERSPECTIVES

In this thesis, we have advanced the understanding of phonon transport in nanostructures through a full-band Monte Carlo (MC) simulation. All material parameters such as phonon dispersions and scattering rates were calculated through ab-initio methods. This research extends our previous computational approach, initially focused on silicon, to encompass gallium arsenide (GaAs) and a variety of two-dimensional (2D) materials, thereby verifying the versatility and effectiveness of our simulation code across different material systems. Moreover, a unique aspect of this research lies in the precise calculation of phonon scattering mechanisms using density functional theory (DFT) and density functional perturbation theory (DFPT).

The first Chapter introduced the historical context and state-of-the-art outcomes, including a thorough review of each material's thermal characteristics. We discussed the limitations of classical Fourier's law at the nanoscale highlighting its inadequacies for devices where phonon mean free paths are comparable to device dimensions. Against this backdrop, various simulation methods were explored for their strengths and weaknesses. Our choice to integrate DFT calculations into the MC algorithm approach enabled us to accurately and efficiently compute a broad spectrum of nanostructures.

In Chapter 2, we established the theoretical basis of this thesis, detailing the ab-initio formalism and MC algorithm for device simulation. Using DFT and DFPT within the Quantum ESPRESSO suite, we examined the linear response of systems to small perturbations, enabling analysis of lattice dynamics. This foundation allowed for the detailed consideration of non-linear phonon interactions, distinguishing between normal and Umklapp processes and considering previously overlooked isotope scattering effects. Then, we detailed the methodology for the MC simulation algorithm to solve the Boltzmann transport equation (BTE) for phonons. Within the framework of the relaxation time approximation (RTA), our approach encompassed the complexities of phonon interactions, the presence of impurities, and the effects of structural boundaries across various

nanostructures. Furthermore, we elaborated on methods to accurately determine temperatures under non-equilibrium conditions. Our discussion extended to analytical models, providing a comparative approach to validate our numerical results.

In the subsequent Chapter 3, we presented the outcomes of our investigations, focusing on the thermal characteristics of GaAs nanostructures. This study was initiated with the ab-initio based analysis to calculate phonon dispersions, group velocities, and scattering rates, inclusive of isotopic effects, across the first Brillouin zone for GaAs. When compared with experimental data, the thermal conductivity values obtained for bulk GaAs demonstrated a remarkable concordance at room temperature. This alignment with theoretical predictions and experimental observations underscores the validity and reliability of our computational approach in elucidating the thermal properties of GaAs materials.

Building upon the material properties, we designed various nanostructures such as cross-plane nanofilms (CPNF), in-plane nanofilms (IPNF), rough nanowires (NW), and porous nanowires (Porous NW) depending on boundary conditions. Our simulations revealed that ultra-short films exhibit thermal conductivities that align with the ballistic transport regime. As nanofilm length increases, thermal conductivity transitions towards diffusive values, showing an asymptotic behavior. For CPNF with a 100 nm length, the Matthiessen model overestimated thermal conductivity by about 40 % compared to our numerical results. Conversely, the effective model, previously validated for silicon nanofilms, achieved remarkable accuracy.

In structures shorter than 10 nm, where ballistic transport dominates, thermal transport properties were found to be almost identical across device types. However, for lengths of 10 μm, IPNF and NW experienced substantial reductions in thermal conductivity compared to CPNF, by 41 % and 52 % respectively. The influence of device width was notably pronounced in IPNF and NW, especially at narrower widths due to rough boundary effects. Beyond certain dimensions, where the device width surpassed its length, the influence of rough boundaries diminished, and thermal conductivities across all device types converged.

We also investigated the transition between different transport regimes across temperatures ranging from 0.1 to 1000 K, focusing on the shifts between ballistic and diffusive modes as temperature changes. Utilizing the Knudsen number (K_D), we characterized the extent of ballistic transport in the devices. For ultra-short devices with 10 nm, K_D values remained above 0.5 across the entire temperature spectrum, signifying a dominance of ballistic transport with minimal phonon scattering. In contrast, for devices extending to 10 μm, we observed a significant decrease in K_D with increasing temperature, indicating a swift transition from ballistic to diffusive transport.

In the analysis of the contributions of individual phonon modes to heat flux density, the longitudinal acoustic (LA) mode consistently played a significant role across all device types and lengths, attributed to its high group velocity. Notably, in devices as short as 10 nm, the contribution from optical modes surpassed 20 %, marking them as important factors in heat transport regardless of the device type. By calculating the accumulated thermal conductivity relative to the mean free paths (MFP) of each phonon mode, we revealed that optical modes make the highest contribution in the 10~20 nm MFP range. These findings underline the significant effect of device size on phonon mode contributions to thermal transport.

Finally, we extended our analysis to consider the influence of nanopores within NW, simulating the potential for defects that could occur during the synthesis process. Our findings showed a marked degradation in thermal conductivity with increased porosity, observing a twofold decrease at 20 % porosity. Through this investigation, we gained a detailed understanding of the interplay between microstructural variations and their effects on the thermal properties.

In Chapter 4, we studied the thermal properties of 2D materials and their lateral heterostructures, focusing on monolayer forms of hexagonal boron nitride (h-BN), graphene, molybdenum disulfide (MoS_2), and tungsten diselenide (WSe_2). Our study provided a detailed cartographic analysis of phonon group velocities and scattering rates across the entire Brillouin zone at 300 K, uncovering distinct non-isotropic characteristics. We analyzed the average phonon scattering rates across a wide temperature spectrum. Our findings illustrated the

predominance of normal scattering processes, particularly in graphene. WSe_2, however, presented a distinct pattern with no clear dominance of normal over Umklapp scattering, possibly due to the increased anharmonicity from heavier atoms that facilitate Umklapp processes. 2D h-BN exhibited significant phonon-isotope scattering due to a substantial isotope mixture, underscoring the necessity of considering isotope effects in thermal transport simulations.

Then, we explored the length-dependent thermal conductivity of h-BN, graphene, MoS_2, and WSe_2 nanofilms at room temperature. We found that at a device length of 10 μm, the thermal conductivity closely aligns with experimental measurements. However, a slight discrepancy was observed for graphene, likely due to the limitations of employing the RTA in scenarios where normal scattering processes predominate. Despite this, the overall consistency of our simulation results with experimental data underscores the model's reliability.

In exploring lateral heterostructures, such as h-BN/graphene and MoS_2/WSe_2 combinations, we applied the diffuse mismatch model (DMM) to describe phonon transmission and reflection at the interfaces. To address the challenge of accurately evaluating temperature near the interface, we introduced the concept of directional temperature. This approach enabled us to capture the non-equilibrium states near the interfaces more precisely than the standard temperature measurement. Our findings revealed the interface thermal conductance (ITC) value in lateral heterostructures, closely aligning with analytical model predictions. Based on the evolution of phonon modal contribution near the interface, a strong non-equilibrium transport regime exists within a few nanometers of the interface. Therefore, we concluded that the introduction of directional temperature provided a more accurate representation of these conditions, enabling a precise calculation of ITC.

Finally, in Chapter 5, we investigated the transient thermal responses of heterostructures, presenting an in-depth study of 100 nm 2D h-BN/graphene lateral heterostructures. This study began with the calculation of crucial material parameters, such as volumetric heat capacity and ballistic thermal conductance. The precision of these calculations, evidenced by their close alignment with experimental

data around room temperature. We then subjected the heterostructures to transient high-temperature conditions, rapidly transitioning the hot thermostat from 300 K to 400 K at t=0 s while maintaining the cold thermostat at 300 K. Our observations indicated that the system reached a steady-state within 200 picoseconds. Notably, areas closest to the hot thermostat experienced an initial surge in heat flux density, peaking almost instantaneously to nearly four times the value observed at steady-state.

Consistently with the research presented in previous chapters, we applied the concept of directional temperatures to more effectively model the rapid changes observed in the transient state. Our approach involved validating a semi-analytical (SA) model based on directional temperatures combined with the ballistic conductance of the materials. We demonstrated that the SA model, previously affirmed for its precision in steady-state simulations of silicon-based junctions and heterostructures, could be aptly extended to characterize the transient thermal dynamics in 2D material-based heterostructures.

In this study, we quantified various response characteristics, including the relaxation time, rise time, and delay time. It was observed that delay time increases linearly with distance from the heat source. Additionally, we explored the thermal transient response of different phonon modes. Our findings indicated that the TA mode in the h-BN region offers the highest contribution to total heat flux. In contrast, the graphene region showcased a pronounced dominance of the ZA mode, highlighting its efficiency as a flexural mode in graphene.

In concluding our study, we confirmed the significant impact of interfaces on the transient thermal response by comparing homogeneous nanofilms of 2D h-BN and graphene against the h-BN/graphene heterostructure. Our investigations revealed that the presence of an interface significantly increases delay times following the interface, underscoring its role in further delaying the thermal response. Notably, as the distance from the interface increases, the discrepancy in delay times between the heterostructure and homogeneous nanofilms becomes increasingly evident, quantitatively demonstrating the substantial influence of interfaces on transient thermal behaviors.

The findings of this thesis not only contribute to our existing knowledge, but also uncover new questions and opportunities for future investigations. Particularly promising directions for future research include the improvement of the RTA framework and the exploration of van der Waals (vdW) heterostructures.

First, traditional RTA models often oversimplify the scattering processes by assuming all phonon interactions contribute equally to relaxation. However, normal scattering processes conserve momentum and do not degrade the thermal current as much as Umklapp processes, which are resistive scatterings where momentum is not conserved. To overcome these limitations and enhance the precision of our models, Callaway's dual RTA model can be incorporated into our MC algorithm. This model addresses the strong normal scattering characteristics by treating the two scattering mechanisms independently, offering a more realistic description of thermal transport. Therefore, particularly in graphene, which has dominant normal scattering processes, it is expected to yield a closer match with experimental data without substantially increasing computational complexity.

Another promising direction involves investigating vdW heterostructures, composed of vertically stacked layered materials held together by vdW forces. These structures pose unique challenges and opportunities for thermal transport studies. Van der Waals forces are crucial for the structural stability and physical properties of layered materials like bilayer graphene. However, the local density approximation (LDA) used in our DFT calculations may underestimate the interlayer binding energy and layer separation distances, leading to inaccuracies in predicting the material's structural, mechanical, and thermal properties.

Therefore, incorporating vdW corrections is pivotal, as they account for the weak yet significant interactions characteristic of vdW materials. By enhancing DFT calculations with vdW corrections, we could model the physical behavior of layers in vdW materials more accurately. Nevertheless, calculating third-order derivatives of the energy with respect to atomic displacements, which is essential for understanding anharmonic phonon interactions in these systems, presents significant

computational challenges. Future work will require developing methodologies that can efficiently compute these quantities, thereby extending our ability to analyze thermal transport in vdW heterostructures with greater fidelity.

RESUME EN FRANÇAIS

A.1 INTRODUCTION

En faisant progresser notre compréhension du transport des phonons dans les nanostructures, cette thèse s'inspire de l'interaction complexe des phénomènes thermiques à l'échelle nanométrique, un domaine où les modèles traditionnels de transfert de chaleur rencontrent des limites importantes. À mesure que les dispositifs diminuent jusqu'à l'échelle nanométrique, la gestion efficace de la chaleur devient primordiale, les dynamiques des phonons jouant un rôle clé dans la détermination des propriétés thermiques des matériaux semi-conducteurs.

Conformément à la tendance vers des dispositifs plus compacts et performants au-delà de la technologie conventionnelle basée sur le silicium, une augmentation de la recherche explorant des matériaux alternatifs tels que les composés et les matériaux bidimensionnels (2D) a été observée, chacun offrant des avantages distincts par rapport au silicium. Par exemple, l'arséniure de gallium (GaAs), caractérisé par une plus grande mobilité des électrons et une bande interdite directe, semble prometteur pour les dispositifs électroniques de nouvelle génération en raison de son adaptabilité pour des nanostructures telles que les nanofils et les superréseaux. De même, les matériaux 2D comme le graphène et le nitrure de bore hexagonal (h-BN), ainsi que les dichalcogénures de métaux de transition (TMDCs), y compris le disulfure de molybdène (MoS_2) et le séléniure de tungstène (WSe_2), ont attiré l'attention pour leurs propriétés électriques, thermiques et mécaniques exceptionnelles. Bien que la recherche en cours montre un potentiel pour de larges applications dans divers domaines, l'étude des propriétés de transport thermique dans ces matériaux a été relativement peu explorée.

De plus, les hétérostructures composées de divers matériaux 2D se sont avérées particulièrement intrigantes en raison de leurs propriétés nouvelles qui vont au-delà de celles des composants individuels et de leur flexibilité pour l'ingénierie des dispositifs. Bien que des efforts expérimentaux aient permis de réussir à fabriquer des hétérostructures

aussi bien dans le plan que hors du plan en utilisant des interfaces de type van der Waals (vdW), mesurer avec précision leurs propriétés thermiques reste un défi. Notamment, l'évaluation expérimentale des propriétés thermiques dans les hétérostructures latérales (dans le plan) pose plus de difficultés que dans les hétérostructures de van der Waals. Ainsi, des techniques de simulation avancées sont devenues cruciales pour examiner les propriétés thermiques des hétérostructures dans le plan, offrant des informations détaillées sur les dynamiques des phonons et le transport thermique aux interfaces.

Dans cette thèse, nous étudions le transport des phonons au sein de diverses nanostructures en utilisant des méthodes stochastiques de Monte Carlo. La précision des simulations est améliorée par l'utilisation d'une description complète des bandes de matériaux (approche « Full-band ») dérivées des calculs ab-initio basés sur la théorie de la fonctionnelle de la densité (DFT) n'ayant pas recours à des paramètres empiriques.

A.2 Methodologie

A.2.1 Calculs ab-initio

Dans le cadre de la DFT, l'équation de Kohn–Sham est résolue en utilisant la densité d'électrons à l'état fondamental pour déterminer l'énergie de la structure électronique. Alors que la DFT vise à décrire la structure électronique d'un système dans son état fondamental, la théorie de la perturbation fonctionnelle de densité (DFPT) étend ce concept à la réponse linéaire du système c'est-à-dire à de petites perturbations en déplaçant légèrement les atomes de leur position d'équilibre. Puisque le phonon est un mode quantifié de vibration prenant en compte des déformations dynamiques dans un solide cristallin, le DFPT constitue ainsi un outil puissant pour prédire la dynamique du réseau, ce qui est essentiel pour étudier les propriétés thermiques telles que la fréquence angulaire, la vitesse de groupe et leur interaction. Cette approche souligne la complexité des interactions de phonons, en mettant particulièrement en évidence l'influence significative de l'anharmonicité sur le transport thermique.

Tous ces calculs sont effectués à l'aide de la suite Quantum ESPRESSO.

A.2.2 Monte Carlo simulation

Par la suite, une méthode stochastique particulaire Monte Carlo (MC) pour résoudre l'équation de transport de Boltzmann (BTE) dans les simulations de transport de phonons a été introduite. L'utilisation de l'approximation du temps de relaxation permet de simuler le transport des phonons en tenant compte des interactions des phonons, des impuretés et des frontières structurelles au sein de diverses nanostructures. Notre analyse évalue de manière exhaustive ces mécanismes de dispersion des phonons sur un large spectre de températures, allant des températures cryogéniques 0,1 K jusqu'à 1000 K. La transmission de phonons à travers l'interface entre différents matériaux est mise en œuvre à l'aide d'une version à bande complète du modèle DMM (Diffuse Mismatch Model) dans notre simulation MC.

La température à chaque position dans la structure simulée doit être mise à jour en continu pour déterminer avec précision les propriétés thermiques. La pseudo-température standard T est dérivée de la densité d'énergie des phonons à chaque position dans le dispositif simulé selon les statistiques d'équilibre de Bose-Einstein pour chaque matériau. Cependant, la définition standard de la température, qui suppose une condition d'équilibre, pourrait ne pas être appropriée pour calculer la conductance thermique à l'interface. Pour analyser de manière exhaustive la dynamique du transport de chaleur, les phonons peuvent être distingués en deux catégories selon leur direction de mouvement. Dans ce contexte, les températures directionnelles, T^+ et T^- , sont introduites, correspondant respectivement aux sous-populations de phonons avec des vitesses positives et négatives. Opter pour les températures directionnelles T^+ et T^- plutôt que pour la pseudo-température standard T offre une représentation plus précise des conditions de non-équilibre.

Nous avons décrit l'algorithme de simulation Monte Carlo étape par étape, démontrant comment calculer des propriétés thermiques telles que la conductivité thermique et la conductance thermique à

l'interface. Des modèles analytiques sont également discutés pour établir un lien entre la compréhension théorique et la simulation informatique dans l'étude du transport des phonons dans les nanostructures. Cette base théorique et de simulation sera appliquée dans les chapitres suivants à des investigations détaillées du comportement des phonons dans des nanostructures à base de GaAs et de matériaux 2D.

A.3 Simulation Monte Carlo a bande complete de nanostructures de GaAs pour le transport des phonons base sur des methodes ab-initio

Dans ce chapitre, nous avons exploré les caractéristiques de transport thermique des nanostructures de GaAs via des simulations Monte Carlo. Les propriétés des matériaux dérivées de calcul ab initio du GaAs valident l'approche computationnelle par rapport aux données expérimentales et fournissent une base solide pour les simulations MC ultérieures. Cela renforce ainsi l'applicabilité de la DFT et de la DFPT pour l'étudedu transport des phonons.

Grâce à la modélisation de nanostructures de GaAs avec la mise en œuvre de conditions aux limites, il est montré que la conductivité thermique dépend fortement des dimensions des dispositifs et de la température. Cette étude fournit également des éclaircissements sur la transition du régime de transport entre les régimes balistique et diffusif au moyen du nombre de Knudsen.

La Figure A.1 montre que nos résultats Monte Carlo sont pertinents dans tous les régimes de transport de phonons, c'est-à-dire balistique, quasi-balistique et diffusif, sans utiliser de paramètres d'ajustement, offrant un outil robuste pour capturer des comportements thermiques complexes.

Les contributions des modes de phonons au transport thermique permettent de révéler la contribution des modes optiques, en particulier dans les longueurs correspondant à leur libre parcours moyen, comme le montre la Figure A.2 (a) et (b). La section finale

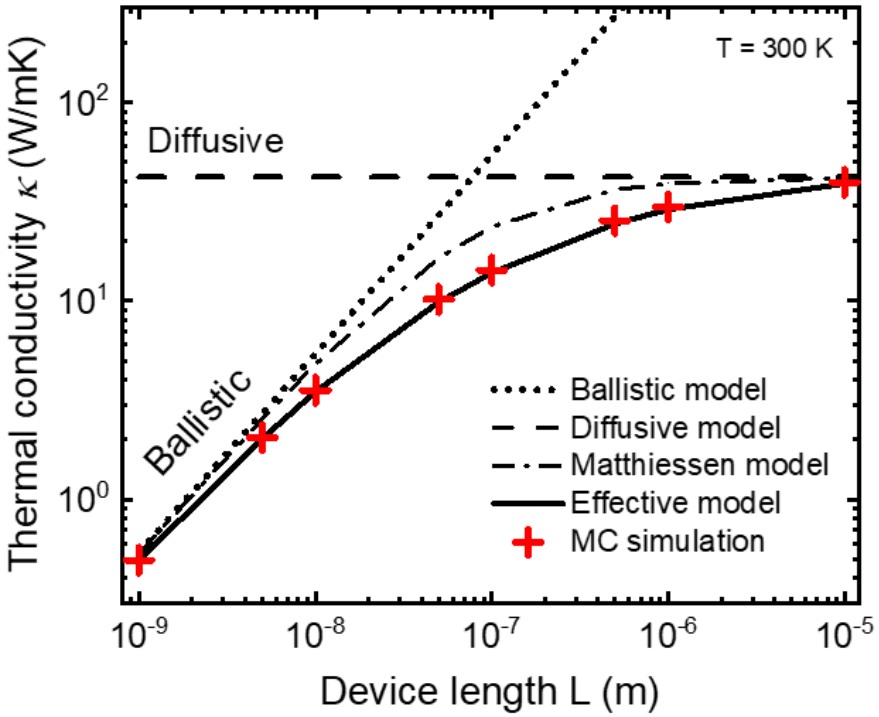

Figure A.1 Conductivité thermique en fonction de la longueur pour des nanofilms de GaAs.

aborde l'effet de dégradation des nanopores sur la conductivité thermique des nanofils de GaAs, en tenant compte des imperfections potentielles dans le processus de synthèse. Néanmoins, une simulation plus précise, incluant la complexité du processus de fabrication, reste un défi. Des investigations supplémentaires sont nécessaires pour capturer leurs subtilités de dispersion et de transport des phonons avec une plus grande précision.

Tout au long de ce chapitre, les effets de la taille des dispositifs, des bords, et de la température sur la conductivité thermique ont été méticuleusement analysés, ce qui pourraient être largement utilisés pour explorer les propriétés thermiques de divers matériaux et de nanostructures afin d'optimiser les conceptions de nanostructures pour atteindre les propriétés de transport thermique souhaitées.

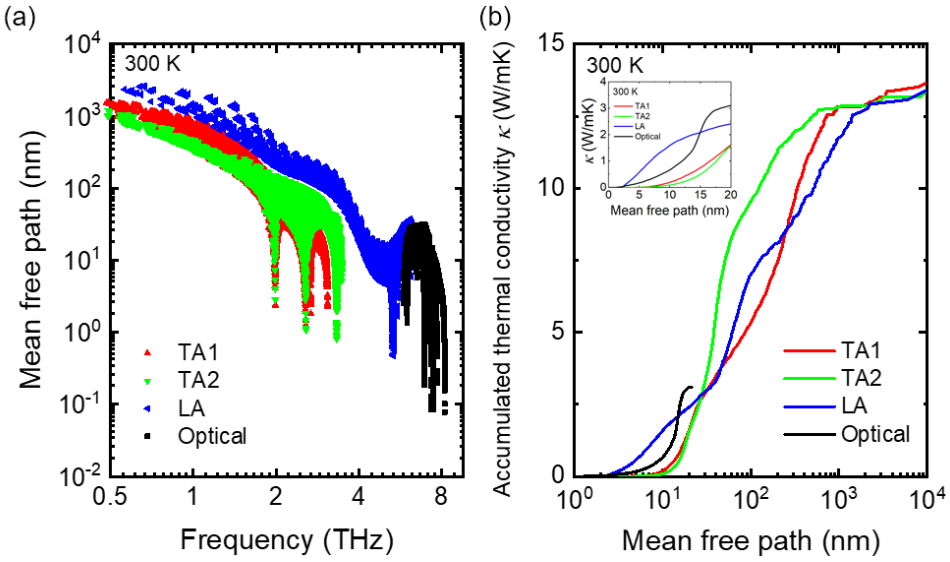

Figure A.2 (a) Le libre parcours moyen des phonons (MFP) calculé en fonction de la fréquence et (b) la conductivité thermique cumulée par rapport au libre parcours moyen pour les modes de phonons individuels à 300 K. L'encart montre une vue agrandie de la conductivité thermique cumulée pour les modes de phonons de libres parcours moyens de 0 à 20 nm.

A.4 SIMULATION MONTE CARLO A BANDE COMPLETE DU TRANSPORT THERMIQUE A TRAVERS L'INTERFACE LATERALE ENTRE DES MATERIAUX 2D

Ce chapitre présente une analyse approfondie du transport thermique dans les matériaux 2D (h-BN, graphène, MoS_2 et WSe_2) et de leurs hétérostructures latérales. Dans les calculs DFT, la précision des résultats est démontrée par le bon accord entre la dispersion de phonons calculée et les données expérimentales, évitant le problème des fréquences négatives non physiques. Une avancée significative présentée dans le chapitre est la représentation cartographique détaillée des vitesses de groupe des phonons et des taux de diffusion pour les matériaux 2D. Cela révèle des caractéristiques non isotropiques, soulignant l'importance d'utiliser une description à bande complète de la zone de Brillouin.

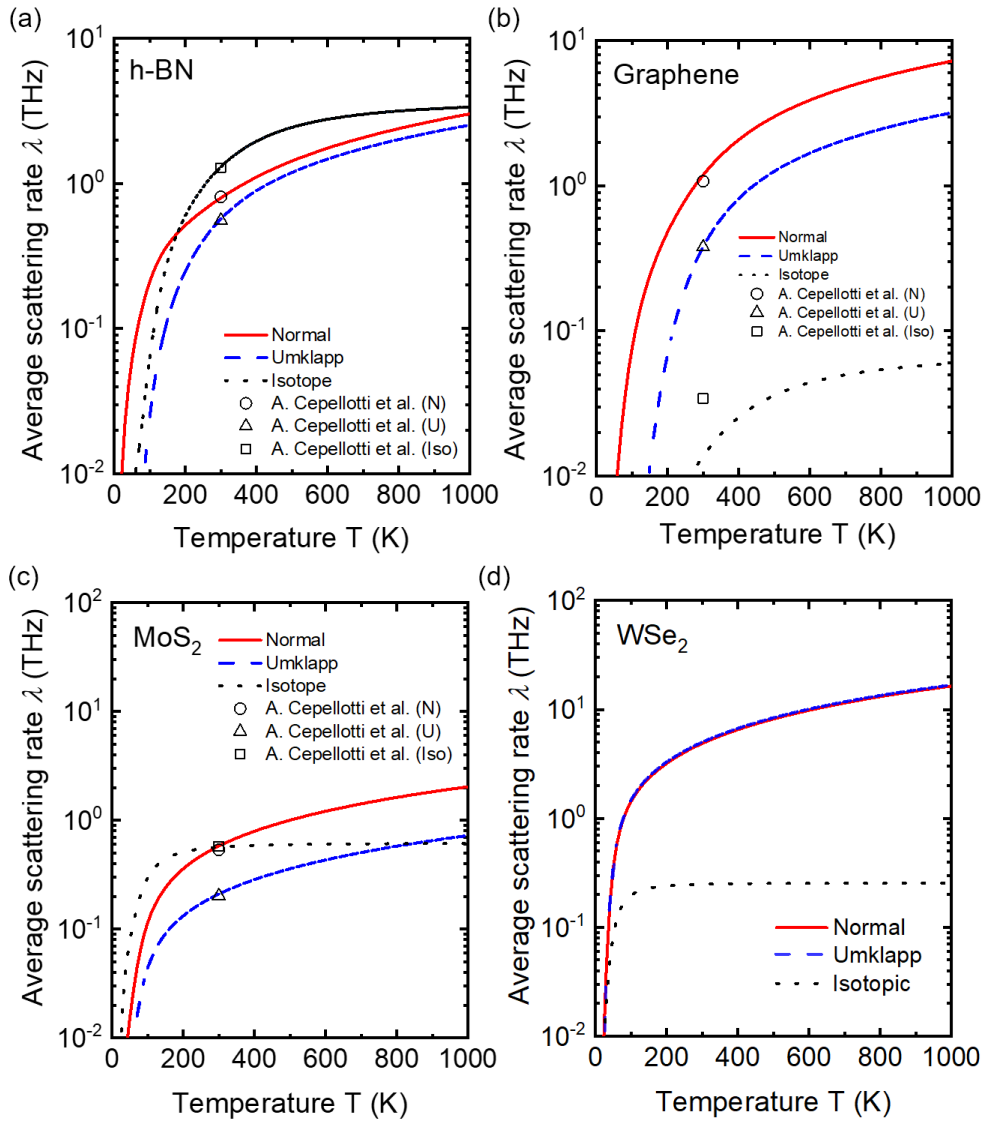

Figure A.3 Taux moyens de diffusion des phonons pour (a) h-BN, (b) Graphène, (c) MoS_2, et (d) WSe_2. Ces taux, qui incluent les processus normaux (ligne continue rouge), Umklapp (ligne pointillée bleue), et Isotopique (ligne pointillée noire), sont tracés en fonction de la température, allant de 0,1 à 1000 K. Les points de données provenant des travaux de A. Cepellotti et al. à 300 K sont indiqués par des symboles: cercles pour les processus normaux (N), triangles pour les processus Umklapp (U), et carrés pour la diffusion d'isotopes (Iso).

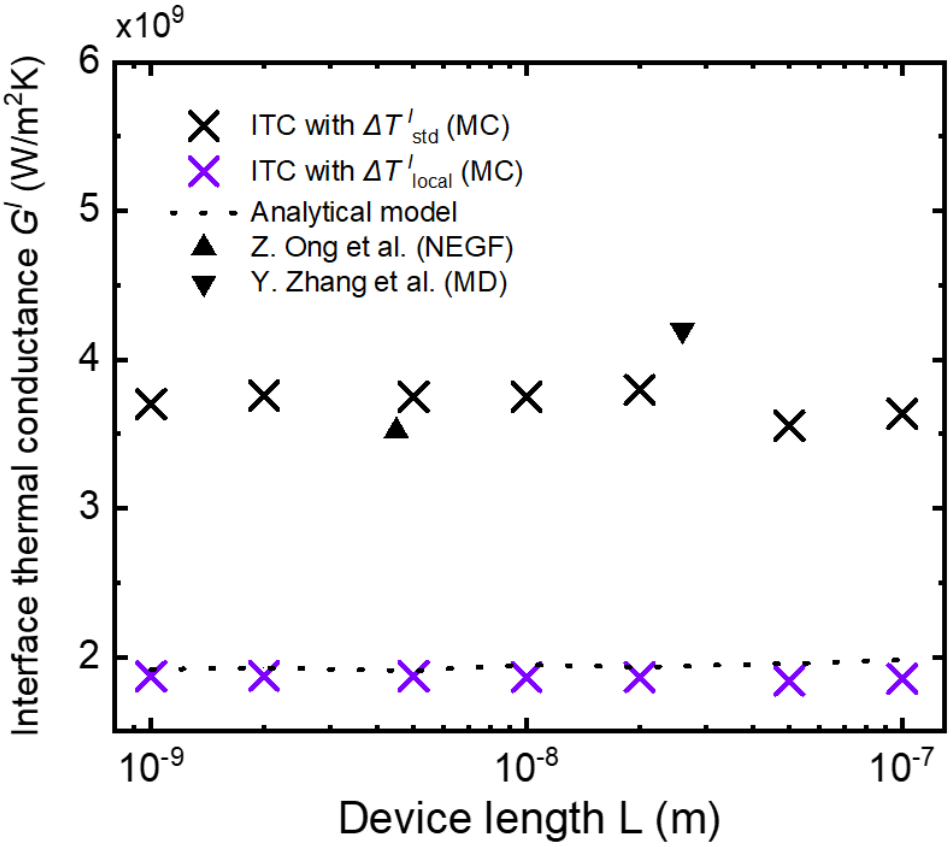

Figure A.4 Comparaison de la conductance thermique à l'interface (ITC) calculée en utilisant la différence de température standard (croix noires) et les températures directionnelles (croix violettes) en fonction de la longueur du dispositif. Le modèle analytique est représenté par la ligne pointillée, tandis que les résultats d'autres études utilisant des méthodes NEGF et MD sont indiqués par des triangles pour comparaison.

Grâce à l'analyse des taux moyens de diffusion des phonons, nous avons constaté que la diffusion normale domine sur la diffusion Umklapp à toutes les températures pour ces matériaux 2D, comme le montre la Figure A.3. De plus, des mélanges d'isotopes substantiels dans le h-BN et le MoS_2 entraînent une forte diffusion phonon-isotope comparable à la diffusion phonon-phonon à 300 K. La fiabilité de notre méthodologie de simulation est validée par le calcul de la conductivité thermique, qui est étroitement alignée avec les mesures expérimentales. Bien que de légères divergences soient observées dans le graphène, où les processus normaux dominent largement, la

précision globale est louable

Dans l'étude des hétérostructures latérales, il est montré que la température standard, basée sur les statistiques de Bose-Einstein, est insuffisante pour décrire avec précision le transfert de chaleur dans ces hétérostructures. Étant donné que les phonons sont particulièrement perturbés près de l'interface, où un régime de transport fortement hors équilibre est observé, la température standard ne parvient pas à capturer efficacement le comportement des phonons à l'interface. Pour y remédier, nous avons introduit le concept de températures directionnelles, qui permettent le calcul précis de la conductance thermique à l'interface (ITC). Notamment, les résultats obtenus en utilisant les températures directionnelles montrent une forte concordance avec le modèle analytique et n'affichent pas les variations dépendantes de la longueur observées avec les calculs de température standard, comme le montre la Figure A.4.

A.5 Reponse thermique transitoire dans des heterostructures 2D h-BN/Graphene de 100 nm

Enfin, nous avons présenté un examen détaillé de la réponse thermique transitoire dans des hétérostructures h-BN/graphène de 100 nm via des simulations Monte Carlo. L'étude est motivée par le fait que les fluctuations de température transitoires peuvent affecter de manière critique la fonctionnalité des dispositifs à l'échelle nanométrique.

L'étude analyse les propriétés thermiques transitoires à différents emplacements de l'hétérostructure, révélant que la densité du flux de chaleur initial est maximale près du thermostat chaud et que les trajectoires des phonons sont notablement perturbées aux interfaces durant le transitoire.

La Figure A.5 montre que le modèle semi-analytique proposé offre une représentation robuste de la densité du flux de chaleur transitoire basée sur les températures directionnelles, capturant efficacement non

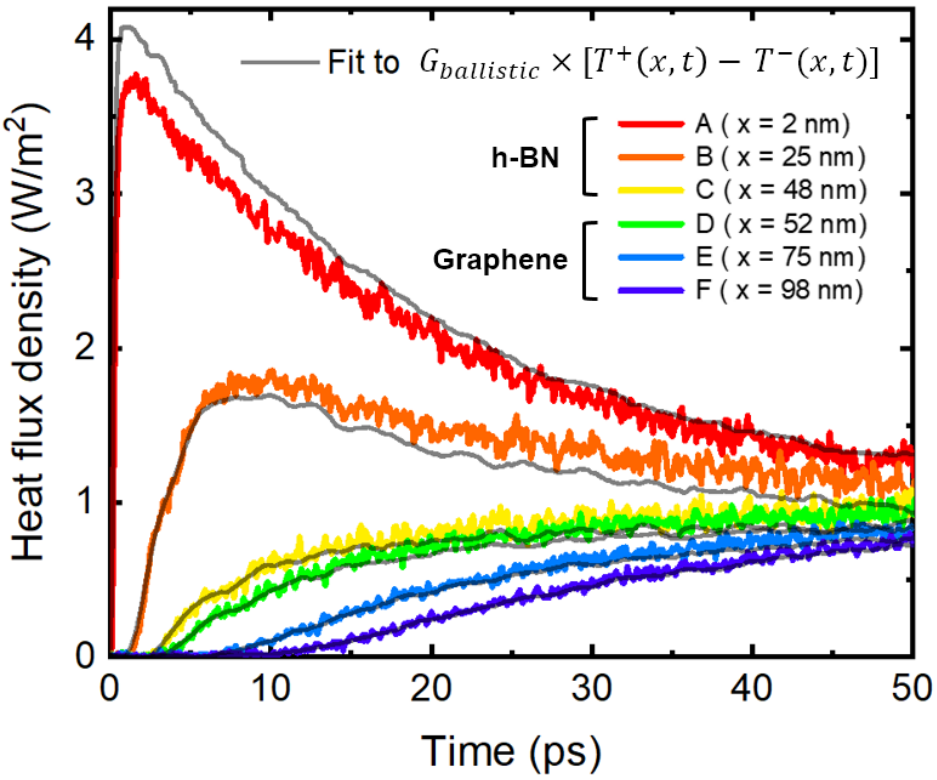

Figure A.5 Profils de densité du flux de chaleur aux positions A à F en fonction du temps pour une hétérostructure latérale 2D h-BN/graphène. La ligne grise continue représente un modèle semi-analytique.

seulement les changements initiaux rapides, mais aussi la transition du système vers l'état stationnaire.

En définissant les temps de relaxation, de retard et de montée, nous avons caractérisé le comportement thermique dynamique, observant que ces paramètres sont significativement affectés par la distance à la source de chaleur et les propriétés des matériaux. Notre étude a également examiné la densité du flux de chaleur transitoire par modes de phonons, notant l'impact prononcé des modes TA et ZA dans les régions de h-BN et de graphène, respectivement. Il est trouvé que l'impact de l'interface sur la réponse thermique transitoire est considérable, présentant une différence substantielle dans le temps de montée au sein de l'hétérostructure par rapport aux nanofilms homogènes.

Cette recherche peut fournir des informations critiques sur la dynamique thermique des dispositifs à l'échelle nanométrique, soulignant l'importance de l'analyse de la réponse transitoire et le rôle essentiel de l'architecture des dispositifs dans la gestion thermique pour la fiabilité des dispositifs.

A.6 CONCLUSION

Dans cette thèse, nous avons fait avancer la compréhension du transport des phonons dans les nanostructures grâce à une simulation Monte Carlo à bandes complètes. Tous les paramètres des matériaux, tels que les dispersions de phonons et les taux de dispersion, ont été calculés par des méthodes ab-initio. Cette recherche étend notre approche computationnelle précédente, initialement centrée sur le silicium, pour englober le GaAs et une variété de matériaux 2D, vérifiant ainsi la polyvalence et l'efficacité de notre code de simulation à travers différents systèmes de matériaux. De plus, un aspect unique de cette recherche réside dans le calcul précis des mécanismes de dispersion des phonons utilisant la DFT et la DFPT.

Nous avons conçu des nanofilms transversaux (CPNF), des nanofilms dans le plan (IPNF) et des nanofils (NW), notant la transition du transport balistique au transport diffusif avec des tailles de nanostructures diverses. Dans l'étude des propriétés thermiques des matériaux 2D, les résultats ont souligné que les processus de dispersion normaux sont prédominants, en particulier dans le graphène. Nous avons introduit le concept de températures directionnelles pour répondre aux limites de la mesure de température standard, en particulier près des interfaces dans les hétérostructures latérales. Cette innovation a facilité des calculs plus précis de la conductance thermique à l'interface. Nos simulations ont démontré que le comportement thermique transitoire différait significativement en fonction de la position et des contributions des modes. La réponse transitoire dans les structures avec interfaces a connu des retards notables, confirmant l'impact des interfaces sur le transport thermique.

BIBLIOGRAPHY

[1] M. J. Madou, *Fundamentals of Microfabrication* (CRC Press, 2018).

[2] H. Song, J. Liu, B. Liu, J. Wu, H. M. Cheng, and F. Kang, *Two-Dimensional Materials for Thermal Management Applications*, Joule **2**, 442 (2018).

[3] S. E. Thompson and S. Parthasarathy, *Moore's Law: The Future of Si Microelectronics*, Mater. Today **9**, (2006).

[4] T. Song, H. Kim, W. Rim, H. Jung, C. Park, I. Lee, S. Baek, and J. Jung, *A 3-Nm Gate-All-Around SRAM Featuring an Adaptive Dual-Bitline and an Adaptive Cell-Power Assist Circuit*, IEEE J. Solid-State Circuits **57**, (2022).

[5] Y. Lee, H. W. Jeong, S. H. Kim, K. Yang, and M. H. Park, *Effect of Stress on Fluorite-Structured Ferroelectric Thin Films for Semiconductor Devices*, Mater. Sci. Semicond. Process. **160**, (2023).

[6] J. Baek, Y. Elasser, K. Radhakrishnan, H. Gan, J. P. Douglas, H. K. Krishnamurthy, X. Li, S. Jiang, C. R. Sullivan, and M. Chen, *Vertical Stacked LEGO-PoL CPU Voltage Regulator*, IEEE Trans. Power Electron. **37**, (2022).

[7] H. F. Hamann, A. Weger, J. A. Lacey, Z. Hu, P. Bose, E. Cohen, and J. Wakil, *Hotspot-Limited Microprocessors: Direct Temperature and Power Distribution Measurements*, IEEE J. Solid-State Circuits **42**, (2007).

[8] J. M. Ziman, *Electrons and Phonons: The Theory of Transport Phenomena in Solids* (Oxford University Press, 2001).

[9] M. Nomura, R. Anufriev, Z. Zhang, J. Maire, Y. Guo, R. Yanagisawa, and S. Volz, *Review of Thermal Transport in Phononic Crystals*, Mater. Today Phys. **22**, (2022).

[10] Q. Zheng, M. Hao, R. Miao, J. Schaadt, and C. Dames, *Advances in Thermal Conductivity for Energy Applications: A Review*, Prog. Energy **3**, (2021).

[11] B. Cai, H. Hu, H. L. Zhuang, and J. F. Li, *Promising Materials for Thermoelectric Applications*, J. Alloys Compd. **806**, (2019).

[12] S. Singh, P. Dutta, M. Rathi, Y. Yao, Y. Gao, S. Sun, D. Khatiwada, V. Selvamanickam, and A. Mavrokefalos, *Enhanced Thermoelectric Performance in Single-Crystal-like Semiconducting Flexible GaAs Films*, APL Mater. **7**, 031104 (2019).

[13] S. Xie, H. Zhu, X. Zhang, and H. Wang, *A Brief Review on the Recent Development of Phonon Engineering and Manipulation at Nanoscales*, Int. J. Extrem. Manuf. **6**, 012007 (2023).

[14] H. Bao, J. Chen, X. Gu, and B. Cao, *A Review of Simulation Methods in Micro/Nanoscale Heat Conduction*, ES Energy Environ. **1**, 16 (2018).

[15] P. Siffert and E. F. Krimmel, *Silicon: Evolution and Future of a Technology*, Vol. 7 (Springer, 2004).

[16] H. S. Bennett, *Hole and Electron Mobilities in Heavily Doped Silicon: Comparison of Theory and Experiment*, Solid State Electron. **26**, (1983).

[17] C. Yang, C. J. Barrelet, F. Capasso, and C. M. Lieber, *Single P-Type/Intrinsic/n-Type Silicon Nanowires as Nanoscale Avalanche Photodetectors*, Nano Lett. **6**, (2006).

[18] Y. Cui, Z. Zhong, D. Wang, W. U. Wang, and C. M. Lieber, *High Performance Silicon Nanowire Field Effect Transistors*, Nano Lett. **3**, (2003).

[19] L. C. Andreani, A. Bozzola, P. Kowalczewski, M. Liscidini, and L. Redorici, *Silicon Solar Cells: Toward the Efficiency Limits*, Adv. Phys. X **4**, (2019).

[20] M. F. Gonzalez-Zalba, S. de Franceschi, E. Charbon, T. Meunier,

M. Vinet, and A. S. Dzurak, *Scaling Silicon-Based Quantum Computing Using CMOS Technology*, Nat. Electron. **4**, (2021).

[21] W. Bogaerts and L. Chrostowski, *Silicon Photonics Circuit Design: Methods, Tools and Challenges*, Laser Photonics Rev. **12**, (2018).

[22] S. Hassan, Humaira, and M. Asghar, *Limitation of Silicon Based Computation and Future Prospects*, in *2010 Second International Conference on Communication Software and Networks* (IEEE, 2010), pp. 559–561.

[23] R. W. Keyes, *Physical Limits of Silicon Transistors and Circuits*, Reports Prog. Phys. **68**, (2005).

[24] N. Jain and B. Raj, *An Analog and Digital Design Perspective Comprehensive Approach on Fin-FET (Fin-Field Effect Transistor) Technology—A Review*, Rev. Adv. Sci. Eng. **5**, (2017).

[25] N. Loubet et al., *Stacked Nanosheet Gate-All-around Transistor to Enable Scaling beyond FinFET*, in *2017 Symposium on VLSI Technology* (IEEE, 2017), pp. T230–T231.

[26] G. Sun, *Intersubband Approach to Silicon Based Lasers—Circumventing the Indirect Bandgap Limitation*, Adv. Opt. Photonics **3**, (2011).

[27] X. K. Chen, Y. J. Zeng, and K. Q. Chen, *Thermal Transport in Two-Dimensional Heterostructures*, Front. Mater. **7**, 427 (2020).

[28] M. H. Kalantari and X. Zhang, *Thermal Transport in 2D Materials*, Nanomaterials **13**, 117 (2022).

[29] S. Poncé, W. Li, S. Reichardt, and F. Giustino, *First-Principles Calculations of Charge Carrier Mobility and Conductivity in Bulk Semiconductors and Two-Dimensional Materials*, Reports Prog. Phys. **83**, 036501 (2020).

[30] H. Kim, A. Amarnath, J. Bagherzadeh, N. Talati, and R. G. Dreslinski, *A Survey Describing beyond Si Transistors and Exploring Their Implications for Future Processors*, ACM J. Emerg.

Technol. Comput. Syst. **17**, (2021).

[31] J. Yoon et al., *GaAs Photovoltaics and Optoelectronics Using Releasable Multilayer Epitaxial Assemblies*, Nature **465**, (2010).

[32] T. Patrick Xiao, K. Chen, P. Santhanam, S. Fan, and E. Yablonovitch, *Electroluminescent Refrigeration by Ultra-Efficient GaAs Light-Emitting Diodes*, J. Appl. Phys. **123**, (2018).

[33] V. K. Khanna, *The Temperature-Sustaining Capability of Gallium Arsenide Electronics*, in *Extreme-Temperature and Harsh-Environment Electronics* (IOP Publishing, 2017).

[34] M. G. Holland, *Phonon Scattering in Semiconductors From Thermal Conductivity Studies*, Phys. Rev. **134**, A471 (1964).

[35] R. O. Carlson, G. A. Slack, and S. J. Silverman, *Thermal Conductivity of GaAs and GaAs1-XPx Laser Semiconductors*, J. Appl. Phys. **36**, 505 (1965).

[36] X. Zou, X. Chen, H. Huang, Y. Xu, and W. Duan, *Enhanced Thermoelectric Figure of Merit in Thin GaAs Nanowires*, Nanoscale **7**, (2015).

[37] N. Arora, D. P. Joshi, and U. Pachauri, *Effect of Size and Dimension Dependent Specific Heat on Thermal Conductivity of Nanostructured Semiconductors*, Mater. Chem. Phys. **217**, (2018).

[38] P. N. Martin, Z. Aksamija, E. Pop, and U. Ravaioli, *Reduced Thermal Conductivity in Nanoengineered Rough Ge and GaAs Nanowires*, Nano Lett. **10**, (2010).

[39] A. V. Inyushkin, A. N. Taldenkov, A. Y. Yakubovsky, A. V. Markov, L. Moreno-Garsia, and B. N. Sharonov, *Thermal Conductivity of Isotopically Enriched 71GaAs Crystal*, Semicond. Sci. Technol. **18**, 685 (2003).

[40] J. Walia, N. Dhindsa, J. Flannery, I. Khodabad, J. Forrest, R. Lapierre, and S. S. Saini, *Enhanced Photothermal Conversion in Vertically Oriented Gallium Arsenide Nanowire Arrays*, Nano

Lett. **14**, (2014).

[41] M. N. Luckyanova et al., *Coherent Phonon Heat Conduction in Superlattices*, Science. **338**, 936 (2012).

[42] A. Ghukasyan, P. Oliveira, N. I. Goktas, and R. Lapierre, *Thermal Conductivity of GaAs Nanowire Arrays Measured by the 3ω Method*, Nanomaterials **12**, (2022).

[43] M. Soini, I. Zardo, E. Uccelli, S. Funk, G. Koblmüller, A. Fontcuberta I Morral, and G. Abstreiter, *Thermal Conductivity of GaAs Nanowires Studied by Micro-Raman Spectroscopy Combined with Laser Heating*, Appl. Phys. Lett. **97**, (2010).

[44] I. Zardo, S. Conesa-Boj, F. Peiro, J. R. Morante, J. Arbiol, E. Uccelli, G. Abstreiter, and A. Fontcuberta I Morral, *Raman Spectroscopy of Wurtzite and Zinc-Blende GaAs Nanowires: Polarization Dependence, Selection Rules, and Strain Effects*, Phys. Rev. B - Condens. Matter Mater. Phys. **80**, (2009).

[45] T. F. Kuech, *III-V Compound Semiconductors: Growth and Structures*, Prog. Cryst. Growth Charact. Mater. **62**, 352 (2016).

[46] D. S. Katzer and M. Cardona, *Thermal-Conductivity Measurements of Gaas/Alas Superlattices Using a Picosecond Optical Pump-and-Probe Technique*, Phys. Rev. B - Condens. Matter Mater. Phys. **59**, (1999).

[47] M. N. Luckyanova, J. A. Johnson, A. A. Maznev, J. Garg, A. Jandl, M. T. Bulsara, E. A. Fitzgerald, K. A. Nelson, and G. Chen, *Anisotropy of the Thermal Conductivity in GaAs/AlAs Superlattices*, Nano Lett. **13**, (2013).

[48] T. Juntunen, T. Koskinen, V. Khayrudinov, T. Haggren, H. Jiang, H. Lipsanen, and I. Tittonen, *Thermal Conductivity Suppression in GaAs-AlAs Core-Shell Nanowire Arrays*, Nanoscale **11**, 20507 (2019).

[49] D. Strauch and B. Dorner, *Phonon Dispersion in GaAs*, J. Phys. Condens. Matter **2**, 1457 (1990).

[50] J. Shah, R. C. C. Leite, and J. F. Scott, *Photoexcited Hot LO Phonons in GaAs*, Solid State Commun. **8**, (1970).

[51] F. Vallée and F. Bogani, *Coherent Time-Resolved Investigation of LO-Phonon Dynamics in GaAs*, Phys. Rev. B **43**, (1991).

[52] H. Hamzeh and F. Aniel, *Monte Carlo Study of Phonon Dynamics in III-V Compounds*, J. Appl. Phys. **109**, (2011).

[53] L. Lindsay, D. A. Broido, and T. L. Reinecke, *Ab Initio Thermal Transport in Compound Semiconductors*, Phys. Rev. B - Condens. Matter Mater. Phys. **87**, 165201 (2013).

[54] Z. Sun, K. Yuan, X. Zhang, and D. Tang, *Pressure Tuning of the Thermal Conductivity of Gallium Arsenide from First-Principles Calculations*, Phys. Chem. Chem. Phys. **20**, 30331 (2018).

[55] T. Luo, J. Garg, J. Shiomi, K. Esfarjani, and G. Chen, *Gallium Arsenide Thermal Conductivity and Optical Phonon Relaxation Times from First-Principles Calculations*, Europhys. Lett. **101**, 16001 (2013).

[56] T. H. Liu, J. Zhou, B. Liao, D. J. Singh, and G. Chen, *First-Principles Mode-by-Mode Analysis for Electron-Phonon Scattering Channels and Mean Free Path Spectra in GaAs*, Phys. Rev. B **95**, (2017).

[57] K. S. Novoselov, A. K. Geim, S. V. Morozov, D. Jiang, Y. Zhang, S. V. Dubonos, I. V. Grigorieva, and A. A. Firsov, *Electric Field in Atomically Thin Carbon Films*, Science. **306**, (2004).

[58] N. Mounet et al., *Two-Dimensional Materials from High-Throughput Computational Exfoliation of Experimentally Known Compounds*, Nat. Nanotechnol. **13**, 246 (2018).

[59] Y. Wang, N. Xu, D. Li, and J. Zhu, *Thermal Properties of Two Dimensional Layered Materials*, Adv. Funct. Mater. **27**, (2017).

[60] A. H. Castro Neto, F. Guinea, N. M. R. Peres, K. S. Novoselov, and A. K. Geim, *The Electronic Properties of Graphene*, Rev. Mod. Phys. **81**, (2009).

[61] A. A. Balandin, S. Ghosh, W. Bao, I. Calizo, D. Teweldebrhan, F. Miao, and C. N. Lau, *Superior Thermal Conductivity of Single-Layer Graphene*, Nano Lett. **8**, (2008).

[62] W. Cai, A. L. Moore, Y. Zhu, X. Li, S. Chen, L. Shi, and R. S. Ruoff, *Thermal Transport in Suspended and Supported Monolayer Graphene Grown by Chemical Vapor Deposition*, Nano Lett. **10**, 1645 (2010).

[63] S. Chen et al., *Raman Measurements of Thermal Transport in Suspended Monolayer Graphene of Variable Sizes in Vacuum and Gaseous Environments*, ACS Nano **5**, (2011).

[64] J. U. Lee, D. Yoon, H. Kim, S. W. Lee, and H. Cheong, *Thermal Conductivity of Suspended Pristine Graphene Measured by Raman Spectroscopy*, Phys. Rev. B - Condens. Matter Mater. Phys. **83**, (2011).

[65] Q. Y. Li, K. Xia, J. Zhang, Y. Zhang, Q. Li, K. Takahashi, and X. Zhang, *Measurement of Specific Heat and Thermal Conductivity of Supported and Suspended Graphene by a Comprehensive Raman Optothermal Method*, Nanoscale **9**, (2017).

[66] X. Xu et al., *Length-Dependent Thermal Conductivity in Suspended Single-Layer Graphene*, Nat. Commun. **5**, (2014).

[67] S. Lee, D. Broido, K. Esfarjani, and G. Chen, *Hydrodynamic Phonon Transport in Suspended Graphene*, Nat. Commun. **6**, (2015).

[68] G. Fugallo, A. Cepellotti, L. Paulatto, M. Lazzeri, N. Marzari, and F. Mauri, *Thermal Conductivity of Graphene and Graphite: Collective Excitations and Mean Free Paths*, Nano Lett. **14**, 6109 (2014).

[69] A. Cepellotti, G. Fugallo, L. Paulatto, M. Lazzeri, F. Mauri, and N. Marzari, *Phonon Hydrodynamics in Two-Dimensional Materials*, Nat. Commun. **6**, (2015).

[70] D. L. Nika, S. Ghosh, E. P. Pokatilov, and A. A. Balandin, *Lattice*

Thermal Conductivity of Graphene Flakes: Comparison with Bulk Graphite, Appl. Phys. Lett. **94**, (2009).

[71] L. Lindsay, D. A. Broido, and N. Mingo, *Flexural Phonons and Thermal Transport in Graphene*, Phys. Rev. B - Condens. Matter Mater. Phys. **82**, (2010).

[72] J. H. Seol et al., *Two-Dimensional Phonon Transport in Supported Graphene*, Science. **328**, (2010).

[73] W. Jang, Z. Chen, W. Bao, C. N. Lau, and C. Dames, *Thickness-Dependent Thermal Conductivity of Encased Graphene and Ultrathin Graphite*, Nano Lett. **10**, (2010).

[74] S. Ghosh, I. Calizo, D. Teweldebrhan, E. P. Pokatilov, D. L. Nika, A. A. Balandin, W. Bao, F. Miao, and C. N. Lau, *Extremely High Thermal Conductivity of Graphene: Prospects for Thermal Management Applications in Nanoelectronic Circuits*, Appl. Phys. Lett. **92**, (2008).

[75] P. Dollfus, V. H. Nguyen, and J. Saint-Martin, *Thermoelectric Effects in Graphene Nanostructures*, J. Phys. Condens. Matter **27**, (2015).

[76] J. Wang, F. Ma, and M. Sun, *Graphene, Hexagonal Boron Nitride, and Their Heterostructures: Properties and Applications*, RSC Adv. **7**, 16801 (2017).

[77] A. Falin et al., *Mechanical Properties of Atomically Thin Boron Nitride and the Role of Interlayer Interactions*, Nat. Commun. **8**, (2017).

[78] I. Aharonovich, J.-P. Tetienne, and M. Toth, *Quantum Emitters in Hexagonal Boron Nitride*, Nano Lett. **22**, 9227 (2022).

[79] J. Meng, D. Wang, L. Cheng, M. Gao, and X. Zhang, *Recent Progress in Synthesis, Properties, and Applications of Hexagonal Boron Nitride-Based Heterostructures*, Nanotechnology **30**, (2019).

[80] A. Simpson and A. D. Stuckes, *The Thermal Conductivity of*

Highly Oriented Pyrolytic Boron Nitride, J. Phys. C Solid State Phys. **4**, (1971).

[81] E. K. Sichel, R. E. Miller, M. S. Abrahams, and C. J. Buiocchi, *Heat Capacity and Thermal Conductivity of Hexagonal Pyrolytic Boron Nitride*, Phys. Rev. B **13**, 4607 (1976).

[82] N. Alem, R. Erni, C. Kisielowski, M. D. Rossell, W. Gannett, and A. Zettl, *Atomically Thin Hexagonal Boron Nitride Probed by Ultrahigh-Resolution Transmission Electron Microscopy*, Phys. Rev. B - Condens. Matter Mater. Phys. **80**, (2009).

[83] L. Lindsay and D. A. Broido, *Enhanced Thermal Conductivity and Isotope Effect in Single-Layer Hexagonal Boron Nitride*, Phys. Rev. B - Condens. Matter Mater. Phys. **84**, (2011).

[84] I. Jo, M. T. Pettes, J. Kim, K. Watanabe, T. Taniguchi, Z. Yao, and L. Shi, *Thermal Conductivity and Phonon Transport in Suspended Few-Layer Hexagonal Boron Nitride*, Nano Lett. **13**, (2013).

[85] H. Zhou et al., *High Thermal Conductivity of Suspended Few-Layer Hexagonal Boron Nitride Sheets*, Nano Res. **7**, (2014).

[86] C. Wang, J. Guo, L. Dong, A. Aiyiti, X. Xu, and B. Li, *Superior Thermal Conductivity in Suspended Bilayer Hexagonal Boron Nitride*, Sci. Rep. **6**, (2016).

[87] Q. Cai, D. Scullion, W. Gan, A. Falin, S. Zhang, K. Watanabe, T. Taniguchi, Y. Chen, E. J. G. Santos, and L. H. Li, *High Thermal Conductivity of High-Quality Monolayer Boron Nitride and Its Thermal Expansion*, Sci. Adv. **5**, (2019).

[88] A. E. Naclerio and P. R. Kidambi, *A Review of Scalable Hexagonal Boron Nitride (H-BN) Synthesis for Present and Future Applications*, Adv. Mater. **35**, (2023).

[89] S. Manzeli, D. Ovchinnikov, D. Pasquier, O. V. Yazyev, and A. Kis, *2D Transition Metal Dichalcogenides*, Nat. Rev. Mater. **2**, (2017).

[90] P. Joensen, R. F. Frindt, and S. R. Morrison, *Single-Layer MoS2*, Mater. Res. Bull. **21**, 457 (1986).

[91] J. N. Coleman et al., *Two-Dimensional Nanosheets Produced by Liquid Exfoliation of Layered Materials*, Science. **331**, (2011).

[92] W. Zhao, Z. Ghorannevis, L. Chu, M. Toh, C. Kloc, P. H. Tan, and G. Eda, *Evolution of Electronic Structure in Atomically Thin Sheets of Ws 2 and Wse2*, ACS Nano **7**, (2013).

[93] K. F. Mak, C. Lee, J. Hone, J. Shan, and T. F. Heinz, *Atomically Thin MoS2: A New Direct-Gap Semiconductor*, Phys. Rev. Lett. **105**, (2010).

[94] Q. H. Wang, K. Kalantar-Zadeh, A. Kis, J. N. Coleman, and M. S. Strano, *Electronics and Optoelectronics of Two-Dimensional Transition Metal Dichalcogenides*, Nat. Nanotechnol. **7**, 699 (2012).

[95] J. K. Ellis, M. J. Lucero, and G. E. Scuseria, *The Indirect to Direct Band Gap Transition in Multilayered MoS2 as Predicted by Screened Hybrid Density Functional Theory*, Appl. Phys. Lett. **99**, (2011).

[96] S. Sahoo, A. P. S. Gaur, M. Ahmadi, M. J. F. Guinel, and R. S. Katiyar, *Temperature-Dependent Raman Studies and Thermal Conductivity of Few-Layer MoS2*, J. Phys. Chem. C **117**, (2013).

[97] X. Zhang, D. Sun, Y. Li, G. H. Lee, X. Cui, D. Chenet, Y. You, T. F. Heinz, and J. C. Hone, *Measurement of Lateral and Interfacial Thermal Conductivity of Single- and Bilayer MoS2 and MoSe2 Using Refined Optothermal Raman Technique*, ACS Appl. Mater. Interfaces **7**, 25923 (2015).

[98] W. Li, J. Carrete, and N. Mingo, *Thermal Conductivity and Phonon Linewidths of Monolayer MoS2 from First Principles*, Appl. Phys. Lett. **103**, (2013).

[99] X. Gu, B. Li, and R. Yang, *Layer Thickness-Dependent Phonon Properties and Thermal Conductivity of MoS2*, J. Appl. Phys. **119**, (2016).

[100] Y. Hong, J. Zhang, and X. C. Zeng, *Thermal Conductivity of*

Monolayer MoSe2 and MoS2, J. Phys. Chem. C **120**, (2016).

[101] Z. Wang, Q. Li, Y. Chen, B. Cui, Y. Li, F. Besenbacher, and M. Dong, *The Ambipolar Transport Behavior of WSe2 Transistors and Its Analogue Circuits*, NPG Asia Mater. **10**, (2018).

[102] Y. Zhang et al., *Electronic Structure, Surface Doping, and Optical Response in Epitaxial WSe2 Thin Films*, Nano Lett. **16**, (2016).

[103] M. R. Jobayr and E. M. T. Salman, *Investigation of the Thermoelectric Properties of One-Layer Transition Metal Dichalcogenides*, Chinese J. Phys. **74**, (2021).

[104] S. Kumar and U. Schwingenschlögl, *Thermoelectric Response of Bulk and Monolayer MoSe2 and WSe2*, Chem. Mater. **27**, 1278 (2015).

[105] E. Easy, Y. Gao, Y. Wang, D. Yan, S. M. Goushehgir, E. H. Yang, B. Xu, and X. Zhang, *Experimental and Computational Investigation of Layer-Dependent Thermal Conductivities and Interfacial Thermal Conductance of One-To Three-Layer WSe2*, ACS Appl. Mater. Interfaces **13**, 13063 (2021).

[106] N. Peimyoo, J. Shang, W. Yang, Y. Wang, C. Cong, and T. Yu, *Thermal Conductivity Determination of Suspended Mono- and Bilayer WS2 by Raman Spectroscopy*, Nano Res. **8**, (2015).

[107] Z. Yan, C. Jiang, T. R. Pope, C. F. Tsang, J. L. Stickney, P. Goli, J. Renteria, T. T. Salguero, and A. A. Balandin, *Phonon and Thermal Properties of Exfoliated TaSe2 Thin Films*, J. Appl. Phys. **114**, (2013).

[108] C. Muratore et al., *Cross-Plane Thermal Properties of Transition Metal Dichalcogenides*, Appl. Phys. Lett. **102**, (2013).

[109] J. Liu, G. M. Choi, and D. G. Cahill, *Measurement of the Anisotropic Thermal Conductivity of Molybdenum Disulfide by the Time-Resolved Magneto-Optic Kerr Effect*, J. Appl. Phys. **116**, (2014).

[110] K. Nakamura, N. Nagamura, K. Ueno, T. Taniguchi, K. Watanabe,

and K. Nagashio, *All 2D Heterostructure Tunnel Field-Effect Transistors: Impact of Band Alignment and Heterointerface Quality*, ACS Appl. Mater. Interfaces **12**, (2020).

[111] C. C. Chen, Z. Li, L. Shi, and S. B. Cronin, *Thermoelectric Transport across Graphene/Hexagonal Boron Nitride/Graphene Heterostructures*, Nano Res. **8**, (2015).

[112] S. Garg, J. P. Fix, A. V. Krayev, C. Flanery, M. Colgrove, A. R. Sulkanen, M. Wang, G. Y. Liu, N. J. Borys, and P. Kung, *Nanoscale Raman Characterization of a 2D Semiconductor Lateral Heterostructure Interface*, ACS Nano **16**, (2022).

[113] Z. Cai, B. Liu, X. Zou, and H.-M. Cheng, *Chemical Vapor Deposition Growth and Applications of Two-Dimensional Materials and Their Heterostructures*, Chem. Rev. **118**, 6091 (2018).

[114] H. Qi, L. Wang, J. Sun, Y. Long, P. Hu, F. Liu, and X. He, *Production Methods of Van Der Waals Heterostructures Based on Transition Metal Dichalcogenides*, Crystals **8**, 35 (2018).

[115] D. S. Koda, F. Bechstedt, M. Marques, and L. K. Teles, *Coincidence Lattices of 2D Crystals: Heterostructure Predictions and Applications*, J. Phys. Chem. C **120**, (2016).

[116] H. Guo, Z. Hu, Z. Liu, and J. Tian, *Stacking of 2D Materials*, Adv. Funct. Mater. **31**, (2021).

[117] J. Li et al., *General Synthesis of Two-Dimensional van Der Waals Heterostructure Arrays*, Nature **579**, (2020).

[118] Y. Gong et al., *Vertical and In-Plane Heterostructures from WS2/MoS2 Monolayers*, Nat. Mater. 2014 1312 **13**, 1135 (2014).

[119] P. Sutter, R. Cortes, J. Lahiri, and E. Sutter, *Interface Formation in Monolayer Graphene-Boron Nitride Heterostructures*, Nano Lett. **12**, 4869 (2012).

[120] Z. Liu et al., *In-Plane Heterostructures of Graphene and Hexagonal Boron Nitride with Controlled Domain Sizes*, Nat.

Nanotechnol. **8**, (2013).

[121] Z. Y. Ong, G. Zhang, and Y. W. Zhang, *Controlling the Thermal Conductance of Graphene/h-BN Lateral Interface with Strain and Structure Engineering*, Phys. Rev. B **93**, (2016).

[122] Y. Hong, J. Zhang, and X. C. Zeng, *Thermal Contact Resistance across a Linear Heterojunction within a Hybrid Graphene/Hexagonal Boron Nitride Sheet*, Phys. Chem. Chem. Phys. **18**, (2016).

[123] T. Feng, W. Yao, Z. Wang, J. Shi, C. Li, B. Cao, and X. Ruan, *Spectral Analysis of Nonequilibrium Molecular Dynamics: Spectral Phonon Temperature and Local Nonequilibrium in Thin Films and across Interfaces*, Phys. Rev. B **95**, (2017).

[124] X. Liu, J. Gao, G. Zhang, and Y. W. Zhang, *MoS2-Graphene in-Plane Contact for High Interfacial Thermal Conduction*, Nano Res. **10**, (2017).

[125] M. Y. Li et al., *Epitaxial Growth of a Monolayer WSe2-MoS2 Lateral p-n Junction with an Atomically Sharp Interface*, Science. **349**, (2015).

[126] H. Qin, Q. X. Pei, Y. Liu, and Y. W. Zhang, *The Mechanical and Thermal Properties of MoS2-WSe2 Lateral Heterostructures*, Phys. Chem. Chem. Phys. **21**, 15845 (2019).

[127] R. Frisenda, E. Navarro-Moratalla, P. Gant, D. Pérez De Lara, P. Jarillo-Herrero, R. V. Gorbachev, and A. Castellanos-Gomez, *Recent Progress in the Assembly of Nanodevices and van Der Waals Heterostructures by Deterministic Placement of 2D Materials*, Chem. Soc. Rev. **47**, 53 (2018).

[128] I. H. Abidi et al., *New Approach to Unveiling Individual Atomic Layers of 2D Materials and Their Heterostructures*, Chem. Mater. **30**, (2018).

[129] Y. Ding et al., *Stacking-Mode Confined Growth of 2H-MoTe2/MoS2 Bilayer Heterostructures for UV–Vis–IR*

Photodetectors, Nano Energy **49**, (2018).

[130] C. C. Chen, Z. Li, L. Shi, and S. B. Cronin, *Thermal Interface Conductance across a Graphene/Hexagonal Boron Nitride Heterojunction*, Appl. Phys. Lett. **104**, (2014).

[131] A. J. Pak and G. S. Hwang, *Theoretical Analysis of Thermal Transport in Graphene Supported on Hexagonal Boron Nitride: The Importance of Strong Adhesion Due to π -Bond Polarization*, Phys. Rev. Appl. **6**, (2016).

[132] Z. Zhang, S. Hu, J. Chen, and B. Li, *Hexagonal Boron Nitride: A Promising Substrate for Graphene with High Heat Dissipation*, Nanotechnology **28**, (2017).

[133] J. Jung, Z. Qiao, Q. Niu, and A. H. MacDonald, *Transport Properties of Graphene Nanoroads in Boron Nitride Sheets*, Nano Lett. **12**, (2012).

[134] J. J. Ma, J. J. Zheng, X. L. Zhu, P. F. Liu, W. D. Li, and B. T. Wang, *First-Principles Calculations of Thermal Transport Properties in MoS2/MoSe2 Bilayer Heterostructure*, Phys. Chem. Chem. Phys. **21**, (2019).

[135] Y. Liu et al., *Thermal Conductance of the 2D MoS2/h-BN and Graphene/h-BN Interfaces*, Sci. Rep. **7**, (2017).

[136] T. Bodineau, I. Gallagher, and L. Saint-Raymond, *A Microscopic View of the Fourier Law*, Comptes Rendus. Phys. **20**, 402 (2019).

[137] F. Bonetto, Joel L. Lebowitz, and Luc Rey-Bellet, *Fourier's Law: A Challenge to Theorists*, in *Mathematical Physics 2000* (Imperial College Press, 2000), pp. 128–150.

[138] G. Chen, *Non-Fourier Phonon Heat Conduction at the Microscale and Nanoscale*, Nat. Rev. Phys. **3**, 555 (2021).

[139] J. Lee, J. Lim, and P. Yang, *Ballistic Phonon Transport in Holey Silicon*, Nano Lett. **15**, 3273 (2015).

[140] R. Hanus, A. Garg, and G. J. Snyder, *Phonon Diffraction and*

Dimensionality Crossover in Phonon-Interface Scattering, Commun. Phys. **1**, (2018).

[141] R. B. Wilson and D. G. Cahill, *Anisotropic Failure of Fourier Theory in Time-Domain Thermoreflectance Experiments*, Nat. Commun. **5**, (2014).

[142] J. P. Caltagirone, *Non-Fourier Heat Transfer at Small Scales of Time and Space*, Int. J. Heat Mass Transf. **160**, (2020).

[143] R. Kovács and P. Rogolino, *Numerical Treatment of Nonlinear Fourier and Maxwell-Cattaneo-Vernotte Heat Transport Equations*, Int. J. Heat Mass Transf. **150**, (2020).

[144] A. Singh and E. B. Tadmor, *Thermal Parameter Identification for Non-Fourier Heat Transfer from Molecular Dynamics*, J. Comput. Phys. **299**, (2015).

[145] D. Terris, K. Joulain, D. Lacroix, and D. Lemonnier, *Numerical Simulation of Transient Phonon Heat Transfer in Silicon Nanowires and Nanofilms*, J. Phys. Conf. Ser. **92**, (2007).

[146] Y. Guo and M. Wang, *Phonon Hydrodynamics and Its Applications in Nanoscale Heat Transport*, Phys. Rep. **595**, 1 (2015).

[147] H. Rezgui, F. Nasri, M. F. Ben Aissa, and A. A. Guizani, *Investigation of Nanoscale Heat Transport in Sub-10 Nm Carbon Nanotube Field-Effect Transistors Based on the Finite Element Method*, Therm. Sci. Eng. Prog. **25**, (2021).

[148] K. Burke and L. O. Wagner, *DFT in a Nutshell*, Int. J. Quantum Chem. **113**, 96 (2013).

[149] S. Baroni, P. Giannozzi, and A. Testa, *Greens-Function Approach to Linear Response in Solids*, Phys. Rev. Lett. **58**, (1987).

[150] L. Paulatto, F. Mauri, and M. Lazzeri, *Anharmonic Properties from a Generalized Third-Order Ab Initio Approach: Theory and Applications to Graphite and Graphene*, Phys. Rev. B - Condens. Matter Mater. Phys. **87**, (2013).

[151] P. Giannozzi et al., *Advanced Capabilities for Materials Modelling with Quantum ESPRESSO*, J. Phys. Condens. Matter **29**, (2017).

[152] X. Gonze et al., *First-Principles Computation of Material Properties: The ABINIT Software Project*, Comput. Mater. Sci. **25**, (2002).

[153] G. Kresse and J. Furthmüller, *Efficient Iterative Schemes for Ab Initio Total-Energy Calculations Using a Plane-Wave Basis Set*, Phys. Rev. B - Condens. Matter Mater. Phys. **54**, (1996).

[154] J. Garg, N. Bonini, B. Kozinsky, and N. Marzari, *Role of Disorder and Anharmonicity in the Thermal Conductivity of Silicon-Germanium Alloys: A First-Principles Study*, Phys. Rev. Lett. **106**, (2011).

[155] Z. Tian, K. Esfarjani, J. Shiomi, A. S. Henry, and G. Chen, *On the Importance of Optical Phonons to Thermal Conductivity in Nanostructures*, Appl. Phys. Lett. **99**, (2011).

[156] W. Li, N. Mingo, L. Lindsay, D. A. Broido, D. A. Stewart, and N. A. Katcho, *Thermal Conductivity of Diamond Nanowires from First Principles*, Phys. Rev. B - Condens. Matter Mater. Phys. **85**, (2012).

[157] X. Gu and R. Yang, *Phonon Transport in Single-Layer Transition Metal Dichalcogenides: A First-Principles Study*, Appl. Phys. Lett. **105**, 131903 (2014).

[158] L. V. Keldysh, *Diagram Technique for Nonequilibrium Processes*, in *Selected Papers of Leonid V Keldysh* (World Scientific, 2023), pp. 47–55.

[159] S. Smidstrup et al., *QuantumATK: An Integrated Platform of Electronic and Atomic-Scale Modelling Tools*, J. Phys. Condens. Matter **32**, (2020).

[160] G. Tatara, H. Kohno, and J. Shibata, *Microscopic Approach to Current-Driven Domain Wall Dynamics*, Phys. Rep. **468**, 213 (2008).

[161] Z. Zeng, B. Li, Z. Zeng, and F. Claro, *Electronic Transport in Hybrid Mesoscopic Structures: A Nonequilibrium Green Function Approach*, Phys. Rev. B - Condens. Matter Mater. Phys. **68**, (2003).

[162] N. Mingo, *Calculation of Si Nanowire Thermal Conductivity Using Complete Phonon Dispersion Relations*, Phys. Rev. B - Condens. Matter Mater. Phys. **68**, (2003).

[163] X. F. Peng and K. Q. Chen, *Thermal Transport for Flexural and In-Plane Phonons in Graphene Nanoribbons*, Carbon N. Y. **77**, (2014).

[164] J. He, D. Li, Y. Ying, C. Feng, J. He, C. Zhong, H. Zhou, P. Zhou, and G. Zhang, *Orbitally Driven Giant Thermal Conductance Associated with Abnormal Strain Dependence in Hydrogenated Graphene-like Borophene*, Npj Comput. Mater. **5**, (2019).

[165] Z. Tian, K. Esfarjani, and G. Chen, *Enhancing Phonon Transmission across a Si/Ge Interface by Atomic Roughness: First-Principles Study with the Green's Function Method*, Phys. Rev. B - Condens. Matter Mater. Phys. **86**, (2012).

[166] X. F. Peng, X. Zhou, S. H. Tan, X. J. Wang, L. Q. Chen, and K. Q. Chen, *Thermal Conductance in Graphene Nanoribbons Modulated by Defects and Alternating Boron-Nitride Structures*, Carbon N. Y. **113**, (2017).

[167] A. Thakur and N. Sarkar, *A Tutorial on the NEGF Method for Electron Transport in Devices and Defective Materials*, Eur. Phys. J. B **96**, 113 (2023).

[168] M. Ye, X. Jiang, S. S. Li, and L. W. Wang, *Large-Scale First-Principles Quantum Transport Simulations Using Plane Wave Basis Set on High Performance Computing Platforms*, Comput. Phys. Commun. **260**, (2021).

[169] M. Luisier, *Atomistic Modeling of Anharmonic Phonon-Phonon Scattering in Nanowires*, Phys. Rev. B - Condens. Matter Mater. Phys. **86**, (2012).

[170] Y. Lee, M. Bescond, D. Logoteta, N. Cavassilas, M. Lannoo, and M. Luisier, *Anharmonic Phonon-Phonon Scattering Modeling of Three-Dimensional Atomistic Transport: An Efficient Quantum Treatment*, Phys. Rev. B **97**, (2018).

[171] Y. Guo, M. Bescond, Z. Zhang, M. Luisier, M. Nomura, and S. Volz, *Quantum Mechanical Modeling of Anharmonic Phonon-Phonon Scattering in Nanostructures*, Phys. Rev. B **102**, (2020).

[172] X. Gu, Z. Fan, and H. Bao, *Thermal Conductivity Prediction by Atomistic Simulation Methods: Recent Advances and Detailed Comparison*, J. Appl. Phys. **130**, (2021).

[173] Y. H. Lee, R. Biswas, C. M. Soukoulis, C. Z. Wang, C. T. Chan, and K. M. Ho, *Molecular-Dynamics Simulation of Thermal Conductivity in Amorphous Silicon*, Phys. Rev. B **43**, (1991).

[174] T. Yamamoto, S. Ohnishi, Y. Chen, and S. Iwata, *Effective Interatomic Potentials Based on the First Principles Material Database*, Data Sci. J. **8**, (2009).

[175] S. G. Volz and G. Chen, *Molecular-Dynamics Simulation of Thermal Conductivity of Silicon Crystals*, Phys. Rev. B - Condens. Matter Mater. Phys. **61**, (2000).

[176] Z. Zhong, X. Wang, and J. Xu, *Equilibrium Molecular Dynamics Study of Phonon Thermal Transport in Nanomaterials*, Numer. Heat Transf. Part B Fundam. **46**, (2004).

[177] A. S. Henry and G. Chen, *Spectral Phonon Transport Properties of Silicon Based on Molecular Dynamics Simulations and Lattice Dynamics*, J. Comput. Theor. Nanosci. **5**, (2008).

[178] C. Sevik, A. Kinaci, J. B. Haskins, and T. Çağln, *Characterization of Thermal Transport in Low-Dimensional Boron Nitride Nanostructures*, Phys. Rev. B - Condens. Matter Mater. Phys. **84**, (2011).

[179] F. Müller-Plathe, *A Simple Nonequilibrium Molecular Dynamics Method for Calculating the Thermal Conductivity*, J. Chem. Phys.

106, (1997).

[180] K. Termentzidis, P. Chantrenne, and P. Keblinski, *Nonequilibrium Molecular Dynamics Simulation of the In-Plane Thermal Conductivity of Superlattices with Rough Interfaces*, Phys. Rev. B - Condens. Matter Mater. Phys. **79**, (2009).

[181] Y. Hu, T. Feng, X. Gu, Z. Fan, X. Wang, M. Lundstrom, S. S. Shrestha, and H. Bao, *Unification of Nonequilibrium Molecular Dynamics and the Mode-Resolved Phonon Boltzmann Equation for Thermal Transport Simulations*, Phys. Rev. B **101**, (2020).

[182] T. Feng, W. Yao, Z. Wang, J. Shi, C. Li, B. Cao, and X. Ruan, *Spectral Analysis of Non-Equilibrium Molecular Dynamics: Spectral Phonon Temperature and Phonon Local Non-Equilibrium in Thin Films and across Interfaces*, Phys. Rev. B **95**, (2017).

[183] S. Merabia and K. Termentzidis, *Thermal Conductance at the Interface between Crystals Using Equilibrium and Nonequilibrium Molecular Dynamics*, Phys. Rev. B - Condens. Matter Mater. Phys. **86**, 094303 (2012).

[184] W. Bao, Z. Wang, and D. Tang, *Phonon Transport across GaN/AlN Interface: Interfacial Phonon Modes and Phonon Local Non-Equilibrium Analysis*, Int. J. Heat Mass Transf. **183**, (2022).

[185] P. Rowe, G. Csányi, D. Alfè, and A. Michaelides, *Development of a Machine Learning Potential for Graphene*, Phys. Rev. B **97**, (2018).

[186] J. I. Ramos, *The Boltzmann Equation and Its Applications*, Appl. Math. Model. **14**, (1990).

[187] R. Peierls, *Zur Kinetischen Theorie Der Wärmeleitung in Kristallen*, Ann. Phys. **395**, (1929).

[188] B. Davier, J. Larroque, P. Dollfus, L. Chaput, S. Volz, D. Lacroix, and J. Saint-Martin, *Heat Transfer in Rough Nanofilms and Nanowires Using Full Band Ab Initio Monte Carlo Simulation*, J.

Phys. Condens. Matter **30**, (2018).

[189] M. G. Holland, *Analysis of Lattice Thermal Conductivity*, Phys. Rev. **132**, (1963).

[190] J. Garg, N. Bonini, and N. Marzari, *High Thermal Conductivity in Short-Period Superlattices*, Nano Lett. **11**, (2011).

[191] T. Shiga, J. Shiomi, J. Ma, O. Delaire, T. Radzynski, A. Lusakowski, K. Esfarjani, and G. Chen, *Microscopic Mechanism of Low Thermal Conductivity in Lead Telluride*, Phys. Rev. B - Condens. Matter Mater. Phys. **85**, (2012).

[192] A. J. H. McGaughey and M. Kaviany, *Quantitative Validation of the Boltzmann Transport Equation Phonon Thermal Conductivity Model under the Single-Mode Relaxation Time Approximation*, Phys. Rev. B - Condens. Matter Mater. Phys. **69**, (2004).

[193] N. Mingo, L. Yang, D. Li, and A. Majumdar, *Predicting the Thermal Conductivity of Si and Ge Nanowires*, Nano Lett. **3**, (2003).

[194] A. Chernatynskiy and S. R. Phillpot, *Evaluation of Computational Techniques for Solving the Boltzmann Transport Equation for Lattice Thermal Conductivity Calculations*, Phys. Rev. B - Condens. Matter Mater. Phys. **82**, (2010).

[195] A. Rodin, M. Trushin, A. Carvalho, and A. H. Castro Neto, *Collective Excitations in 2D Materials*, Nat. Rev. Phys. **2**, 524 (2020).

[196] X. Gu, Y. Wei, X. Yin, B. Li, and R. Yang, *Colloquium: Phononic Thermal Properties of Two-Dimensional Materials*, Rev. Mod. Phys. **90**, 041002 (2018).

[197] J. Callaway, *Model for Lattice Thermal Conductivity at Low Temperatures*, Phys. Rev. **113**, (1959).

[198] Y. Guo and M. Wang, *Lattice Boltzmann Scheme for Hydrodynamic Equation of Phonon Transport*, Int. J. Therm. Sci. **171**, (2022).

[199] M. Kazan, G. Guisbiers, S. Pereira, M. R. Correia, P. Masri, A. Bruyant, S. Volz, and P. Royer, *Thermal Conductivity of Silicon Bulk and Nanowires: Effects of Isotopic Composition, Phonon Confinement, and Surface Roughness*, J. Appl. Phys. **107**, (2010).

[200] W. Li, J. Carrete, N. A. Katcho, and N. Mingo, *ShengBTE: A Solver of the Boltzmann Transport Equation for Phonons*, Comput. Phys. Commun. **185**, (2014).

[201] M. Omini and A. Sparavigna, *An Iterative Approach to the Phonon Boltzmann Equation in the Theory of Thermal Conductivity*, Phys. B Phys. Condens. Matter **212**, (1995).

[202] G. Fugallo, M. Lazzeri, L. Paulatto, and F. Mauri, *Ab Initio Variational Approach for Evaluating Lattice Thermal Conductivity*, Phys. Rev. B - Condens. Matter Mater. Phys. **88**, (2013).

[203] J. D. Chung, A. J. H. McGaughey, and M. Kaviany, *Role of Phonon Dispersion in Lattice Thermal Conductivity Modeling*, J. Heat Transfer **126**, (2004).

[204] G. H. Tang, C. Bi, and B. Fu, *Thermal Conduction in Nano-Porous Silicon Thin Film*, J. Appl. Phys. **114**, (2013).

[205] C. L. Chang and M. Chang, *Non-Iteration Estimation of Thermal Conductivity Using Finite Volume Method*, Int. Commun. Heat Mass Transf. **33**, (2006).

[206] D. Lacroix, K. Joulain, and D. Lemonnier, *Monte Carlo Transient Phonon Transport in Silicon and Germanium at Nanoscales*, Phys. Rev. B **72**, 064305 (2005).

[207] C. Jacoboni and L. Reggiani, *The Monte Carlo Method for the Solution of Charge Transport in Semiconductors with Applications to Covalent Materials*, Rev. Mod. Phys. **55**, (1983).

[208] R. B. Peterson, *Direct Simulation of Phonon-Mediated Heat Transfer in a Debye Crystal*, J. Heat Transfer **116**, (1994).

[209] S. Mazumder and A. Majumdar, *Monte Carlo Study of Phonon*

Transport in Solid Thin Films Including Dispersion and Polarization, J. Heat Transfer **123**, 749 (2001).

[210] K. Kukita, I. N. Adisusilo, and Y. Kamakura, *Monte Carlo Simulation of Diffusive-to-Ballistic Transition in Phonon Transport*, J. Comput. Electron. **13**, (2014).

[211] Z. Aksamija and I. Knezevic, *Anisotropy and Boundary Scattering in the Lattice Thermal Conductivity of Silicon Nanomembranes*, Phys. Rev. B - Condens. Matter Mater. Phys. **82**, (2010).

[212] Q. Hao, G. Chen, and M. S. Jeng, *Frequency-Dependent Monte Carlo Simulations of Phonon Transport in Two-Dimensional Porous Silicon with Aligned Pores*, J. Appl. Phys. **106**, (2009).

[213] J. P. M. Péraud and N. G. Hadjiconstantinou, *Efficient Simulation of Multidimensional Phonon Transport Using Energy-Based Variance-Reduced Monte Carlo Formulations*, Phys. Rev. B - Condens. Matter Mater. Phys. **84**, (2011).

[214] H. B. G. Casimir, *Note on the Conduction of Heat in Crystals*, Physica **5**, (1938).

[215] S. B. Soffer, *Statistical Model for the Size Effect in Electrical Conduction*, J. Appl. Phys. **38**, (1967).

[216] A. L. Moore, S. K. Saha, R. S. Prasher, and L. Shi, *Phonon Backscattering and Thermal Conductivity Suppression in Sawtooth Nanowires*, Appl. Phys. Lett. **93**, (2008).

[217] L. N. Maurer, Z. Aksamija, E. B. Ramayya, A. H. Davoody, and I. Knezevic, *Universal Features of Phonon Transport in Nanowires with Correlated Surface Roughness*, Appl. Phys. Lett. **106**, (2015).

[218] L. Chaput, J. Larroque, P. Dollfus, J. Saint-Martin, and D. Lacroix, *Ab Initio Based Calculations of the Thermal Conductivity at the Micron Scale*, Appl. Phys. Lett. **112**, (2018).

[219] L. Yang and A. J. Minnich, *Thermal Transport in Nanocrystalline Si and SiGe by Ab Initio Based Monte Carlo Simulation*, Sci. Rep. **7**, (2017).

[220] K. D. Parrish, J. R. Abel, A. Jain, J. A. Malen, and A. J. H. McGaughey, *Phonon-Boundary Scattering in Nanoporous Silicon Films: Comparison of Monte Carlo Techniques*, J. Appl. Phys. **122**, (2017).

[221] L. Zeng, V. Chiloyan, S. Huberman, A. A. Maznev, J. P. M. Peraud, N. G. Hadjiconstantinou, K. A. Nelson, and G. Chen, *Monte Carlo Study of Non-Diffusive Relaxation of a Transient Thermal Grating in Thin Membranes*, Appl. Phys. Lett. **108**, (2016).

[222] Y. Chen, D. Li, J. R. Lukes, and A. Majumdar, *Monte Carlo Simulation of Silicon Nanowire Thermal Conductivity*, J. Heat Transfer **127**, (2005).

[223] M. N. Z. Abidin and M. Y. Misro, *Numerical Simulation of Heat Transfer Using Finite Element Method*, J. Adv. Res. Fluid Mech. Therm. Sci. **92**, (2022).

[224] S. Hamian, T. Yamada, M. Faghri, and K. Park, *Finite Element Analysis of Transient Ballistic-Diffusive Phonon Heat Transport in Two-Dimensional Domains*, Biol. Control **80**, (2015).

[225] Y. Gu and J. Wang, *Green's Function Method Hybrid with the Finite Element Method for Ballistic Phonon Transport at Low Temperatures in Nanostructures of Arbitrary Shape*, Numer. Heat Transf. Part B Fundam. **72**, (2017).

[226] C. A. Gadre et al., *Nanoscale Imaging of Phonon Dynamics by Electron Microscopy*, Nature **606**, (2022).

[227] H. Zhou and G. Zhang, *General Theories and Features of Interfacial Thermal Transport*, Chinese Phys. B **27**, (2018).

[228] P. L. Kapitza, *Heat Transfer and Superfluidity of Helium II*, Phys. Rev. **60**, 354 (1941).

[229] M. Masuduzzaman and B. Kim, *Scale Effects in Nanoscale Heat Transfer for Fourier's Law in a Dissimilar Molecular Interface*, ACS Omega **5**, (2020).

[230] J. Zhang, Y. Hong, Z. Tong, Z. Xiao, H. Bao, and Y. Yue, *Molecular Dynamics Study of Interfacial Thermal Transport between Silicene and Substrates*, Phys. Chem. Chem. Phys. **17**, (2015).

[231] Y. Guo, Z. Zhang, M. Bescond, S. Xiong, M. Nomura, and S. Volz, *Anharmonic Phonon-Phonon Scattering at the Interface between Two Solids by Nonequilibrium Green's Function Formalism*, Phys. Rev. B **103**, (2021).

[232] J. Larroque, P. Dollfus, and J. Saint-Martin, *Phonon Transmission at Si/Ge and Polytypic Ge Interfaces Using Full-Band Mismatch Based Models*, J. Appl. Phys. **123**, (2018).

[233] R. S. Prasher and P. E. Phelan, *A Scattering-Mediated Acoustic Mismatch Model for the Prediction of Thermal Boundary Resistance*, J. Heat Transfer **123**, (2001).

[234] W. A. Little, *The Transport of Heat between Dissimilar Solids at Low Temperatures*, Can. J. Phys. **37**, 334 (1959).

[235] E. T. Swartz and R. O. Pohl, *Thermal Boundary Resistance*, Rev. Mod. Phys. **61**, 605 (1989).

[236] P. Reddy, K. Castelino, and A. Majumdar, *Diffuse Mismatch Model of Thermal Boundary Conductance Using Exact Phonon Dispersion*, Appl. Phys. Lett. **87**, 1 (2005).

[237] W. Zhang, T. S. Fisher, and N. Mingo, *Simulation of Interfacial Phonon Transport in Si-Ge Heterostructures Using an Atomistic Green's Function Method*, J. Heat Transfer **129**, (2007).

[238] J. Maassen and M. Lundstrom, *Modeling Ballistic Effects in Frequency-Dependent Transient Thermal Transport Using Diffusion Equations*, J. Appl. Phys. **119**, 95102 (2016).

[239] B. Davier, P. Dollfus, N. D. Le, S. Volz, J. Shiomi, and J. Saint-Martin, *Revisiting Thermal Conductivity and Interface Conductance at the Nanoscale*, Int. J. Heat Mass Transf. **183**, 122056 (2022).

[240] N. D. Le, B. Davier, N. Izitounene, P. Dollfus, and J. Saint-Martin, *Study of Phonon Transport across Si/Ge Interfaces Using Full-Band Phonon Monte Carlo Simulation*, J. Comput. Electron. **21**, 744 (2022).

[241] N. Izitounene, N. D. Le, B. Davier, P. Dollfus, L. Paulatto, and J. Saint-Martin, *Spectral Simulation of Heat Transfer Across Polytype Interfaces*, Cryst. Res. Technol. **57**, (2022).

[242] F. Giustino, *Materials Modelling Using Density Functional Theory: Properties and Predictions* (Oxford University Press, 2014).

[243] P. Hohenberg and W. Kohn, *Inhomogeneous Electron Gas*, Phys. Rev. **136**, (1964).

[244] W. Kohn and L. J. Sham, *Self-Consistent Equations Including Exchange and Correlation Effects*, Phys. Rev. **140**, (1965).

[245] J. Heyd, G. E. Scuseria, and M. Ernzerhof, *Hybrid Functionals Based on a Screened Coulomb Potential*, J. Chem. Phys. **118**, (2003).

[246] J. P. Perdew, M. Ernzerhof, and K. Burke, *Rationale for Mixing Exact Exchange with Density Functional Approximations*, J. Chem. Phys. **105**, (1996).

[247] A. D. Becke, *A New Mixing of Hartree-Fock and Local Density-Functional Theories*, J. Chem. Phys. **98**, (1993).

[248] A. Tkatchenko and M. Scheffler, *Accurate Molecular van Der Waals Interactions from Ground-State Electron Density and Free-Atom Reference Data*, Phys. Rev. Lett. **102**, (2009).

[249] U. Zimmerli, M. Parrinello, and P. Koumoutsakos, *Dispersion Corrections to Density Functionals for Water Aromatic Interactions*, J. Chem. Phys. **120**, (2004).

[250] N. E. Kirchner-Hall, W. Zhao, Y. Xiong, I. Timrov, and I. Dabo, *Extensive Benchmarking of DFT+U Calculations for Predicting Band Gaps*, Appl. Sci. **11**, (2021).

[251] S. Baroni, S. de Gironcoli, A. Dal Corso, and P. Giannozzi, *Phonons and Related Crystal Properties from Density-Functional Perturbation Theory*, Rev. Mod. Phys. **73**, 515 (2001).

[252] R. P. Feynman, *Forces in Molecules*, Phys. Rev. **56**, (1939).

[253] B. Wei, Q. Sun, C. Li, and J. Hong, *Phonon Anharmonicity: A Pertinent Review of Recent Progress and Perspective*, Sci. China Physics, Mech. Astron. **64**, 117001 (2021).

[254] X. Yan, B. Wang, Y. Hai, D. R. Kripalani, Q. Ke, and Y. Cai, *Phonon Anharmonicity and Thermal Conductivity of Two-Dimensional van Der Waals Materials: A Review*, Sci. China Physics, Mech. Astron. 2022 6511 **65**, 1 (2022).

[255] X. Yang, T. Feng, J. S. Kang, Y. Hu, J. Li, and X. Ruan, *Observation of Strong Higher-Order Lattice Anharmonicity in Raman and Infrared Spectra*, Phys. Rev. B **101**, (2020).

[256] X. Gonze and J. P. Vigneron, *Density-Functional Approach to Nonlinear-Response Coefficients of Solids*, Phys. Rev. B **39**, (1989).

[257] L. Paulatto, I. Errea, M. Calandra, and F. Mauri, *First-Principles Calculations of Phonon Frequencies, Lifetimes, and Spectral Functions from Weak to Strong Anharmonicity: The Example of Palladium Hydrides*, Phys. Rev. B - Condens. Matter Mater. Phys. **91**, (2015).

[258] I. Adamenko, *The Distribution Function for Phonons Emitted into He II by a Solid*, Phys. B Condens. Matter **284–288**, 33 (2000).

[259] B. Davier, Theoretical Study of Thermoelectric Properties in Nanostructures, Université Paris-Saclay, 2018.

[260] J. B. J. Fourier, *The Analytical Theory of Heat* (Cambridge University Press, 2009).

[261] J. Maassen and M. Lundstrom, *The Landauer Approach to Electron and Phonon Transport*, ECS Trans. **69**, 23 (2015).

[262] H. J. Monkhorst and J. D. Pack, *Special Points for Brillouin-Zone Integrations*, Phys. Rev. B **13**, 5188 (1976).

[263] M. E. Straumanis and C. D. Kim, *Phase Extent of Gallium Arsenide Determined by the Lattice Constant and Density Method*, Acta Crystallogr. **19**, 256 (1965).

[264] J. Meija et al., *Atomic Weights of the Elements 2013 (IUPAC Technical Report)*, Pure Appl. Chem. **88**, 265 (2016).

[265] A. A. Maznev, F. Hofmann, A. Jandl, K. Esfarjani, M. T. Bulsara, E. A. Fitzgerald, G. Chen, and K. A. Nelson, *Lifetime of Sub-THz Coherent Acoustic Phonons in a GaAs-AlAs Superlattice*, Appl. Phys. Lett. **102**, (2013).

[266] F. Hofmann, J. Garg, A. A. Maznev, A. Jandl, M. Bulsara, E. A. Fitzgerald, G. Chen, and K. A. Nelson, *Intrinsic to Extrinsic Phonon Lifetime Transition in a GaAs-AlAs Superlattice*, J. Phys. Condens. Matter **25**, (2013).

[267] A. Jain, Y. J. Yu, and A. J. H. McGaughey, *Phonon Transport in Periodic Silicon Nanoporous Films with Feature Sizes Greater than 100 Nm*, Phys. Rev. B - Condens. Matter Mater. Phys. **87**, (2013).

[268] D. P. Sellan, J. E. Turney, A. J. H. McGaughey, and C. H. Amon, *Cross-Plane Phonon Transport in Thin Films*, J. Appl. Phys. **108**, (2010).

[269] V. G. Dubrovskii and F. Glas, *Vapor–Liquid–Solid Growth of Semiconductor Nanowires*, in *Fundamental Properties of Semiconductor Nanowires* (Springer, 2021), pp. 3–107.

[270] H. Hijazi and V. G. Dubrovskii, *Dynamics of Monolayer Growth in Vapor–Liquid–Solid Gaas Nanowires Based on Surface Energy Minimization*, Nanomaterials **11**, (2021).

[271] R. Coehoorn, C. Haas, J. Dijkstra, C. J. F. Flipse, R. A. De Groot, and A. Wold, *Electronic Structure of MoSe2, MoS2, and WSe2. I. Band-Structure Calculations and Photoelectron Spectroscopy*,

Phys. Rev. B **35**, (1987).

[272] W. Paszkowicz, J. B. Pelka, M. Knapp, T. Szyszko, and S. Podsiadlo, *Lattice Parameters and Anisotropic Thermal Expansion of Hexagonal Boron Nitride in the 10-297.5 K Temperature Range*, Appl. Phys. A Mater. Sci. Process. **75**, 431 (2002).

[273] R. A. Gordon, D. Yang, E. D. Crozier, D. T. Jiang, and R. F. Frindt, *Structures of Exfoliated Single Layers of WS2, MoS2, and MoSe2 in Aqueous Suspension*, Phys. Rev. B - Condens. Matter Mater. Phys. **65**, 1254071 (2002).

[274] V. M. Karpan, G. Giovannetti, P. A. Khomyakov, M. Talanana, A. A. Starikov, M. Zwierzycki, J. Van Den Brink, G. Brocks, and P. J. Kelly, *Graphite and Graphene as Perfect Spin Filters*, Phys. Rev. Lett. **99**, (2007).

[275] J. Serrano, A. Bosak, R. Arenal, M. Krisch, K. Watanabe, T. Taniguchi, H. Kanda, A. Rubio, and L. Wirtz, *Vibrational Properties of Hexagonal Boron Nitride: Inelastic X-Ray Scattering and Ab Initio Calculations*, Phys. Rev. Lett. **98**, (2007).

[276] M. Mohr, J. Maultzsch, E. Dobardžić, S. Reich, I. Milošević, M. Damnjanović, A. Bosak, M. Krisch, and C. Thomsen, *Phonon Dispersion of Graphite by Inelastic X-Ray Scattering*, Phys. Rev. B - Condens. Matter Mater. Phys. **76**, (2007).

[277] N. Wakabayashi, H. G. Smith, and R. M. Nicklow, *Lattice Dynamics of Hexagonal MoS2 Studied by Neutron Scattering*, Phys. Rev. B **12**, 659 (1975).

[278] Q. Cai, B. Wei, Q. Sun, A. H. Said, and C. Li, *Monolayer-like Lattice Dynamics in Bulk WSe2*, Mater. Today Phys. **28**, (2022).

[279] T. Sohier, M. Gibertini, M. Calandra, F. Mauri, and N. Marzari, *Breakdown of Optical Phonons' Splitting in Two-Dimensional Materials*, Nano Lett. **17**, 3758 (2017).

[280] H. Terrones, F. López-Urías, and M. Terrones, *Novel Hetero-*

Layered Materials with Tunable Direct Band Gaps by Sandwiching Different Metal Disulfides and Diselenides, Sci. Rep. **3**, 1549 (2013).

[281] M. E. Wieser et al., *Atomic Weights of the Elements 2011 (IUPAC Technical Report)*, Pure Appl. Chem. **85**, (2013).

[282] P. Scuracchio, K. H. Michel, and F. M. Peeters, *Phonon Hydrodynamics, Thermal Conductivity, and Second Sound in Two-Dimensional Crystals*, Phys. Rev. B **99**, (2019).

[283] H. E. Jackson, C. T. Walker, and T. F. McNelly, *Second Sound in NaF*, Phys. Rev. Lett. **25**, (1970).

[284] S. Chen, Q. Wu, C. Mishra, J. Kang, H. Zhang, K. Cho, W. Cai, A. A. Balandin, and R. S. Ruoff, *Thermal Conductivity of Isotopically Modified Graphene*, Nat. Mater. **11**, 203 (2012).

[285] Y. Wang, Y. Gao, E. Easy, E.-H. Yang, B. Xu, and X. Zhang, *Thermal Conductivities and Interfacial Thermal Conductance of 2D WSe2*, in *2020 IEEE 15th International Conference on Nano/Micro Engineered and Molecular System (NEMS)* (IEEE, 2020), pp. 575–579.

[286] Z. Y. Ong and G. Zhang, *Efficient Approach for Modeling Phonon Transmission Probability in Nanoscale Interfacial Thermal Transport*, Phys. Rev. B - Condens. Matter Mater. Phys. **91**, (2015).

[287] Y. Zhang, Q. X. Pei, C. M. Wang, C. Yang, and Y. W. Zhang, *Interfacial Thermal Conductance and Thermal Rectification of Hexagonal BCnN/Graphene In-Plane Heterojunctions*, J. Phys. Chem. C **122**, 22783 (2018).

[288] Z. Liang, K. Sasikumar, and P. Keblinski, *Thermal Transport across a Substrate-Thin-Film Interface: Effects of Film Thickness and Surface Roughness*, Phys. Rev. Lett. **113**, 065901 (2014).

[289] E. Pop, *Energy Dissipation and Transport in Nanoscale Devices*, Nano Res. **3**, 147 (2010).

[290] L. J. Zhou, G. N. Wu, J. F. Yu, and X. H. Zhang, *Thermal Overshoot Analysis for Hot-Spot Temperature Rise of Transformer*, IEEE Trans. Dielectr. Electr. Insul. **14**, 1316 (2007).

[291] K. Yazawa, D. Kendig, J. Reiter, and A. Shakouri, *Intrinsic Transient Thermal Response of GaN HEMT*, in *2016 IEEE MTT-S International Microwave Symposium (IMS)*, Vols. 2016-August (IEEE, 2016), pp. 1–3.

[292] G. Mandrusiak, X. She, A. M. Waddell, and S. Acharya, *On the Transient Thermal Characteristics of Silicon Carbide Power Electronics Modules*, IEEE Trans. Power Electron. **33**, 9783 (2018).

[293] J. Zhang, T. Zhang, S. Prakash, and Y. Jaluria, *Experimental and Numerical Study of Transient Electronic Chip Cooling by Liquid Flow in Microchannel Heat Sinks*, Numer. Heat Transf. Part A Appl. **65**, 627 (2014).

[294] G. Chen, *Ballistic-Diffusive Equations for Transient Heat Conduction from Nano to Macroscales*, J. Heat Transfer **124**, 320 (2002).

[295] H. Fei, *The Importance and Applications of Heat Capacity: Investigating a Fundamental Property of Matter*, J. Thermodyn. Catal. **14**, 1 (2023).

[296] V. L. Solozhenko, *Thermodynamics of Dense Boron Nitride Modifications and a New Phase P,T Diagram for BN*, Thermochim. Acta **218**, 221 (1993).

[297] K. S. Gavrichev, V. L. Solozhenko, V. E. Gorbunov, L. N. Golushina, G. A. Totrova, and V. B. Lazarev, *Low-Temperature Heat Capacity and Thermodynamic Properties of Four Boron Nitride Modifications*, Thermochim. Acta **217**, 77 (1993).

[298] S. Mann, P. Rani, R. Kumar, G. S. Dubey, and V. K. Jindal, *Thermodynamic Properties of Pure and Doped (B, N) Graphene*, RSC Adv. **6**, 12158 (2016).

[299] E. Muñoz, J. Lu, and B. I. Yakobson, *Ballistic Thermal*

Conductance of Graphene Ribbons, Nano Lett. **10**, 1652 (2010).

[300] A. Arriagada, E. T. Yu, and P. R. Bandaru, *Determination of Thermal Parameters of One-Dimensional Nanostructures through a Thermal Transient Method*, J. Therm. Anal. Calorim. **97**, 1023 (2009).

[301] D. Abarbanel and J. Maassen, *Modeling Quasi-Ballistic Transient Thermal Transport with Spatially Sinusoidal Heating: A McKelvey-Shockley Flux Approach*, J. Appl. Phys. **121**, (2017).

[302] Z. M. Tan and W. J. Yang, *Propagation of Thermal Waves in Transient Heat Conduction in a Thin Film*, J. Franklin Inst. **336**, 185 (1999).